MONASH University

Liquid marbles: Study of their mechanics and applications

Eric Shen Lin
(Bachelor of Mechanical Engineering (Honours))

A thesis submitted for the degree of *Doctor of Philosophy* at
Monash University in *2023*
Department of Mechanical and Aerospace Engineering

Copyright notice

Abstract

Liquid marbles (LMs) have continued to be actively investigated despite being first reported way back in 2001. They are unique in that the encapsulating shell isolates the liquid core by preventing contact with the air around it. LMs were initially studied for their unusual physical characteristics but are now increasing being explored for applications.

The research efforts conducted in this project can be classified into 3 main areas. In terms of the creation, content removal, and applications aspect, a new method of using brushes to create LMs in a more controlled manner was reported. An adaptation of this method allowed Janus liquid marbles (JLMs) to be created more controllably. Due to an access feature inherent with the method, capillary tubes could be used to extract the liquid contents of the LMs. Finally, a new method to separate particles according to their wetting characteristics was demonstrated.

In terms of investigating gas bubbles in LMs, a syringe-based fluid dispensation system developed was found to deliver gas bubbles precisely as well. A new technique for measuring gas bubble flowrates using an inverted burette technique was also developed. The delivery of singular gas bubbles into the LM was found to clear the shell at the apex but reformed when the bubble ruptured. Finally, a method of LM aeration via the generation of oxygen or hydrogen gases using electrolysis was demonstrated.

In terms of investigating the freezing of LMs, it was found that bacteria could be cryopreserved using frozen sessile drops with higher viability than using standard liquid vials. An application in additive manufacturing involving monitoring the conical shapes with tip points at the apexes of frozen drops was developed. It was found that frozen LMs made with copper powder mixed in with contaminants, which may result in poor quality engineering components being produced, could be detected by measuring the angles of the tips.

In future, the brush-on technique could to be developed further via automation processes such that arrays of LMs can be rapidly produced. By introducing better gaseous control techniques, the bubble may remain inside the LM for a longer period of time so that more elaborate processes could be incorporated. Further work could be conducted to determine if frozen LMs would have the same benefits as frozen sessile drops in improving the cryopreservation of bacteria over standard vials. Overall, this project has been successful in advancing knowledge and applications using LMs.

Declaration

This thesis is an original work of my research and contains no material which has been accepted for the award of any other degree or diploma at any university or equivalent institution and that, to the best of my knowledge and belief, this thesis contains no material previously published or written by another person, except where due reference is made in the text of the thesis.

Signature: ……

Print Name: …ERIC SHEN LIN…….

Date: ……06/02/2023……

Publications during enrolment

1. **E Lin**, Z. Song, J.W. Ong, H.A. Abid, O.W. Liew, T.W. Ng, Brushed creation of liquid marbles. PeerJ Materials Science 4 (2022) e24.

2. J.W. Ong, H.A. Abid, T. Minifie, **E.S. Lin**, Z. Song, M. Katariya, O.W. Liew, T.W. Ng, Unmanned aerial vehicle transport of frozen blood samples using phase change materials. Biosystems Engineering. 221 (2022) 30-42.

3. **E.S. Lin**, Z. Song, J.W. Ong, H.A. Abid, O.W. Liew, T.W. Ng, Liquid marble microbioreactor aeration facilitated by on-demand electrolysis. Results in Chemistry. 4 (2022) 100334.

4. J.W. Ong, Z. Song, H.A. Abid, **E.S. Lin**, O.W. Liew, T.W. Ng, Cryoprotectant-free preservation of bacteria using semi-spherical drops. Cryobiology. 104 (2022) 98-101.

5. Z. Song, **E.S. Lin**, M.H. Uddin, H.A. Abid, J.W. Ong, O.W. Liew, T.W. Ng, Fog harvesting with highly wetting and non-wetting vertical strips. Langmuir. 38 (2022) 1845–1852.

6. H.A. Abid, J.W. Ong, **E.S. Lin**, Z. Song, O.W. Liew, T.W. Ng, Low-cost imaging of fluorescent DNA in agarose gel electrophoresis using Raspberry Pi cameras. Journal of Fluorescence. 32 (2022) 443–448.

7. Z. Song, J.W. Ong, **E.S. Lin**, H.A. Abid, O.W. Liew, T.W. Ng, Superwetting antibacterial copper oxide nanoflake foil substrates generated by thermal oxidation. JCIS Open. 5 (2022) 100042.

8. H.A. Abid, J.W. Ong, Z. Song, **E.S. Lin**, O.W. Liew, T.W. Ng, Thermal study of Polymerase Chain Reaction with capillary tubes. International Journal of Heat and Mass Transfer. 176 (2021) 121508.

9. **E.S. Lin**, Z. Song, J.W. Ong, H.A. Abid, D.C.K. Chung, S.H. Huynh, O.W. Liew, T.W. Ng, Liquid marble clearance and restoration using gas bubble insertion and bursting. Soft Matter. 17 (2021) 2512-2517.

10. H.A. Abid, T. Minifie, J.W. Ong, **E.S. Lin**, Z. Song, O.W. Liew, T.W. Ng, Inflight Polymerase Chain Reaction of samples with drones. Analytical Biochemistry. 616 (2021) 114098.

11. Z. Song, **E.S. Lin**, J. Zhu, J.W. Ong, H.A. Abid, M.H. Uddin, O.W. Liew, T.W. Ng, Sustained graphene oxide coated superhydrophilicity and superwetting using humidity control. Colloids and Surfaces A: Physicochemical and Engineering Aspects. 613 (2021) 126097.

12. H.A. Abid, **E.S. Lin**, J.W. Ong, T. Minifie, Z. Song, O.W. Liew, T.W. Ng, Polymerase chain reaction thermal cycling using the programmed tilt displacements of capillary tubes. Review of Scientific Instruments. 91 (2020) 104105.

13. Z. Song, **E.S. Lin**, Md.H. Uddin, J.W. Ong, H.A. Abid, Z. Xiong, D. Li, O.W. Liew, T.W. Ng, Temporal evolution of wetting transitions of graphene oxide coated on

roughened polyvinyl chloride surfaces. Materials Today Communications. 25 (2020) 101650.

14. J.W. Ong, T. Minifie, **E.S. Lin**, H.A. Abid, O.W. Liew, T.W. Ng, Cryopreservation without dry ice-induced acidification during sample transport. Analytical Biochemistry. 608 (2020) 113906.

15. **E.S. Lin**, D.C.K. Chung, J.W. Ong, H.A. Abid, L. Peng, X. Jiang, O.W. Liew, T.W. Ng, Liquid marble particle wetting separation. Colloids and Interface Science Communications. 35 (2020) 100237.

16. H.A. Abid, J.W. Ong, **E.S. Lin**, O.W. Liew, T.W. Ng, Volume and rate measurement of slowly generated gas bubbles. Flow Measurement and Instrumentation. 72 (2020) 101694.

17. J.W. Ong, D.C.K. Chung, **E.S. Lin**, H.A. Abid, O.W. Liew, T.W. Ng, Syringe infusion pump with absolute piston displacement control. Review of Scientific Instruments 90 (2019) 076108.

18. **E.S. Lin**, Z. Song, H.A. Abid, J.W. Ong, O.W. Liew, T.W. Ng, Stable creation of Janus liquid marbles, Submitted.

19. **E.S. Lin**, Z. Song, H.A. Abid, J.W. Ong, T.W. Ng, Drop freezing detection of feedstock contaminants in copper powder bed fusion additive manufacturing, Submitted.

Acknowledgements

I would like to express my deepest gratitude to my supervisor Associate Professor Tuck Wah Ng who generously provided knowledge and expertise. This endeavour would not have been possible without his invaluable patience and feedback throughout. Special thanks to Monash University who provided facilities and equipment for this endeavour.

I am also grateful to my friends who shared the laboratory space, Jian Ong, Hassan Abid and Zhixiong Song for their experimental help and moral support.

Lastly, I'd like to mention my family who have provided support that has kept my motivation high during this process.

Table of Contents

1. Introduction

1.1 Background

Particles can interact with the droplet in 4 different locations (see Figure 1): At the contact line, liquid-gas interface, inside the liquid or at the liquid-solid interface. The field of research differs depending on the location of interaction.

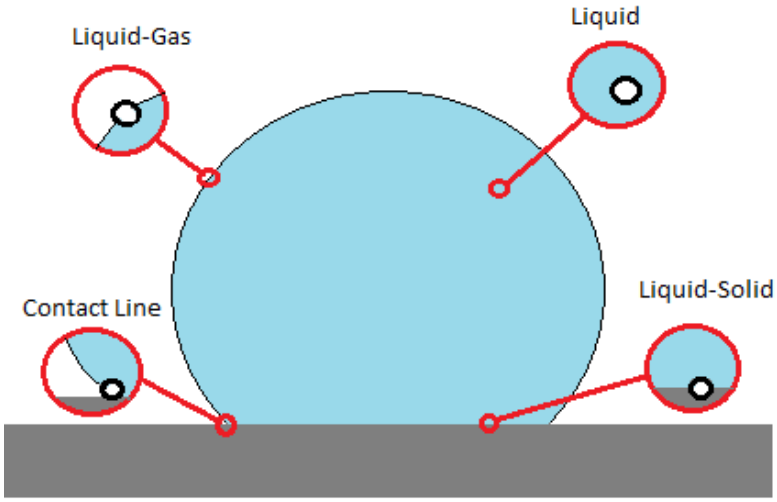

Figure 1 Depiction of the 4 different locations of particle interation; at the contact line, liquid-gas interface, inside the liquid or at the liquid-solid interface

Particle laden drops occur when the particle interaction locations are either within the liquid or at the liquid-solid interface. This can be classified as colloids, a mixture in which solid particles are suspended throughout the liquid. Colloids are important in fields ranging from manufacturing to biology [1]. Particles are added to the fluid to improve the intrinsic fluid properties or improve processes.

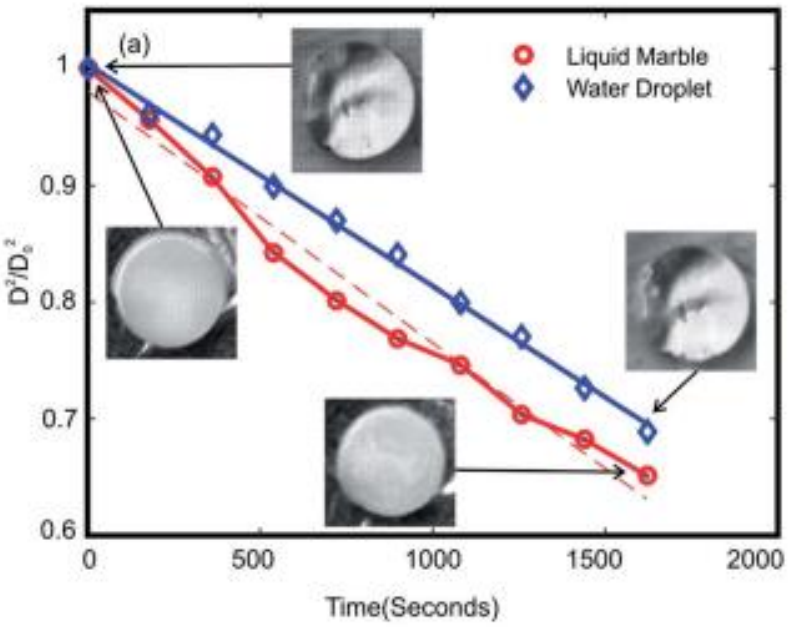

Figure 2 Surface regression of a single 10 µL liquid marble and water droplet at room temperature [2]. It is clear that liquid marbles have advantages in reducing the evaporation rate.

A liquid marble (LM) is formed when the particle interaction locations are either at the liquid-gas interface or at the contact line. LMs are freestanding droplets covered by nano or micro-sized particles. The simplest way to create a LM is to roll a liquid droplet onto a bed of hydrophobic microparticles. The particles form a protective shell on the droplet, which acts as a barrier at the liquid-gas interface. It can be manipulated as a soft solid, causing a non-stick situation for a liquid-solid pair. As such, LMs have attracted considerable attention for applications such as gas sensing [3], water pollution [4], microfluidics [5] and more. While liquid marbles and liquid drops (even with particles in them) can assume the same shape, there are clear differences in their behaviour. This is illustrated by their varied surface regression responses due to evaporation, for example, as shown in Figure 2. These differences hence warrant the need to understand liquid marbles better.

1.2 Objectives and Approach

The overall objectives of this candidature are three-fold. They include:
- Conduct investigations to better understand the mechanics of liquid marbles
- Devise new methods and equipment to facilitate these investigations
- Develop new applications using liquid marbles based on the investigations conducted

In order to obtain the necessary background information prior to undertaking the objectives of the project, it was necessary to conduct a reasonably exhaustive literature review on the fundamental basis of liquid marbles and the salient developments to date using liquid marble technology. The outcomes of this review are presented in Chapter 2.

Following the efforts of the literature review, a series of investigations were conducted with the intention to compose the main body of this thesis. To provide a more coherent organization, these efforts have been classified into 3 main categories:
- The creation, content removal, and applications of liquid marbles
- Gas bubbles in liquid marbles, and
- Liquid marble freezing

The body of work conducted under these three categories are presented in Chapters 3, 4, and 5 respectively.

1.3 Scope

The original method of LM creation involves dispensing a liquid droplet on a bed of hydrophobic powder and rolling it about [6]. This has remained the conventional method for creating LMs since it can be done with minimal instrumentation, however generation of large amounts of LMs in quick succession can be difficult to achieve. Discharging multiple liquid drops onto a single particulate bed followed by agitation to form the outer shell can result in contamination through material transference from one liquid body to another. This can be undesirable especially when the LMs are used in applications of microbioreactors for the cell culture, viruses or bacteria.

Janus liquid marbles (JLMs) have been created by coalescing two individual liquid marbles [7-9], however a method of dropping liquids onto separate powder beds sequentially has also been attempted [10]. These approaches have drawbacks in that they cannot create JLMs in a controlled and uniform manner.

This thesis addresses these issues arising from LM creation by brushing particles onto a liquid drop that was located stably on a strongly hydrophobic substrate with a hole. It is proven to create LMs in a controlled fashion [11]. The underlying mechanics needed to develop JLMs in a controlled manner are outlined and a new approach to do so is described and demonstrated.

There are limitations in removing the covering particles from the LM in order to reach the liquid core and determine its biological and chemical state. The utilisation of optical radiation [12], ultrasonic fields [13], and timed disintegration with wettability change [14] are some of the methods that have been tried to accomplish this. However, the characteristics of the liquid, the wetting properties of the liquids and particles, the delivery of motive forces through actuators, and the design of the equipment required to provide the non-contacting fields are just a few physical factors that can affect the effectiveness of these approaches.

In this thesis, a method of draining the liquid contents without any particle carryover was investigated. A capillary tube is inserted into the overhanging component of the drop and a method to coat just the sessile component of the drop is established. This is advantageous as no external energy source is required, enabling the development of scientific applications based on this idea [15].

Gas bubbles has been shown to play an important role in liquid marbles. Two parameters that are essential for gas sample analysis are their average production rates and total production volumes throughout specified time periods. Flowrate sensors measure the former parameter in order to derive the latter. The devices and structures needed to accomplish this can be expensive and complicated [16-18].

This thesis explores a more direct way of measurement involves sending the gas to an airtight syringe, where the extent of plunger movement over time enables the determination of both parameters.

It has been proven difficult to add additional reagents into the LM without contamination or deformation. This thesis provides a solution to this via the generation of a singular air bubble within an LM that is deposited on a superhydrophobic substrate with a hole [19-21]. The suspended air bubble causes localised displacements of the outer shell particles, forming open regions at the apex of the LM. Clearly, this allows additional reagents to be added to the LM prior to bubble rupture and shell reformation.

Electrolysis of water has been used to generate gas bubble streams however, it currently cannot be used to improve the aeration of the internal contents of a LM without disrupting the chemistry in the medium.

This thesis proposes a method of overhead aeration through the generation of gas by electrolysis, ensuring that the composition in the overhead component is minimally affected in the process. Apart from this, investigations were also conducted to establish the interaction of the bubbles with the encapsulating particles as well as the stability of the bubbles needed for aeration.

Cryopreservation is a regularly used technology for long-term preservation that ensures the quality and viability of microorganisms in laboratories and biological resource institutions. However, microbial viability is negatively impacted by freeze-thaw damage and variations in osmotic pressure throughout the cryopreservation procedure [22]. Utilizing the unique thermal properties of semi-spherical drops, a novel cryopreservation technique is developed in this research that eliminates the requirement for cryoprotectants.

A limitation in laser powder bed fusion (LPBF) additive manufacturing lies in the potential presence of contaminants in the feedstock which could affect the quality of the fabricated parts [23]. In-process monitoring methods can be used to detect the contaminants [24], however an assessment prior to use would clearly be more effective.

This thesis utilises frozen LMs created from copper powder, as well as varying levels of copper/hydrated magnesium silicate (Talc) and copper/graphite compositions to address the issue. The frozen drops were analysed for their tip and contact angles. Consequently, an assessment was made to determine if this approach could be developed into a method to monitor feedstock contamination of copper powder in LPBF.

2. Literature Review

This literature review sought to provide the basis behind how liquid marbles are created and to uncover the applications that are possible with it. As this field is very extensive, it was not possible to cover all the aspects. However, the major issues in this topic have been studied and presented in this chapter, with the intention of guiding the investigative efforts involved in this dissertation.

In section 2.1, the history behind the creation of liquid marbles and the various ways in which they have been developed into applications was examined. As this work sought to find ways to extend the manner in which liquid marbles can be created as well as utilized, the review was naturally broadened to cover some important aspects associated with liquid drops, since liquid drops and liquid marbles can be presented as discrete entities on surfaces. In section 2.2, the important relationships concerning liquid drops and surface wetting were outlined. In section 2.3, colloidal drops were reviewed since particles play a key role in their formation as in the case of liquid marbles. In section 2.4 key aspects of liquid drop freezing were reviewed due to their ability to assume solid forms, similar to the case when liquid marbles were frozen. Finally, the characteristics of gas bubbles were considered due to their being able to exist as a separate phase in liquid drops as well as in liquid marbles.

2.1 Liquid Marbles

Liquid marbles (LMs) have captivated the attention of researchers over many years. These soft particles can be hydrophobic or hydrophilic in nature and can be controlled. Aussillous and Quere [6] first developed a simple method for manufacturing LMs by rolling a liquid droplet over a bed of hydrophobic microparticles. The hydrophobic encapsulating shell safeguards the liquid core by preventing its contact with the surrounding air. LMs provide a non-adhesive alternative to super-hydrophobicity as a liquid-solid pair. LMs are intriguing due to their unusual physical characteristics and potential applications.

Superhydrophobicity is often achieved by changing the surface of a solid substrate [25]. In the case of LMs, the opposite method is employed: superhydrophobic or nonwetting particles are deposited to the surface of the liquid. It should be emphasised that LMs maintain their non-adhesive properties on a vast array of solid and liquid supports. Similar to how air cushions remove Leidenfrost drops from their support, air cushions separate LMs from their support [26]. Aberle et al. [27] have recently investigated the Leidenfrost effect on the behaviour of LMs placed on hot surfaces.

Since LMs comprise of a solid-solid interface on contact instead of the usual liquid-solid interface, they become non-stick droplets with very low friction at the surface. As a result, minimal forces are required to manipulate the LM's shape or movement. There have been several different strategies reported to manipulate the LM, with magnetic and electrostatic forces being the main ones [28].

2.1.1 Electrostatics

It has been shown that LMs can be controlled by electric and magnetic fields [28]. Due to the fact that an electric field distorts the geometry of dielectric droplets, droplets deposited on superhydrophobic surfaces and LMs are expected to behave similarly when subjected to an electric field. However, this is not the case.

Understanding of the concept is enhanced by considering the contact of the droplet with the solid substrate and the formation of a second electrical layer inside the contact area. Even without an external field, the droplet possesses a non-zero dipole moment due to its double electrical layer. Changing the direction of the external field alters both the polarity of the substrate and the droplet, thus the droplet can only be stretched by the external field. This impact can be overlooked, at least for spherical marbles, due to the random position of the solid particles on the surface of the LM.

Liyanaarachchi [28] has reported the unexpected release of electrostatically charged glass beads from a particle bed, traversing the air gap and covering a suspended water droplet to create a metastable spherical aggregate on the bed surface. A bed of micron-sized ballotini particles was contained by a charged substrate wrapped with PTFE tape. The PTFE tape was utilised to facilitate frictional charging [29]. Particles were observed crossing the millimetre gap and penetrating the droplet's surface as it approached from above. The authors observed that the particles filled the droplet within 300 ms before detaching and resting in a metastable state on the powder bed. This discovered phenomenon may represent an alternate way for producing LMs, with the advantage of using hydrophilic particles. The conventional method of dropping a droplet over a bed of hydrophilic particles would result in liquid absorption.

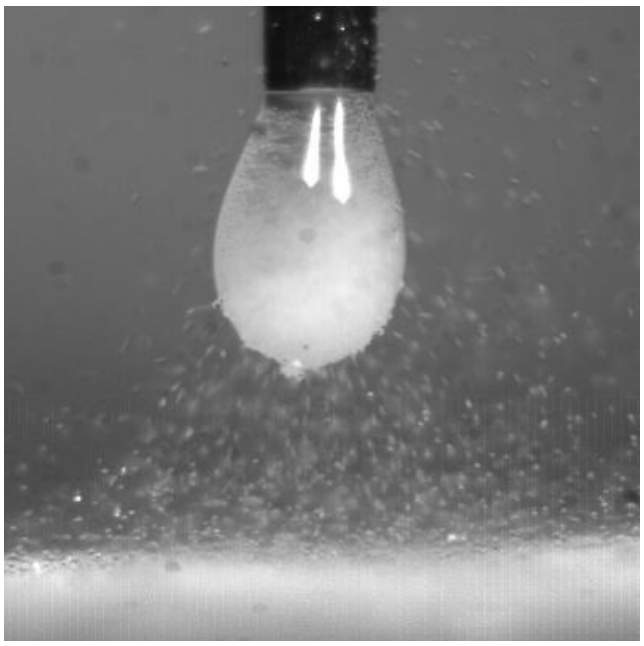

Figure 3 Particles of spherical ballotini being transferred to a pendant drop of water across an air gap over 300ms [28]

Aussillous and Quere [30] pioneered the research by showing a LM could be moved under the effect of an electrostatic field, created by simply rubbing a Teflon on fabric. It was also found that liquid droplets can be spontaneously coated with hydrophobic particles, which results in a multi-layer LM. The LM's movements can be controlled, and its shape deformed under the influence of an electric field provided by a capacitor.

Bormashenko [31] reported similar findings for Janus liquid marbles (JLMs), droplets formed of two hemispheres with differing physical or chemical properties. Due to the difference in electric characteristics of particles in the shell coating, a JLM composed of carbon black and Teflon was able to be rotated using an electric field [31]. Under the influence of an external electric field, the researchers were able to control composite non-stick droplets composed of di-iodomethane and water in a subsequent paper [7]. The composite marbles were placed on a superhydrophobic surface between two electrodes, and the electric field was increased to 106 V/m gradually. Once the electric field reached E = 7.105 V/m, they observed that the water drop began to 'climb' the di-iodomethane drop within the marble. At the upper limit of E = 106 V/m, it was discovered that the water droplet resides on the surface of the composite marble.

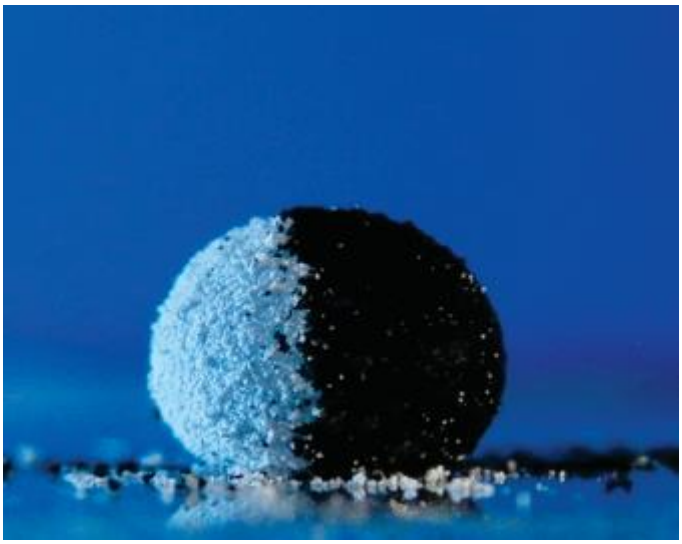

Figure 4 Janus liquid marble comprising of two different powder coatings [31]

2.1.2 Magnetism

Utilizing magnetic forces for LM manipulation has gained popularity as a result of its ease of use. As no physical touch is necessary, this enables remote manipulation of the LM. The two primary techniques for utilising the responses include magnetising the particle shell or the liquid core [32].

In the case of the magnetic particle shell, the outer layer of the LM consists of hydrophobic magnetic particles, such as nanoparticles of iron (Fe_3O_4) or nanoparticles created by combining iron with other materials [32]. The iron particles endow the outer shell with superparamagnetic characteristics, enabling manipulation of the LM with an external magnetic field. As a result, the hydrophobic coating on these magnetic marbles could be opened and closed reversibly and be utilised to join two marbles. Curiously, magnetic LMs roll towards a permanent magnet rather than sliding on a solid surface.

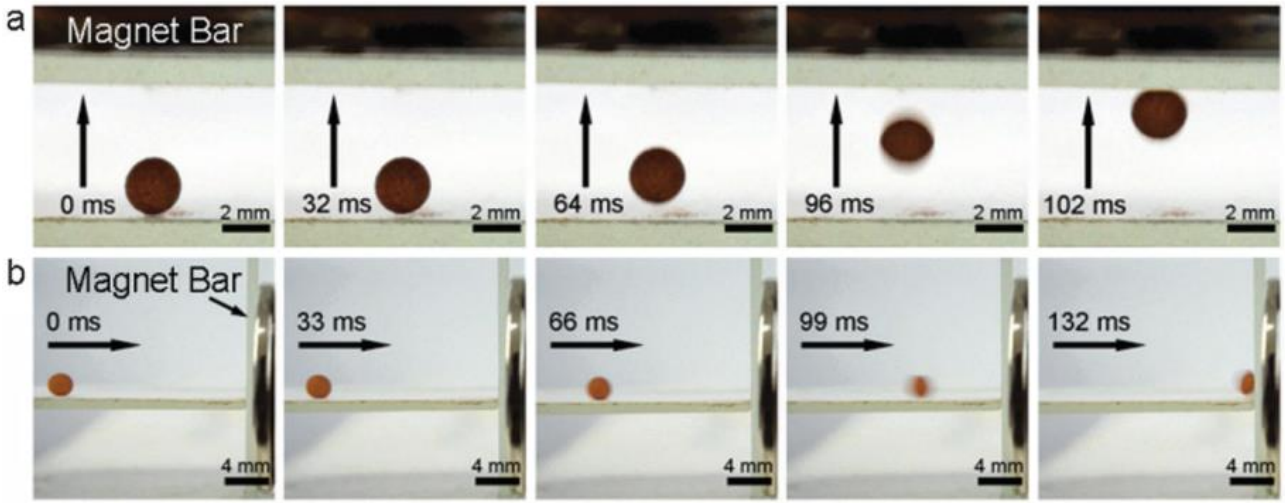

Figure 5 a) Digital camera images of a liquid marble moving vertically (a) and horizontally (b), driven by a magnet bar [14]

Lin et al. [33] created biocompatible magnetic superhydrophobic cellulose-based LMs, enabling their usage in biomedical applications. Similar to superparamagnetic behaviour, the produced composite microspheres exhibited a tiny hysteresis loop and low coercivity. They demonstrated that an LM may be managed in a directed manner using a magnetic bar, which has applications in the controlled movement of liquids.

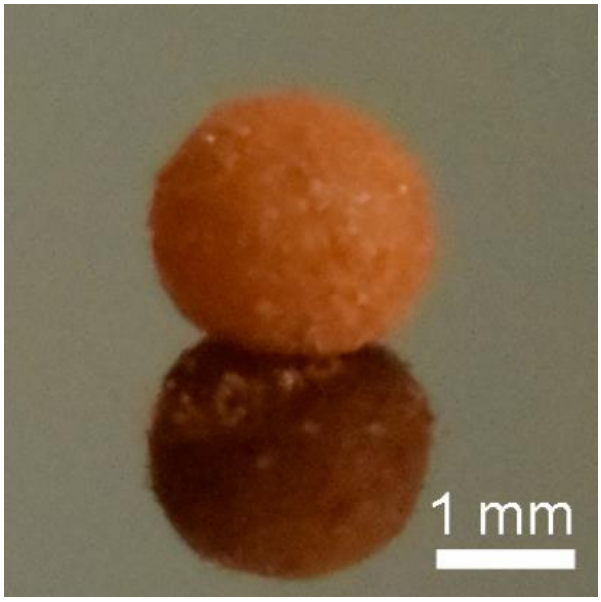

Figure 6 Liquid marble generated from poly(DOPAm-ci-PFOEA)/Fe3O4/cellulose microspheres [34]

Since LMs may be opened and closed reversibly, it is possible to examine the marble's liquid core. It is feasible to gain direct access to the core and add a second liquid, allowing it to be utilised as a microreactor suited for chemical reactions [35]. This characteristic permits optical detection, which makes it possible to examine the chemical composition and reactions within the LM without disrupting its shell. Zhao et al. [36] successfully transported LMs around a proposed device and measured the electrochemical characteristics of the LM's contents. Superhydrophobic magnetic LMs were produced by rolling a water droplet on a bed of Fe_3O_4 nanoparticles. As an external inhomogeneous magnetic field, neodymium cylinder magnets were employed. As each magnetic moment of a magnetic domain has different orientations, the magnetic LM lacks magnetic properties. However, when an external magnetic field is introduced, the magnetic domains align in the same direction, leading the LM to become active.

A magnetic device can be added to the liquid core in order to manipulate the LM's contents. Using a digital microfluidics platform, the authors [37] intended to use the apparatus to magnetically control the transport of aqueous solution. Using voltammetry with a miniaturised three-electrode probe to detect dopamine in the core of an LM, they demonstrated the detection of liquid components in magnetic LMs. This measurement result is essential for detecting brain function abnormalities. In addition, they demonstrated work on optical absorbance detection on an opened LM, which enabled the applications of glucose assays. Subsequently, shell hardening to protect reagents using hydrophobic particles with a low melting point was demonstrated [38]. These new qualities of magnetic LMs, sample detection, storage, actuation, and microreactors enable the construction of "lab-on-a-drop" devices, hence enabling novel applications in biotechnology [39], chemical synthesis [40], and analytical chemistry [41].

2.1.3 Cell Culture

The shell of the LM is known to be gas permeable, as indicated by numerous papers pertaining to gas sensing [42]. Gas permeability is essential for cell culture applications since it permits oxygen and carbon dioxide gas exchange between the environment and the cell culture medium. This technique has been utilised for the creation of cancer cell spheroids [43], embryoid bodies [44], olfactory ensheathing cell spheroids [45], and the in-vitro maturation of sheep oocytes [46]. Tian et al. [47] revealed that LMs might be utilised for the cultivation of aerobic bacteria.

Cancer cell spheroids were produced by inoculating hepatocellular carcinoma cells in an LM [43]. The essential cell aggregation for CCS formation was facilitated by the inherent properties of LM: their limited volume, which promoted a greater intercellular contact, and their non-adhesive shell, which prevented cell attachment.

The use of these 3D bioreactors for embryoid body development has also been documented; since pluripotent embryonic stem cells tend to congregate [48], LMs represent a low-effort and highly efficient in vitro manufacturing strategy. It was also observed that the LM provided a favourable microenvironment for spontaneously inducing the differentiation of embryoid bodies into functional cardiomyocytes [49]. It was emphasized that this technology would be highly beneficial to provide a continuous source of cardiomyocytes for regenerative medicine applications [50], drug discovery [51] and safety testing [52].

In related research, it was demonstrated that LM can also be employed for co-culture trials [45]. Schwann cells or astrocytes were co-cultured with olfactory ensheathing cells. On the liquid environment given by LMs, the olfactory ensheathing cells were able to duplicate their typical behaviour of surrounding other cell types, as the cells were able to freely associate with the other cell types [45].

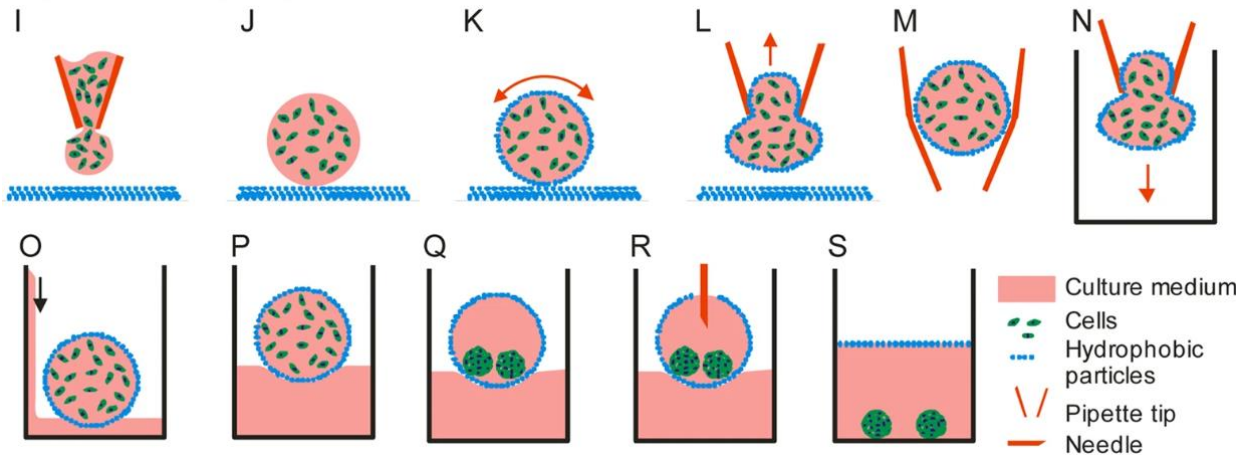

Figure 7 (I,J) A droplet of cells is deposited on the PTFE powder bed and (K) then coated with PTFE by rotating the marble in circular movements. (L–N) A pipette tip is used to pick up, transfer and (O,P) is then floated by dispensing media against the wall of the well. (Q) After incubation, the cells form spheroids inside the marbles. (R,S) Marbles can be broken with needles to release the spheroids which then sink to the bottom of the well. [53]

Floating LMs can be used to construct olfactory ensheathing cell spheroids [45]. The selection of these LMs was justified by the fact that floating LMs were more manageable and minimised the effects of evaporation because they were put over a liquid bath that enhanced the humidity. In addition, utilising floating LM decreased the effect of gravity on cell aggregation at the LM bottom, while the movement of the marble across the surface of the supporting liquid enhanced the mixing process within the LM. This action proved essential for producing spheres of uniform size.

Recently, LMs were demonstrated to be suitable micro-bioreactors for inducing oocyte maturation in vitro [46]. In addition, it was indicated that LMs has great potential for additional reproductive biology applications, including oocyte fertilisation [54] and individual embryo cultivation [55]. Reduced reagent consumption [56] and low contamination risk [57] have been recognised as advantageous features of a LM.

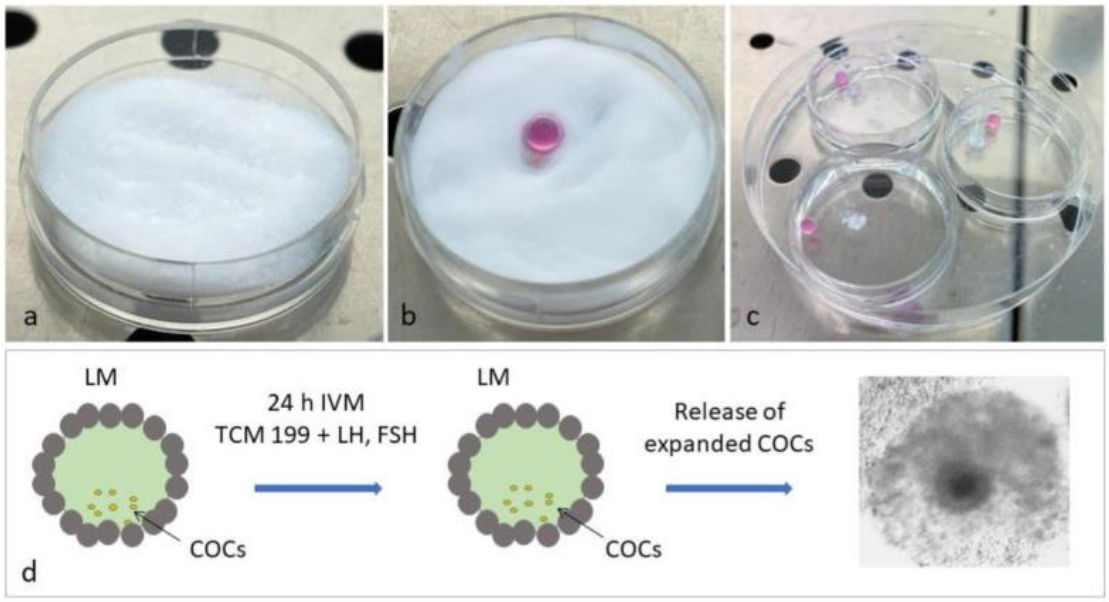

Figure 8 Preparation of liquid marbles (LM) containing COCs. (a) A hydrophobic Cab-O-Sil/Cabot powder bed is prepared in a 35-mm Petri dish. (b) 30 µL of IVM medium, containing 10 COCs, are dispensed over the hydrophobic Cab-O-Sil/Cabot powder bed. The IVM drop is gently rolled over the powder to be fully coated with the Cab-O-Sil/Cabot particles. (c) The resulting LM drop is placed in a new 35-mm Petri dish positioned inside a larger Petri dish containing sterile water to prevent evaporation. (d) Schematic representation of IVM in Cab-O-Sil/Cabot powder LM. [58]

2.1.4 Diagnostic Assays

Using LMs as microreactors has provided considerable benefits for lowering the usage of chemical reagents, making chemical reactions more cost-effective. The use of diagnostic assays is a key application in the biological sector. Authors Arbatan et al. [59] have shown that LMs can be utilised as bioreactors for rapid blood typing, utilising human blood groupings ABO and Rh to illustrate the use of LMs as a micro-bioreactor for the diagnosis of human blood.

The LMs were created by rolling blood droplets over a bed of hydrophobic precipitated calcium carbonate. Per test, three sets of marbles with distinct antibody solutions were created and injected into the LM. The ABO and Rh blood groups were established by observing whether a haemagglutination response occurred, as evidenced by a difference in colour between two sections of the marble. Separation was confirmed by observing a light-red and dark-red zone within the LM, with the darker zone resulting from the agglutinated red blood cells precipitating at the LM's base, showing the presence of the antigen [60]. The absence of a colour difference indicated that the relevant antigen was not present. Using the results of the experiment, blood grouping could be identified, which is an important step prior to blood transfusions to prevent fatal incompatibility. The use of LMs as micro-bioreactors has the advantages of requiring a minimal quantity of chemicals, reducing biohazards, being inexpensive and consequently disposable [61].

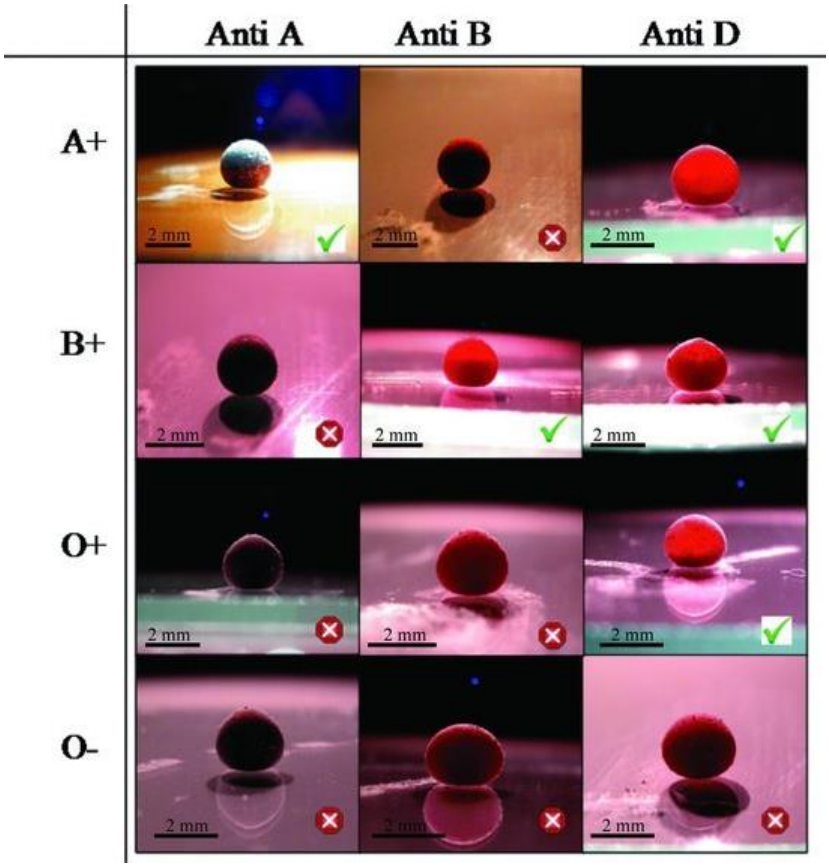

Figure 9 Summary of blood typing results after the corresponding antibodies are injected into the marble microreactor (20 µL). Green ticks are added to the photos where the separation of agglutinated RBC is observed. The cross signs are added to photos where agglutination caused colour separation is not observed. [59]

Zhao et al. [36] reported that LMs are an appropriate platform for biological experiments. On the basis of electrochemical measurements, a new approach for the quantitative detection of dopamine in LMs was investigated. They hypothesised that this technique may be utilised to diagnose neurological illnesses affecting brain functions [36].

2.1.5 Drug Screening

Since LMs permit the injection and extraction of controlled amounts of liquid without compromising their structure, Oliveira et al. [62] demonstrated that LMs can be utilised for high-throughput drug screening. Concurrently, the LM's liquid environment was engineered to accommodate the cultivation of anchorage-dependent cells that require physical support to adhere and proliferate.

In order to achieve this objective, microparticles were injected into the liquid environment to provide the necessary cell anchoring sites for cell adhesion [63]. After preparing the LM with a mixture of cells and microparticles and allowing the cells to adapt during an incubation time, a pharmacological or chemical agent was administered into the micro-bioreactors. Several circumstances could be analysed and compared through the injection of a reagent that changes colour in response to a specific biological response. This was conceivable since the LMs were translucent. This colour monitoring was accomplished by collecting photos from LM, followed by image processing to produce the data. This new technique's reproducibility was fully tested by comparison to a well-known conventional method [64]. This approach might have an influence on high-throughput drug screening in 3D cell culture systems, where findings can be obtained using colorimetric and non-destructive measurements [65].

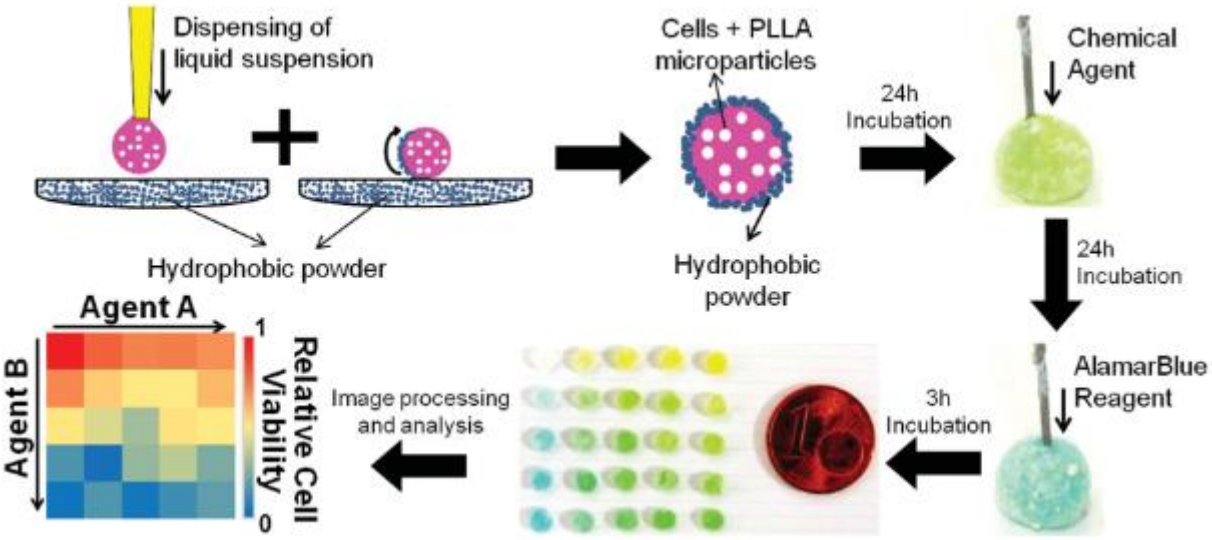

Figure 10 The proposed method for using liquid marbles (LM) in high-throughput drug screening is depicted in a schematic. First, a predetermined volume of cell suspension containing modified PLLA microparticles was dispersed over a bed of hydrophobic powder and then incubated for 24 hours. Chemical substances (drugs) to be examined can then be injected. After a new incubation period, AlmarBlue reagent can be introduced into the LM to assess cell vitality by colour change. By doing image processing/analysis on photographs of the LM, the colour intensity was measured, and a heat map containing the results can be created. [62]

Due to evaporation, injection, and extraction of liquid, the size of the LMs may alter during the assays. However, steps can be implemented to address this issue, such as producing an environment of saturated water vapour or assuring a constant volume of LM through the use of accurate measurement devices, such as pipettes.

Oliveira et al. [62] and Zhao et al. [36] demonstrated the ease of use of the LM in drug/biological screening applications and "online" electrochemical/optical detection, respectively. LM show great potential for high throughput applications. Nevertheless, significant advancements are required in the automation of operations, as all procedures are currently based on manual manipulation.

2.1.6 Cryopreservation

The cryopreservation of mammalian cells is an emerging use for LMs. Serrano et al. [66] demonstrated LMs as an effective alternative to the standard technique for the cryopreservation of a mammalian cell line, without the use of cryopreservative chemicals. Due to the cytotoxic effects of typical cryopreservative chemicals such as dimethyl sulfoxide and glycerol, modest concentrations must be used [67]. Two conventionally inspired techniques were employed: rapid freezing by immersion in liquid nitrogen and slow cooling to -80 °C using a typical freezing container. LM were made by rolling droplets of a highly concentrated cell solution (produced with foetal bovine serum) over poly(tetrafluoroethylene) powder. The LMs were then kept in a frozen state for 15 days. The integrity of the LM was found to be intact after freezing, and the following cellular parameters were assessed: viability, morphology, proliferation, size, complexity, and cell cycle. In this application, the droplet volume and cell concentration proved to be the determining criteria for successful LM use.

The authors discovered a safe range of droplet volume and cell concentration: 5–30 µL and (0.52) x 105 cells μL^{-1}, respectively. LMs reached the same degree of performance as normal freezing techniques for all investigated cellular metrics after achieving these limitations [68].

2.1.7 Hydrophobic Shell Removal

Removing the coating particles from the LM to gain access to the liquid core to query its biological and chemical status has proven to be difficult. Attempted techniques that achieve this include the use of optical radiation [12], ultrasonic fields [13], and timed disintegration with wettability change [14]. The success of these approaches is generally dependent on several physical factors, such as the characteristics of the liquid, the wetting properties of the liquids and particles, the delivery of motive forces through actuators, and the design of equipment necessary to provide the non-contacting fields. A method that neglects such considerations would allow applications for use as an effective, reusable reactor [69].

2.2 Liquid Drops and Surface Wetting

2.2.1 Wettability and Contact Angle

Wettability is a fundamental concept in LM research. It refers to the capacity of a liquid to maintain contact with a solid surface. The equilibrium between adhesive and cohesive intermolecular interactions governs this. The fundamental characteristic of liquids behave on surfaces is contact angle. A liquid with a lower degree of wetting has a larger contact angle and more liquid-liquid interaction strength (cohesion) than solid-liquid interaction strength (adhesion). A liquid with a contact angle greater than ninety degrees is considered hydrophobic. It should be noted that the changes in wetting interactions are gradual-rather than abrupt.

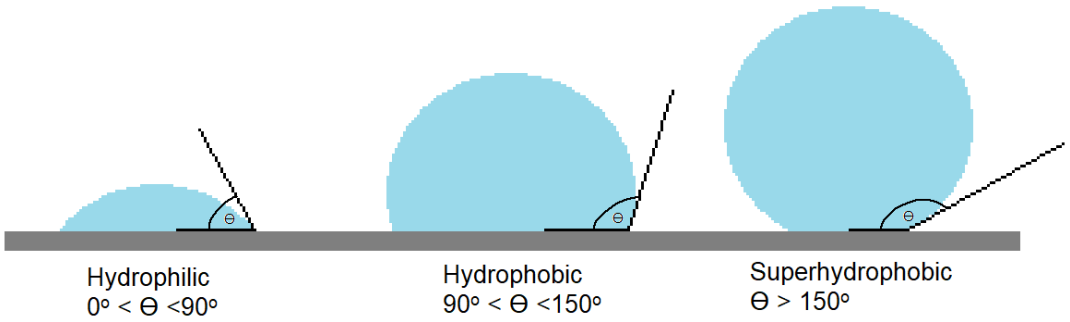

Figure 11 Different regimes depending on the contact angle of the droplet on the surface.

On a superhydrophobic surface, where water has virtually no affinity, the contact angle of a water droplet can exceed 150 degrees. The manner in which wetting affects the contact angle can be described using the Wenzel and Cassie-Baxter equations.

2.2.2 Wenzel Wetting

The Wenzel equation establishes a relationship between surface tension and surface roughness and the contact angle of a liquid droplet forming on a solid surface. Using this equation, the contact angle is given by

$$\cos(\theta_w) = \frac{r(\gamma_{sv}-\gamma_{sl})}{\gamma_{lv}} = r\cos(\theta) \quad (1)$$

where θ_w is the contact angle formed, r is the roughness factor, γ is the surface tension at the interface with SV, SL, LV representing the interfaces between solid, liquid and vapour and θ represents the contact angle of liquid droplet on a smooth flat surface at equilibrium, also known as the Young's contact angle. This equation is typically applied to homogenous wetting regimes, where the liquid enters the gaps caused by surface roughness.

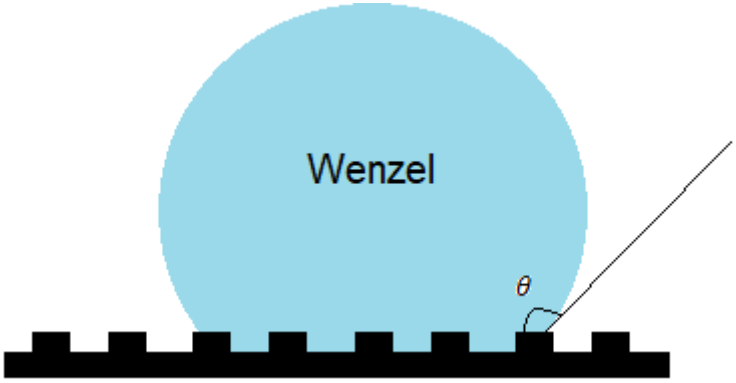

Figure 12 Wenzel wetting sceme where surface roughness is accounted for in the equation of contact angle

2.2.3 Cassie-Baxter Wetting

The Cassie-Baxter equation [70] relates the ratios of SV interface with respect to the total area of SL and LV interfaces, such that

$$\cos(\theta_{cb}) = \varphi_s \cos(\theta) + \varphi_s - 1 \quad (2)$$

where φ_s is the ratio of total area of SL interface to the total area of SL and LV interfaces. θ_{cb} is the contact angle given by the Cassie-Baxter equation. The Cassie-Baxter equation is applied to heterogenous cases where air bubbles are trapped inside the gaps. This equation shows that the contact angle will increase when the surface is roughened. As the stable wetting state can either be homogenous or heterogeneous, thus both equations can be used to model the contact angle of the LM.

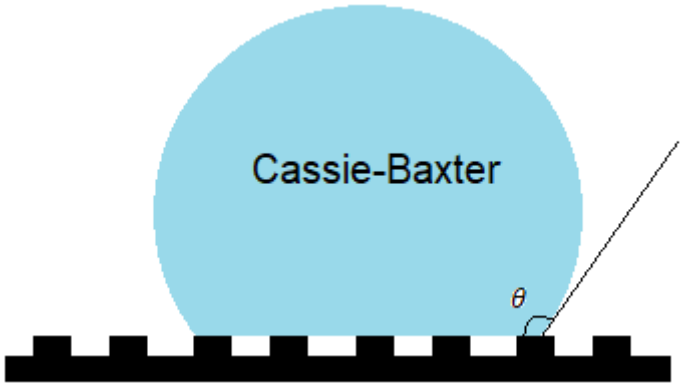

Figure 13 Cassie-Baxter wetting scheme relating the ratio of the solid-vapour interface with the total area of the solid-liquid and liquid-vapour interfaces

2.2.4 Surface Free Energy

The mechanics of the attachment of the outer layer particles can modelled by replacing a portion of the droplet's liquid-air, solid-air interfacial area with the solid-air interfacial area across the region of particle attachment [71].

The net surface free energy change per particle attaching to the droplet is given by

$$\Delta F = A_{SA}(\gamma_{SL} - \gamma_{SA}) - A_{LA}\gamma_{LA} \quad (3)$$

Using Young's Law for the interfacial surface tension, we have

$$\cos(\theta_e) = \frac{\gamma_{SA} - \gamma_{SL}}{\gamma_{LA}} \quad (4)$$

This yields an equation for the net surface free energy change that is given by

$$\Delta F = -A_{SA}\gamma_{LA}(\cos(\theta_e) + \frac{A_{LA}}{A_{SA}} \quad (5)$$

The ratio of liquid-air to solid-air interfacial area is (1-cosθ)/2, which is always positive. This infers that the surface free energy when the particle is attached to the liquid-air interface is always reduced, resulting in the process being energetically favoured.

There has been a wide variety of powders used to create LMs [72]. Particles can be hydrophobic or hydrophilic, with the contact angle of the attached particle varying accordingly. The Young's contact angle of a highly hydrophobic powder, such as polytetrafluoroethylene particles, is larger than 90 degrees, whereas the Young's contact angle of a hydrophilic powder, such as graphite, is

less than 90 degrees. In both instances, a favourable energy outcome is reached when the particle is attached to the outer shell of the liquid droplet, allowing the formation of the LM.

2.3 Colloidal Drops

Colloidal drops or particle-laden drops arise when particle interactions occur within the liquid or at the liquid-solid interface. This is known as a colloidal mixture, a suspension of solid particles in a liquid. As particle size decreases, the correlation between colloidal behaviour and the ratio of surface area to volume increases [73]. In 1861, Thomas Graham tested the ability of dissolved chemicals to diffuse in water through a permeable barrier and determined that only crystalline solids, but not colloids, could pass through. Subsequently, it was discovered that any substance could be subdivided into particles of colloidal size (1 nm to 1 μm) and categorised as a colloid. The range of sizes of colloidal particles is determined by their linear dimensions or atomic number [74].

Colloidal particles can range in morphology from corpuscular to rod-like to disc-like to thin films or long filaments. In the case of corpuscular particles, the diameter is utilised to determine the colloidal size; nevertheless, in all other circumstances, a system is regarded to be colloidal if one of its dimensions falls within the range.

Colloidal materials have large surface areas and, consequently, high surface energy as the size of colloidal particles is between the atomic and bulk dimensions. Colloidal systems are heterogeneous and consist of two phases: the dispersed phase and the dispersion medium. Both the phase that generates the particles and the particles themselves are referred to as dispersed phase. The phase in which particles are spread is known as dispersed media.

2.3.1 Drying of Colloidal Drops

The formation of complex patterns during wetting and drying of colloidal drops is commonly observed phenomenon in our daily life, which is also involved in numerous research and industrial fields such as inkjet printing [75], spray coating [76], and medical practice [77]. Unlike liquid drops that dry and disappear from surfaces, the fact that particles are present in colloidal drops mean that various patterns are formed when they are dried out. These include cracking patterns, crystal patterns, ring-stain patterns, and uniform-deposition patterns. The difference in desiccation patterns is mainly due to the different physical processes experienced by colloidal droplets during its wetting and drying stages. The complexity of the colloidal fluid system and the interactions between the system and substrate play an integral role in the differences in patterns observed.

Evaporation spontaneously occurs when the partial vapour pressure in the environment around the sessile drop is lower than the saturation pressure. This is driven by the diffusion of molecules in the volatile solvent in the case of colloidal droplets. Simultaneously, heat and mass convections occur within the droplet which builds up a local flow field. Two important flow fields are proposed to occur within the colloidal droplet during drying: capillary flow and Marangoni flow.

Capillary flow is a compensation flow caused by the differential evaporation rates during drying along the interface of the droplet [78]. A colloidal droplet resting on a hydrophilic surface will have its contact line pinned during drying, causing the local evaporation rate to be enhanced. This forces the liquid in the central part of the droplet to flow outwards in order to replenish the faster liquid loss at the edges, resulting in a horizontally outward capillary flow within the droplet [79]. The radius of the droplet remains constant, whilst the contact angle decreases. The rate of decrease is high due to the higher evaporation rate of the colloidal droplet. It also results in the three-phase contact line to be pinned faster and the capillary flow within the sessile drop to be stronger. Consequently, the rate of capillary flow during drying increases along with the evaporation rate of the colloidal droplet.

When coffee droplets are spilt onto a solid substrate, a ring-shaped deposit of coffee solids will be found around the edge of the dried droplet. This is known as the “coffee ring” effect which is a hydrodynamic process due to the capillary flow in the droplet. Since the enhanced evaporation rate at the pinned contact line of the droplet generates the horizontally outward capillary flow, the

suspended materials are carried to the edge. After the evaporation process, the solid materials are concentrated at the edge forming the “coffee ring” at the perimeter of the droplet [80].

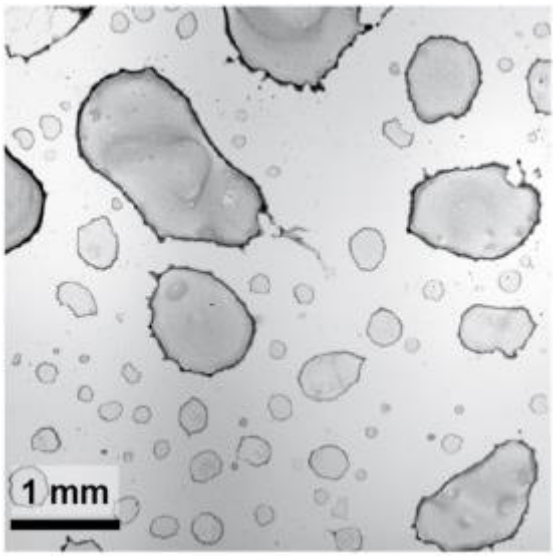

Figure 14 Transmission optical microscopy image of particle deposits obtained after a complete dissolution of a sessile water droplet [80]

A key mechanism in the coffee stain effect is the Marangoni flow. It is a convection flow that is driven by the droplet’s surface tension gradient. The surface tension gradient can be caused by the differential concentration of substances (suspended particles) or the non-uniform distribution of local temperature fields [81]. During drying of colloidal suspensions, the liquid evaporation causes a local variation in the concentration of solid particles and generates a surface tension gradient along the liquid-air interface [82]. Subsequently, the liquid in the lower surface tension regions will get pulled towards the higher surface tension regions, resulting in Marangoni convection. Hu and Larson [82] presented the features of Marangoni flow in a colloidal drop wherein the liquid near the base of the sessile drop is pulled upwards to the drop, and then transported downwards. This causes circular movement along the liquid-air interface. The local surface tension of liquid in a colloidal droplet can be decreased by increasing the local temperature, which causes Marangoni flow to occur to non-uniform distribution of temperatures [79].

Clearly, the drying of colloidal drops is highly differentiated than the drying of liquid marbles. In the latter, the particulates remain at the surface of the diminishing drop throughout the process. For that reason, coffee stains are not observed when liquid marbles are evaporated.

2.3.2 Applications with Colloidal Drops

Despite the structural differences between a colloidal drop and a liquid marble, the colloidal drop can also play an important role in biological applications [83]. It has been shown in the previous section that drying a drop of colloidal solution leaves a ring-like structure of the colloidal particles – a ‘coffee ring’. In Surface enhanced Raman Scattering (SERS), high signal enhancement can be reached in the coffee-ring area; however, reproducibility cannot be expected [84]. Recently, many studies have attempted to understand and avoid formation of the coffee ring [85]. Xie et al. [86] described a method that allows reproducibly obtaining self-assembled monolayers of Au nanorods by controlling humidity and temperature of the drying environment. Furthermore, the wettability and temperature of the substrate on which the colloid drop is casted has great influence on how the nanoparticles settle [87, 88]. All of these factors should be considered when preparing SERS substrates by drying the metal nanoparticle colloids. It has been found that enhancement effects of various drop-dried colloidal substrates with differently shaped silver nanoparticles can result in optimal experimental conditions for detection of uric acid in aqueous solutions by means of SERS [84].

2.4 Frozen Drops

The phase transition from liquid to solid that occurs when a water droplet on a cold plate reaches its freezing point is known as the solidification of the droplet. Frosting is a commonly seen phenomena during the solidification process, which is evident in heat extraction of air in heat pumps [89]. There are four primary stages in the process of droplet icing on a cold surface [90]: pre-cooling or supercooling, recalescence, freezing, and cooling or tempering. In the first stage, pre-cooling or supercooling, the initial cooling temperature of the droplet approaches the nucleation temperature. The second stage is recalescence, in which the temperature of the liquid water rises abruptly due to the latent heat release from the ice, reaching the solidification temperature. Subsequently, in the third stage, freezing occurs, when the droplet gradually hardens at a steady temperature. The final stage is the cooling stage, in which the droplet's temperature begins to decline.

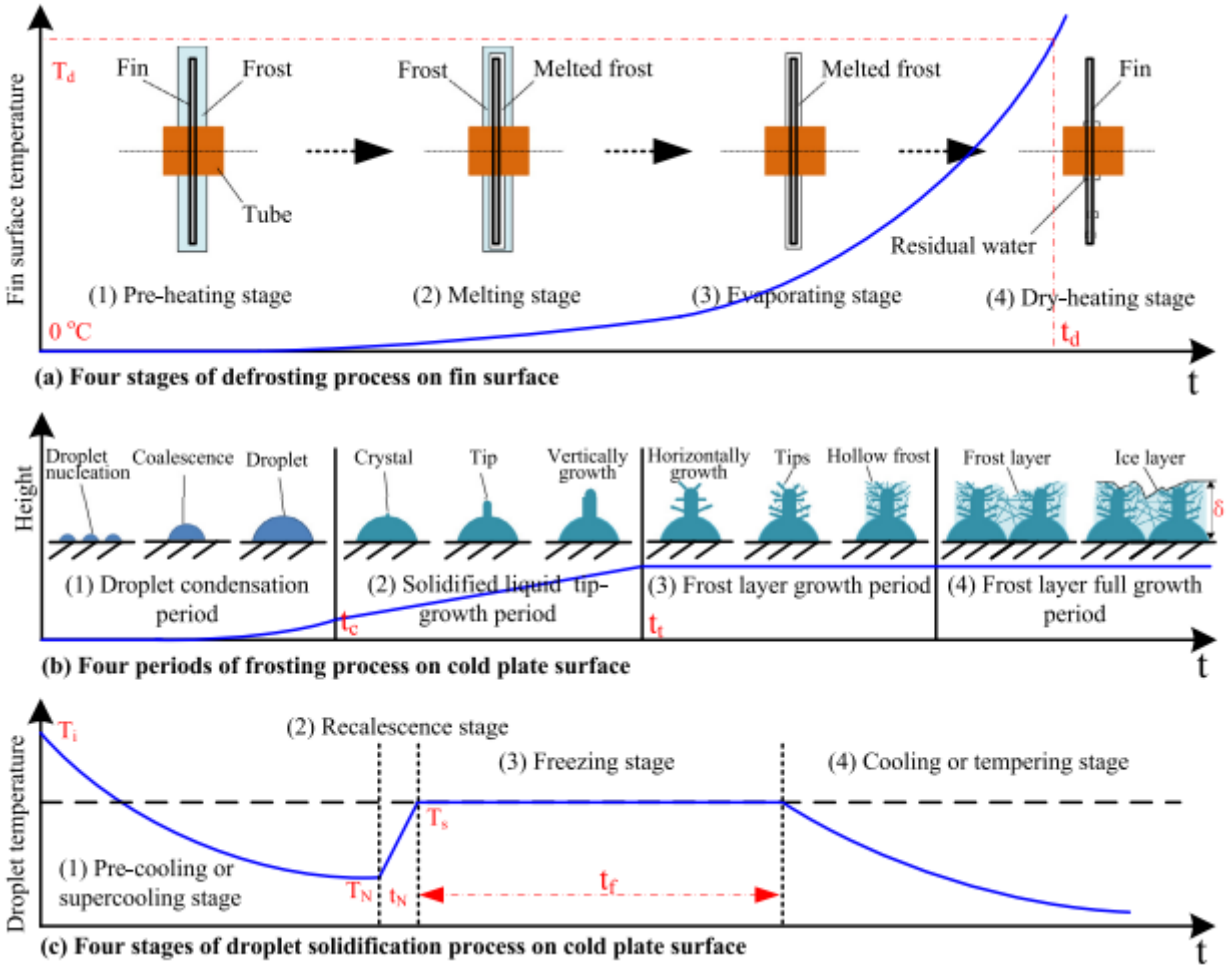

Figure 15 Stages of defrosting, frosting and solidification [91]

2.4.1 Nucleation

Nucleation is typically a random process, making it extremely challenging to pinpoint the initial location of ice nucleation in a water droplet. There are two alternative forms of ice nucleation: homogeneous nucleation, in which the nucleation rate is proportional to droplet volume, and heterogenous nucleation, in which the nucleation rate is related to the interface's surface area [92]. Evaporative cooling of a droplet on an isothermal plate produces uniform nucleation at the liquid-gas interface. The first nucleation location of a sessile water droplet placed on a hydrophilic cold plate was similarly seen to be random [93]; nevertheless, it always occurs near the three-phase contact line, where the temperature is the lowest. Due to the surface being the source of cooling, the liquid-solid interface temperature is significantly lower than that of the remainder of the droplet.

Due to the fact that water has a higher thermal conductivity (0.59W/m.K) than air (0.026W/m.K), air functions as a thermal insulator for the droplet throughout the freezing process. As a result, the temperature of the three-phase contact line lowers faster than other sites on the liquid-solid interface.

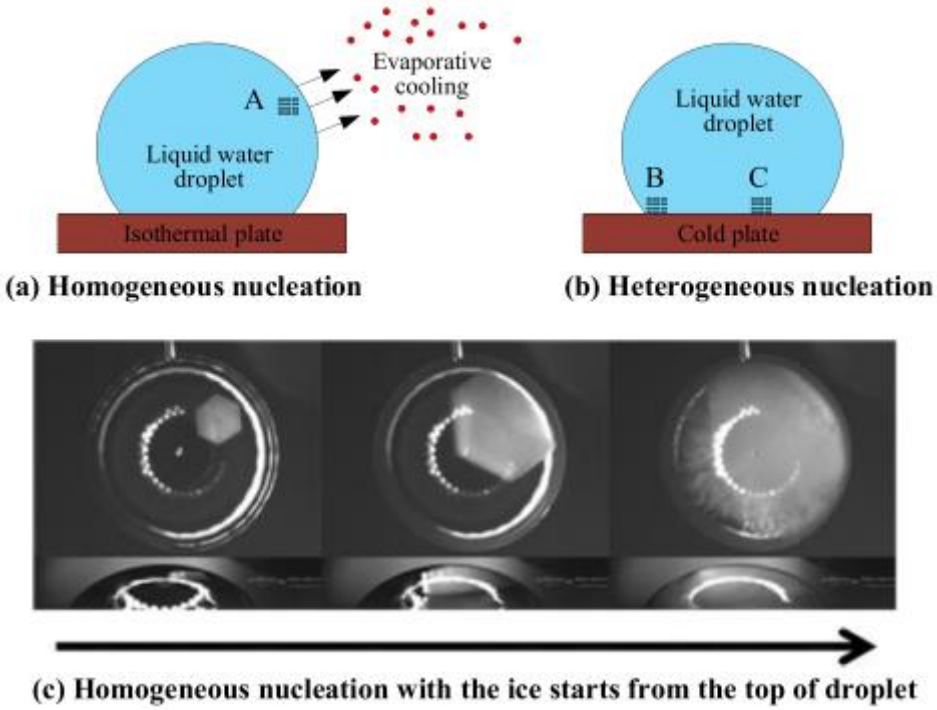

Figure 16 Schematic depicting the two possible modes of ice nucleation in a water droplet [93]

Experiments on a microscale are typically conducted in laboratories as they offer greater control precision and stability. Due to the decrease in homogeneity as the liquid-solid interfacial area grows, homogenous nucleation can only be utilised at micro-scaled interfaces. Authors Hikina et al. [94] designed an experiment to examine the method's scaling constraints. They produced tiny droplets with contact surfaces ranging from 10^{-12} to 10^{-6} m^2. Ice nucleation was characterised by a quick shift in the droplet's form. Clearly, the scale limitation of the homogeneous nucleation regime is 10^{-10} m^2, meaning that uniform ice nucleation can only be characterised when the contact area is less than this limitation.

2.4.2 Opaqueness

At the recalescence stage, the droplet becomes opaque for two probable reasons. The first is the phenomenon of light being refracted as it travels through the droplet. When a droplet freezes, it contains a mixture of ice and water with different refractive indices of 1.333 and 1.31, which alters the direction of light [95]. The second cause of opaque frozen droplets is air bubbles trapped in ice. Blanchard et al. [96] demonstrated that trapped air bubbles in ice led the water droplet to become opaque, confirming the hypothesis that the refractive phenomenon of light in the confined air bubbles is responsible for the droplet's opacity.

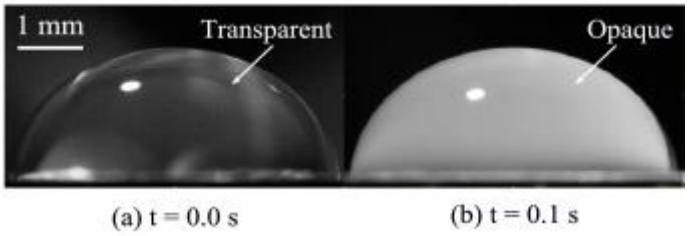

Figure 17 Sessile water droplet freezing on a cold plate surface [97]

Since air is less soluble in ice than it is in water, extra gas enters the liquid as ice forms, increasing the concentration of air dissolved in water. As this air gets supersaturated, bubbles form on the

ice's surface; when light strikes these smaller bubbles, scattering occurs, causing the droplet to appear opaque.

2.4.3 Deformation and Shape Change

As a water droplet freezes, its average density falls and its overall volume increases [98]. It has been demonstrated that when a droplet is frozen, its height also increases [98, 99]. When water freezes at 0°C, its volume rises by around 10% under air pressure [98], despite the fact that a spherical droplet should only expand by 2.15 % due to its radius alone. Chang et al. [100] examined the expansion ratio of the droplet's width and height relative to its diameter. The height expansion ratio was observed to fluctuate between 1.16 and 1.24, whereas the radial expansion ratio stayed constant at 1.00.

When a droplet is placed on a cold surface, the freezing front begins at the bottom [101]. Before the interface reaches the drop's peak, a sharp tip rather than a spherical form is noticed, which signifies the beginning of the vertical development phase of the solidified liquid tip. This phenomenon could be explained by the lower density of ice compared to water [102]. Using peanut oil, whose solid and liquid densities are comparable, Wang et al. observed [102] that the frozen droplet lacked a sharp edge. It was discovered that the centre and border of water droplets have varied freezing front growth rates, since the heat conductivity of ice (2.2 W/m.k) is significantly greater than that of water (0.569 W/m.k) [98], leading to the increasing rate of the edge freezing front.

Nauenberg et al. [103] observed that the freezing front became increasingly concave rather than flat. A small crater would emerge in the upper part of the solid phase where the liquid phase was confined, confirming that the curvature of the freezing front must increase as freezing progresses and the volume of the frozen phase expands. Since the radius of the frozen crater must eventually fall to zero, this factor also contributes to the creation of the pointed tip of the frozen droplet.

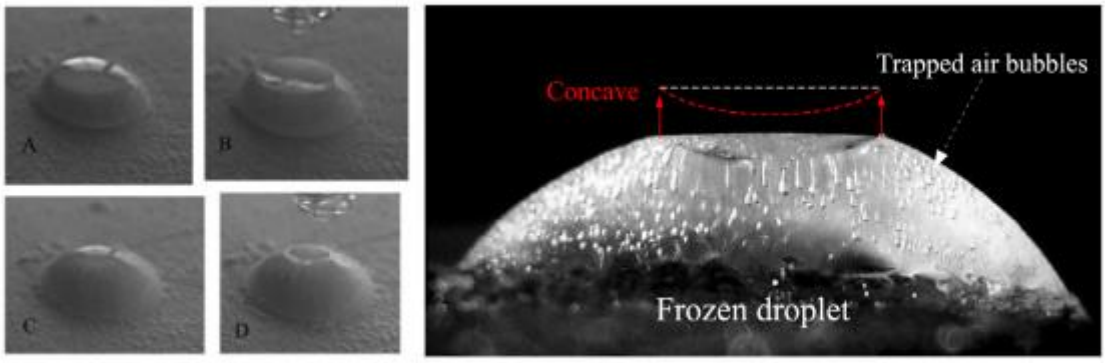

Figure 18 Freezing front of a water droplet on cold plate surface [103]

The evolution of the freezing front during the freezing process provides investigative value. There are eight typical surface crystallisation conditions, consisting of a mix of the same or different angles, curves, and curvatures. Each combination results in a unique freezing rate; for instance, a concave-shaped freezing front has the highest freezing rate due to its larger Gibbs free energy barrier [104].

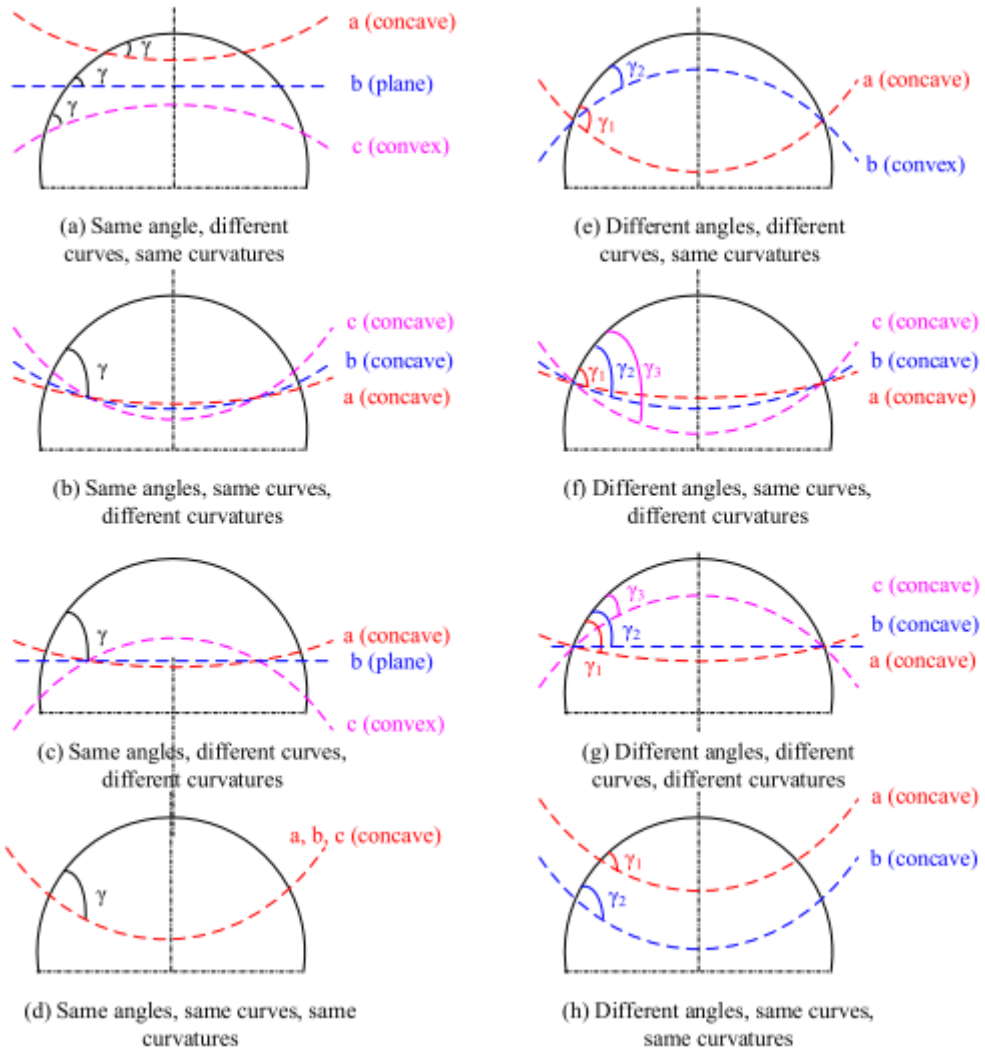

Figure 19 Eight different conditions of surface crystallisation of a water droplet [91]

2.5 Gas Bubbles

A bubble residing in a liquid contains a mixture of vapour and permanent gas. Hao et al. [105] investigated the effects of gas diffusion into a growing vapour bubble, the slowed condensation process, and the growth enhancement by rectified diffusion. There are two destabilising mechanisms, the first of which is kinematic in nature and occurs during bubble contraction, while the second is dynamical in character and occurs when the compression of the bubble content slows the inward motion of the bubble wall. It is commonly acknowledged that the gas bubble is stable as long as the interface's velocity and acceleration are minimal.

Initial research examined the collapse of a bubble in 10K-subcooled water at normal pressure [105]. Three conditions were studied: a bubble of pure vapour at 90 °C, water saturated with CO^2 at 100 °C, and 25 °C, respectively. In the presence of dissolved gas, the collapse of the bubble was significantly slower. Due to the importance of latent heat in supplying the effective stiffness of a vapour bubble, there were significant rapid and severely damped oscillations of bubble size at the beginning of the testing [106]. Initial collapse provides latent heat to the surface of the bubble, which raises the temperature above saturation, briefly reversing the collapse and increasing the pressure. As the bubble grows in size, its surface cools, resulting in a decrease in pressure and contraction. These oscillations were severely dampened, resulting in a quasi-equilibrium condition in which the surface temperature is stabilised at saturation.

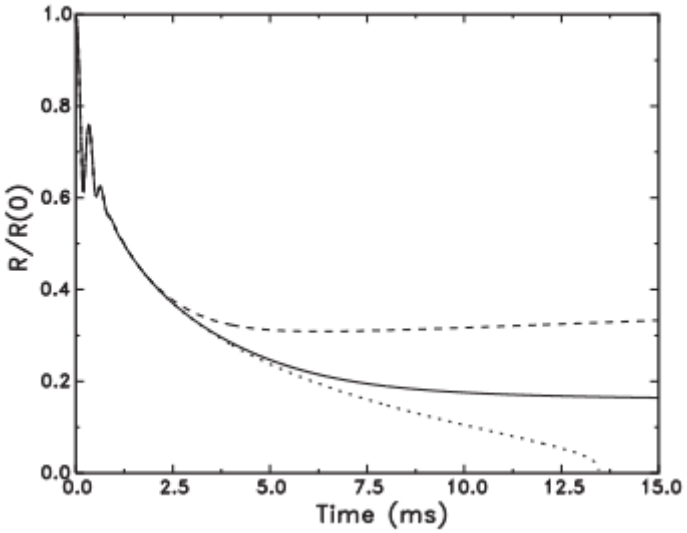

Figure 20 At 90°C and 101.3 kPa of ambient pressure, a pure vapour bubble in water devoid of dissolved gas collapses rapidly (dotted line). The collapse is significantly slowed by the presence of dissolved CO^2 in the liquid. The solid line represents water saturated with CO^2 at 100°C, while the dotted line represents water at 25°C. In this later instance, the liquid is supersaturated at 90°C and after the condensation of the vapour, gas diffusion causes the bubble to develop [105]

In the second experiment, a superheated bubble was subjected to low pressure for a brief period of time. This represents the situation in flow boiling where bubbles pass over regions of low pressure. As the pressure is reduced, the partial pressure of the gas decreases, causing the bubble to rise quickly. As a result of the following pressure recovery, the vapour rapidly condenses and the radius decreases. Subsequently, the contraction of the bubble is halted and then reversed due to an increase in vapour pressure caused by the release of latent heat, which raises the bubble's surface temperature, and the compression of the gas. At this stage, the total pressure in the bubble approaches the ambient pressure. Since this pressure is the sum of the gas and vapour pressures, the gas at the bubble surface is now undersaturated, and a concentration gradient causes the bubble to develop slowly when gas diffuses into it.

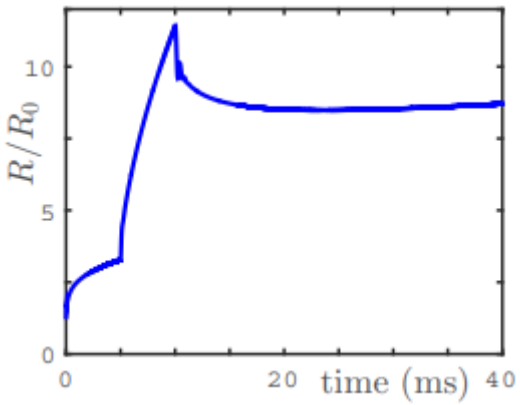

Figure 21 Radius vs time of a gas-vapor bubble in CO2-saturated water at 100 ◦C and 101.3 kPa. The liquid temperature is 100 ◦C and the ambient pressure 101.3 kPa except for 5 ms <t< 10 ms, when it is reduced so that the liquid is superheated by 5 ◦ C. The initial bubble radius R0 is 100 µm [105]

It was discovered that the bubble's total gas mass increases by an order of magnitude, with its radium being double its initial value [105]. When subcooled, this generates visible tiny bubbles to boil away from heated places. The gas mass fraction decreases during the early phase, which is attributable to the faster diffusion of heat relative to mass, indicating that bubble expansion is mostly due to vapour formation [107].

In the final portion of the investigation, the growth rate of an oscillating bubble containing pure vapour was compared to that of a bubble containing both gas and vapour. Even a modest proportion of noncondensable gas accelerated the expansion of the bubble through rectified diffusion [108]. The process is caused by the accumulation of non-condensable gas near the bubble wall at the beginning of the compression half-cycle. A concentration boundary layer functions as a barrier to permit further condensation of vapour. The vapour must diffuse across a gas-rich boundary layer close to the surface of the bubble, while vapour formation at the interface is unimpeded.

3. Liquid Marble: Creation, Content Removal, & Applications

3.1 Preamble

The literature review conducted found that while considerable amount of work had already been done to study liquid marbles, there are specific areas that can be further advanced. This chapter details the investigations that have been conducted in terms of the creation, liquid content removal and applications using liquid marbles.

More specifically, section 3.2 discusses a new method of using brushes to create liquid marbles in a more controlled manner. The original method of LM creation involves dispensing a liquid droplet on a bed of hydrophobic powder and rolling it about [6]. However, generation of large amounts of LMs in quick succession can be difficult to achieve. Using cosmetic brushes to transfer particulate from the bed to the bristle, then from the bristle to the liquid-gas interface of the droplet was first analysed theoretically. Van der Waal forces and surface tension forces were considered to determine that the favourable outcome of the force balance is the particulates transferring onto the interface. This was then proven in the subsequent experiments, where LMs and Janus liquid marbles (JLMs) were successfully created using the new 'brush-on' technique.

In section 3.3, investigations done to use the method in section 3.2 to create JLMs are outlined. JLMs have the potential to improve the functionality of LMs in applications. JLMs have predominantly been created by coalescing two individual liquid marbles [7-9], however a method of dropping liquids onto separate powder beds sequentially has also been attempted [10]. These approaches have drawbacks in that they cannot create JLMs in a controlled and uniform manner. The mechanics needed for JLMs with good separation between different types of particles to be created was investigated in this section. It also presented a preparation method, with further development on the particle transfer aspect, is amenable for high throughput JLM production.

Section 3.4 details studies on how the liquid contents of the liquid marble can be extracted using capillary tubes. It has been proven challenging to remove the covering particles from the LM in order to reach the liquid core and determine its biological and chemical state. The utilisation of optical radiation [12], ultrasonic fields [13], and timed disintegration with wettability change [14] are some of the methods that have been tried to accomplish this. However, the characteristics of the liquid, the wetting properties of the liquids and particles, the delivery of motive forces through actuators, and the design of the equipment required to provide the non-contacting fields are physical factors that can affect the effectiveness of these approaches. This section details a method of evacuation using capillary tubes. By placing one end of a capillary tube in contact with the overhanging component, controlled drainage of liquid from the droplet could be achieved. Such a method makes it relatively simple to examine the contents of the LM without unintended transfer of the enclosing particles.

Finally, in section 3.5, a new method for particle separation based on the wetting characteristics of the particles that make up a liquid marble was investigated. Current techniques of particle separation include use of membranes [109] and coagulation-flocculation [110]. The former is subject to fouling, whereas the latter operates with the solid particles already in solution. When separation of particles in their solid state is required, exploiting the differences in wetting characteristics can be used, therefore a separation technique that achieves this would be greatly useful. This section investigates the use of LMs created in the form of pendant and sessile drops to achieve particle separation based on their differential wettability. The method permitted the wetting particles to be separated into the liquid core which is then easily withdrawn into capillary tubes for analysis without any need for actuator motive forces or careful design of specialized equipment.

3.2 Brush Creation of Liquid Marbles

3.2.1 Introduction

The original method of LM creation involves dispensing a liquid droplet on a bed of hydrophobic powder and rolling it about [6]. This has remained as the most popular method for creating LMs since it can be done with minimal instrumentation. Agitating the particulate bed using mechanical forces from vortex mixing has been reported to improve the repeatability of LM creation [111]. Furthermore, agitation using electrostatic forces have also been explored [28, 112], whilst a two-step approach of controlled impact of liquid drops onto one particulate bed and then onto another particulate bed has been shown to create Janus liquid marbles (JLM) [10]. JLMs can be exploited to display multi-response characteristics, with the use of magnetic forces to allow for rotation and transportation on solid substrates and liquid water surfaces.

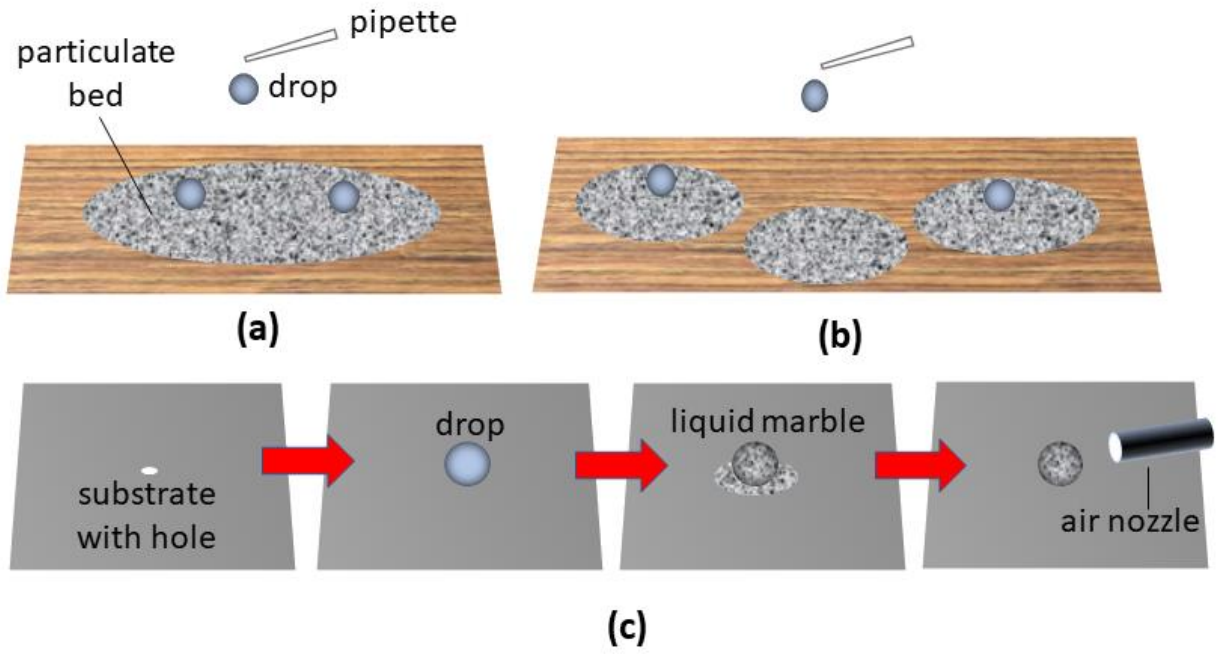

Figure 22 In the classical method for LM formation, (a) drops of liquid are dispensed on the particulate bed and moved around. The dispensation of drops onto separate particulate beds (b) helps to limit transfer of material from one liquid body to another. A method that eschews the use of multiple particulate beds (c) involves dispensing a drop on a non-wetting substrate with hole, depositing particulates on the drop followed by removal of excess particles by blowing or by suction using an air nozzle. [11]

Generation of large amounts of LMs in quick succession can be difficult to achieve. Discharging multiple liquid drops onto a single particulate bed (Fig. 22a) followed by agitation to form the outer shell can result in contamination through material transference from one liquid body to another. This can be undesirable especially when the LMs are used in applications of microbioreactors for the cell culture, viruses or bacteria. Coalescence between subsequent liquid drops may be avoided by depositing the drops onto separate particulate beds (Fig. 22b) followed by agitation instead, however this method can result in significant wastage since only a small amount of particles will be consumed to form the LM. With the recent concerns over the negative health impacts of airborne particulate matters [113, 114], there is a clear motivation of reducing particulate usage during LM generation to minimize their wastage to the environment.

An improvement on the LM generation involves dispensing a liquid drop on a highly non-wetting substrate with a small hole, followed by deposition of powders over the drop and removal of excess particulates by air dislodgement or vacuum aspiration using an air nozzle. Even though this technique prevents material transfer between droplets and reduces particulate wastage to some extent, uniform powder coverage and depinning of the LM during air dislodgement remains a challenge to overcome.

Brushes have been applied since ancient Rome [115] to transfer cosmetic powder from a containment bed to the skin. It is possible to ensure highly uniform and optimal distributions of particulates over the skin surface when the correct brush material and application technique is used. Brush feeders, operating in the same manner on industrial scales, have been applied for the transfer and dispersal of light, fluffy or low sphericity particulates [116].

Van der Waals forces due to adhesion of solid particles to solid surfaces and surface tension forces (attraction of solid particles to liquid-gas interfaces) are theoretically analyzed in the context of creating LMs and JLMs. Subsequently, experimental work has been done to directly transfer the particulates onto the liquid drop using a cosmetic brush to form the LM and JLMs. Experiments were also conducted to simulate and estimate the effect of the applied “brush-on” forces on the stability of the stationary liquid drop.

3.2.2 Theory

3.2.2.1 Adhesion of Spherical Particles to a Cylindrical Rod

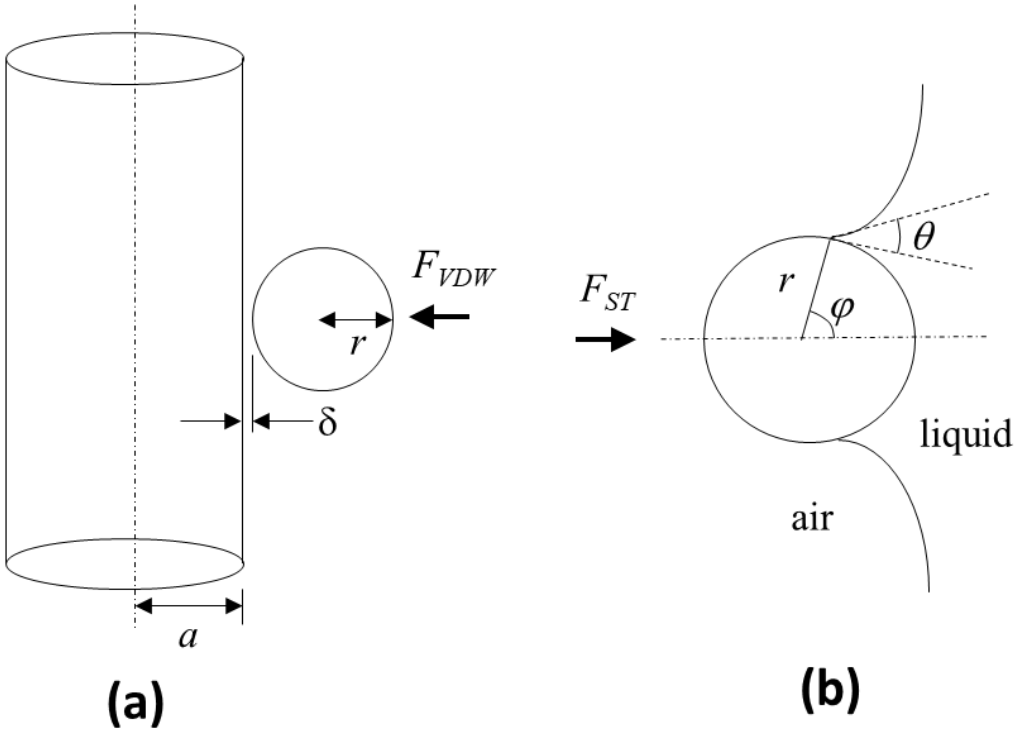

Figure 23 (a) Van der Waals forces F_{VDW} that allow particle adhesion to the brush bristles can be modelled as a sphere of radius r separated by a distance δ from the surface of an infinitely long cylinder with radius a. (b) Surface tension forces F_{ST} that facilitate particle adhesion to the liquid-gas interface is governed by the filling angle φ in relation to the contact angle θ and sphere radius r. [11]

During the interaction between micron-sized solid particles and dry solid bristles of a brush, the Van der Waals forces (F_{VDW}) are the primary forces in determining their mutual adhesion [117]. An appropriate model to apply is that of a spherical particle of radius r interacting with an infinitely long cylindrical rod of radius a (see Fig. 23(a)). Suppose that the number of molecules per volume unit is n_c and n_s for the cylinder and sphere, respectively. The interaction potential between a molecule of the cylinder with that of the sphere can be expressed as

$$\emptyset = n_s \int_{V_s} \frac{\alpha}{\rho^6} dV_s \tag{6}$$

where α = London-van der Waals constant, ρ = distance of molecules between two interacting bodies, V_s = volume of the sphere, V_c = volume of the cylinder. The energy resulting from the interacting potential is given by

$$E = n_c n_s \alpha \int_{V_s} \int_{V_c} \frac{dV_s dV_c}{\rho^6} = n_c \int_{V_c} \emptyset(r) dV_c \quad (7)$$

from which the interaction force can be determined using [118]

$$F_{vdw} = \frac{2AR^3}{3ax^2(x+2R)^2} \quad (8)$$

where A = Hamaker constant, δ = separation distance between sphere and cylinder, $R = r / a$, $x = \delta / a$.

Leite et al. [119] has approximated the Hamaker constant for the interaction of mediums 1 and 2 across medium 3 using

$$A \cong \frac{3}{4} k_B T \frac{(\varepsilon 1-\varepsilon 3)(\varepsilon 2-\varepsilon 3)}{(\varepsilon 1+\varepsilon 3)(\varepsilon 2+\varepsilon 3)} + \frac{3hv_e(n_1^2-n_3^2)(n_2^2-n_3^2)}{8\sqrt{2}\sqrt{n_1^2+n_3^2}\sqrt{n_2^2+n_3^2}[\sqrt{n_1^2+n_3^2}\sqrt{n_2^2+n_3^2}]} \quad (9)$$

where where kB = Boltzmann's constant (1.380649×10^{-23} $m^2kgs^{-2}K^{-1}$), T = temperature in Kelvins, h = Planck's constant ($6.62607015 \times 10\text{-}34$ m^2kgs^{-1}), v_e = mean frequency, ε_i = dielectric constant for medium i, and n_i = refractive index of medium i.

3.2.2.2 Adhesion of Solid Particles to Liquid-Gas Interface

For LM creation, it is necessary for the solid particle to transfer from brush bristle to the liquid-gas interface of the liquid drop. The surface tension force (F_{ST}) plays a primary role in this (Fig. 21b). For a solid sphere of radius r interacting with a liquid-gas interface with surface tension γ, the surface tension force is given by

$$F_{ST} = 2\pi\gamma r \sin\varphi \sin(\theta + \varphi) \quad (10)$$

where φ = the fill angle and θ = contact angle.

The calculations to determine the Van der Waals forces using Eq. (8) required knowledge of the Hamaker constants. Polyester (material of the brush fiber) and air were taken to be media 1 and 3 respectively, giving $\varepsilon_1 = 2.9$, $\varepsilon_3 = 1.006$, $n_1 = 1.56$, $n_3 = 1$. Based on a mean frequency $v_e = 6 \times 10^{14}$ Hz and temperature T = 298 K, having talc as the particle, in which $\varepsilon_2 = 1.8$ and $n_2 = 1.56$, gives $A = 1.75 \times 10^{-20}$ J using Eq. (4). Having graphite alternatively as the particle, in which $\varepsilon_2 = 12$ and $n_2 = 2.7$, gives $A = 3.89 \times 10^{-20}$ J using Eq. (9). As illustrated in Figure 24a, van der Waals forces were found to fall off steeply with increase in the separation distance (even at the nanometer range) between the sphere and cylinder, with virtually no difference between the talc-polyester and graphite-polyester cases.

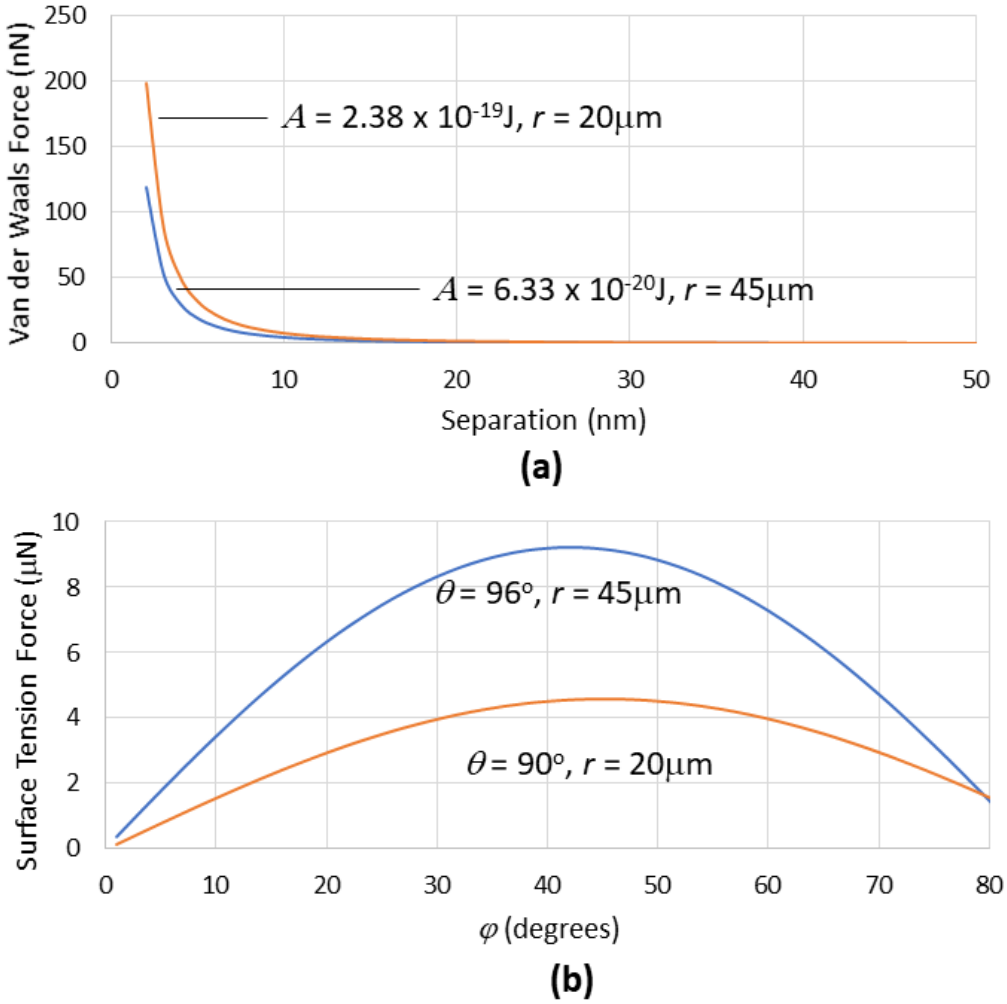

Figure 24 (a) Van der Waals forces generated between a cylinder with radius = 500 µm interacting with spheres having different radius r and Hamaker constants at various separation distances (between sphere and cylinder). These forces were much lower than (b) surface tension forces that are generated with spheres of different radius and contact angles at various filling angles. [11]

The calculations for surface tension forces using Eq. (10) alternatively were based on the use of contact angles of 96º and 90º for talc [120] and graphite [121] respectively, determined previously by experimentation. As shown in Figure 22b, the surface tension forces were significantly higher with talc than with graphite, although the contact angles for both materials were similar, which shows sphere radius contributes greatly to the magnitude of surface tension forces. The surface tension forces (in the micro-Newton range) were much higher than the Van der Waals forces (which were in the nano-Newton range), which would make the transfer of particles from the bristles to the gas-liquid interface of the drop favourable.

3.2.3 Materials and Methods

The substrate was prepared by using candle soot, collected by placing an inverted beaker over a burning candle for 12 minutes, yielding around 900mg of soot. 15mL of absolute ethanol was then poured into the beaker and thoroughly mixed using an ultrasonic cleaner (PS-20A, SUNNEX) for 5 minutes to synthesize the soot solution. Transparent polyvinyl chloride (PVC) slides (75 mm x 25 mm) of 0.5 mm thickness with holes of 2mm diameter were roughened (service provided by Dextech Technologies Pty Ltd) to high degrees of uniformity. The slides were then sprayed with the soot solution using a compressed air driven air brush (Paasche, VL).

Drops of 10 µL volume deionized water were dispensed above the holes on the substrate. Cosmetic applicator brushes (Oxx Cosmetics) were then used to transfer hydrous magnesium silicate (Talc) powder (Sigma, 86255; average size 45 µm) as well as graphite powder (Sigma,

282863; average size 20 µm) to the drops to create LMs and JLMs. The bristles of the cosmetic applicator brush were made from polyester and had an average radius of 500 µm.

To simulate the force effect of brush on liquid drop stability, drops of 10 µL volume deionized water were dispensed onto the holes on the substrate via a pipette. A rectangular thin foil of length L, width w and thickness t, created from material with modulus of elasticity E, is dangled vertically with its top end clamped firmly in position (see Fig. 23a). A thin substrate made of hydrophobic material is attached to the free end of the foil. When the substrate with drop is moved towards the foil, the latter will deform elastically. The force F_f imposed by the foil on the drop can be estimated from the deflection of the free end Δ using [122]

$$F_f = \frac{3EI\Delta}{L} \tag{11}$$

Wherein I the second moment of area is given by

$$I = \frac{wt^3}{12} \tag{12}$$

The contact angles, advancing and receding, of the drop were analysed by recording a time sequence of images with a camera as the thin foil contacts with the drop. The contact angles were measured using an imaging analysis software (ImageJ). The contact angles and drop shapes after specific levels of force interaction were also similarly monitored.

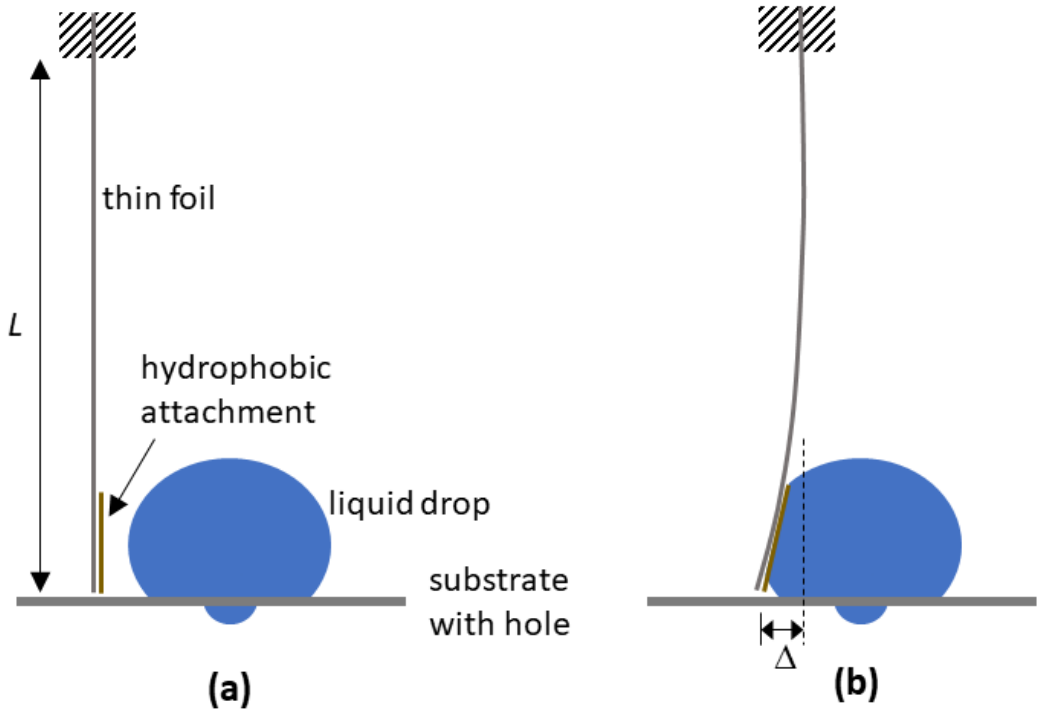

Figure 25 The experiment to simulate the effect of brushing on forces on drop stability (a) involved using a thin foil of length L dangled with its top end clamped firmly in position, and its bottom free end having a hydrophobic attachment. When the liquid drop is moved towards the foil and pushes against it, the free end of the foil undergoes lateral displacement Δ allowing the interaction force to be estimated. [11]

Figure 25 shows application of the theoretical calculations above, where it is evident that brush bristles in its dry state can collect a decent amount of talc particles from the powdered bed, and the majority of the particles can then be efficiently transferred to the liquid-gas interface of a drop.

3.2.4 Results and Discussion

The images presented in Figure 26 clearly indicate the ability to create LMs and JLMs using the proposed technique. The distribution of particles on the liquid-gas interface were more uniform, the process more readily conducted, and less particles were wasted compared to previously reported methods. Since the drop is stably pinned to the hole of the substrate, it is reasonable to create an array of drops onto the substrate followed by the brushing on of particles. This suggests a possibility of automating the process to increase LM and JLM production throughput.

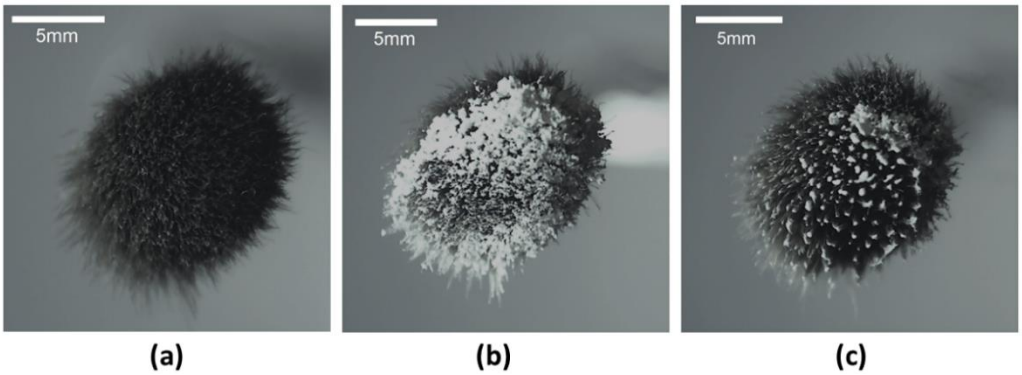

Figure 26 Images of the cosmetic brush used in (a) its parent state, (b) following contact with a talc powder bed, and (c) after transference to the liquid-gas interface of a drop by contact. [11]

A potential challenge that may arise during this automation process is the possibility of drop deformation and depinning from the hole when the interaction forces are applied. Experiments using a dangling thin foil provided a quantitative measure of the force magnitude applied. It was found that regardless of the stiffness of the foil, it was not possible to sweep the drop away as a single body. Instead, a portion of the liquid drop was deformed and squeezed under the foil, generating one of two contact lines (see Fig. 28a). This behaviour can be attributed to the force being applied to one interface of the liquid body (from its left), rather than to the entire body, differing from the case when the substrate is tilted for gravitational forces to act on the whole liquid body. In addition, the liquid core used was water which shows low shear stress resistance, further exacerbates this phenomenon. More viscous or non-Newtonian fluids may allow the displacement of the drop as a single body.

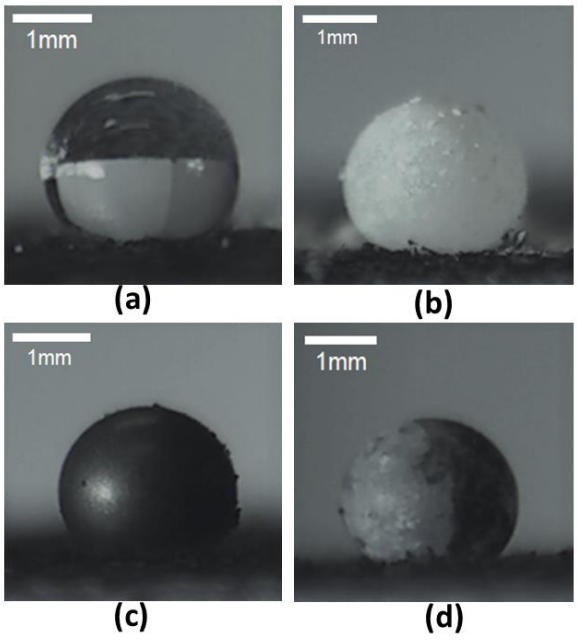

Figure 27 Images recorded of (a) a liquid drop. Using the proposed brush on method on the drop, LMs were created with (b) talc and (c) graphite particles, as well as (d) Janus LMs were created with talc and graphite particle encapsulation at the left and right sides respectively. [11]

A change of droplet shape is undesirable, therefore an assessment of drop stability after the application of brush-on forces is needed to determine if any shape change occurs (see Fig. 28b and c). From a series of experiments conducted, it was found that forces under 1 mN caused no change to the original contact angles of the drop, which becomes the critical limit of applied particle brush-on forces to create LMs and JLMs.

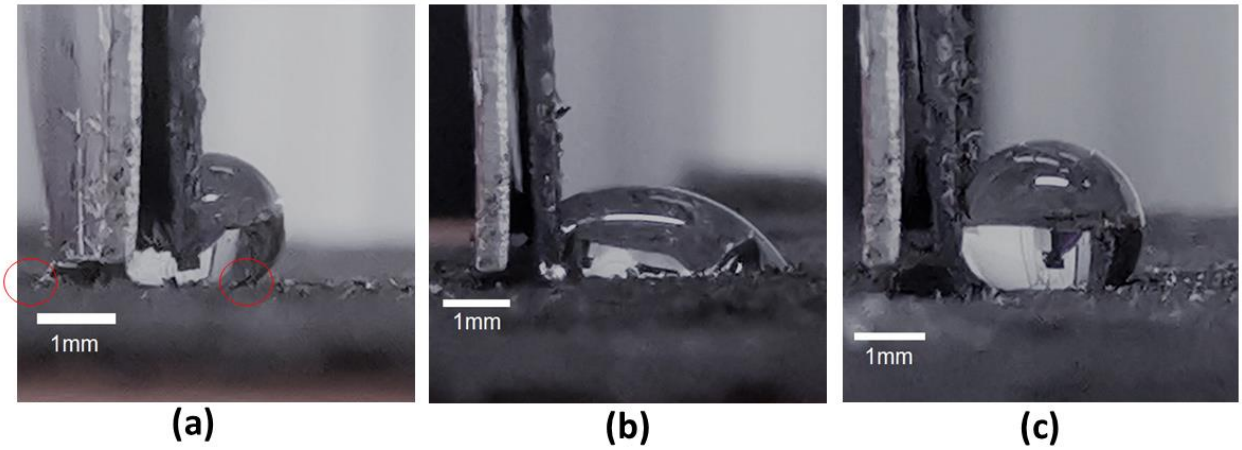

Figure 28 When interacted with the dangling thin foil, part of the body of the drop is always squeezed under the foil (a) creating contact lines on the left and right (indicated as red circles). When the applied interaction force is relatively large and then released (b), the drop undergoes a departure from its initial shape and contact angles. Such a departure is eschewed when the applied interaction force is limited and then released (c). [11]

The process of moving the dangling foil to contact with the drop, and the force experiments on the drop produced unique contact angle trends at the left and right contact lines as shown in Figure 29. The droplet had an average contact angle of 135^{o} before any force was applied. When the foil just contacts with the drop, (force = 0), the left contact line exhibited slightly larger average contact angles (142^{o}) compared with the right contact line (131^{o}) (see Fig. 29(a) and (b) respectively). This seemingly counterintuitive outcome is due to the capillary flow of liquid squeezing into the gap between the foil and substrate, causing the left and right contact angles to be advancing and receding respectively. As the force application increases, the contact angle at the left contact line reduced greatly, reversing its role from being advancing to receding.

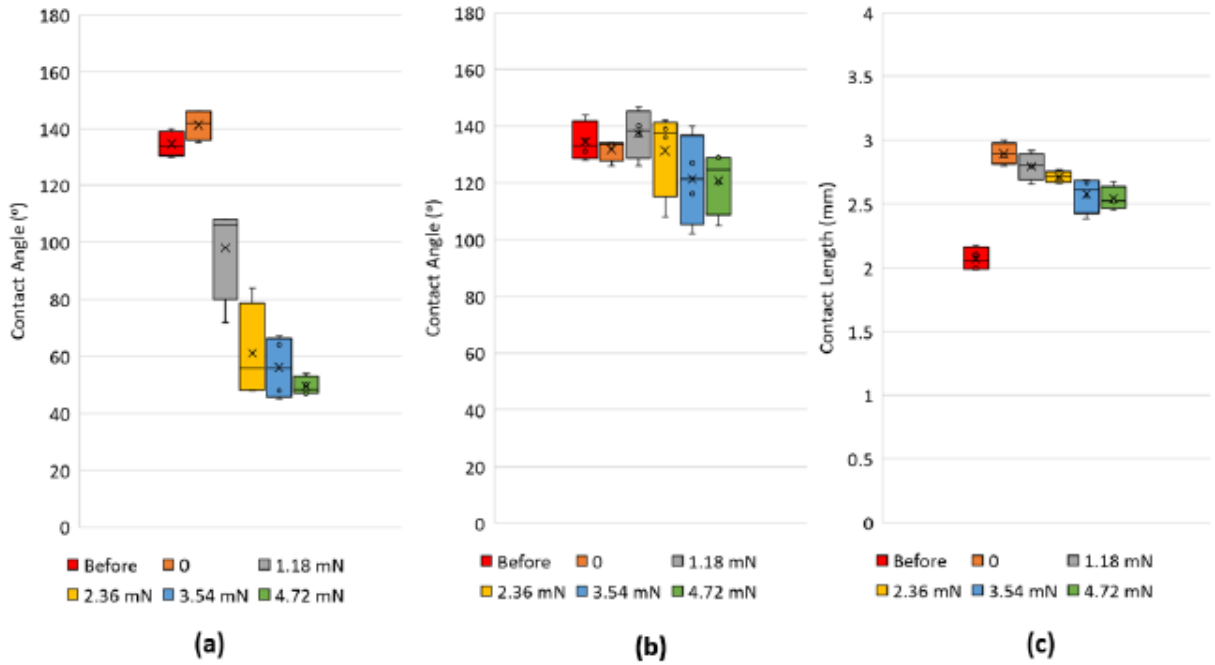

Figure 29 Box plots of the contact angles measured at the left (a) and right (b) contact lines as well as contact length (c) before the foil contacts the drop, just when the foil contacts the drop, and when the foil imparts different levels of forces on the drop. Each plot is based on 5 separate readings. [11]

As a result, the contact angle at the right contact line now switches from receding to advancing. This seems to follow the mechanics of a sessile drop that is being progressively tilted. It should be noted, however, that the contact angle of the right contact line is reduced as the applied force increases, although more marginally, from the equilibrium contact angle (see Fig. 29b). With drops on inclined surfaces, the advancing contact angle is always greater than the equilibrium contact angle. This behaviour indicates a mechanism in which the bottom part of the liquid body (indicated by a virtual horizontal line that runs along the lowest part of the foil) was trying to accommodate to the force perturbation differently from its upper part. The former was essentially trying to “spread” itself to take advantage of its adhesion forces to the substrate, whereas the latter was attempting to adjust its shape in the absence of any adhesion forces. A similar demonstration of drops undergoing separate behaviours at its top and bottom was reported previously in another application context [123, 124].

3.2.5 Conclusions

A novel approach to create LMs with better control and reduced wastage was explored in this chapter. Using cosmetic brushes to transfer particulate from the bed to the bristle, then from the bristle to the liquid-gas interface of the droplet was first analysed theoretically. Van der Waal forces and surface tension forces were considered to determine that the favourable outcome of the force balance is the particulates transferring onto the interface. This was then proven in the subsequent experiments, where LMs and JLMs were successfully created using the new ‘brush-on’ technique. This approach can be automated to allow for high throughput create of LMs with minimal wastage, allowing new opportunities in LM such as biological screening to access for viable cells through colour change [62].

The findings in this section have been published in E Lin, Z. Song, J.W. Ong, H.A. Abid, O.W. Liew, T.W. Ng, Brushed creation of liquid marbles. PeerJ Materials Science 4 (2022) e24.

3.3 Stable Brush Creation of Janus Liquid Marbles

3.3.1 Introduction

As highlighted in section 3.2, the unique architecture of LMs has enabled it to be used in a wide variety of important applications [125-128]. With Janus liquid marbles (JLMs), where the encapsulating particles are of different types, there is potential to extend the functionality of LMs even further. JLMs have predominantly been created by coalescing two individual liquid marbles [7-9], however a method of dropping liquids onto separate powder beds sequentially has also been attempted [10]. These approaches have drawbacks in that they cannot create JLMs in a controlled and uniform manner.

In section 3.2, it was found that brushing particles onto a liquid drop that was located stably on a strongly hydrophobic substrate with a hole is able to create LMs in a controlled fashion [11]. In this section, the underlying mechanics needed to develop JLMs in a controlled manner are outlined and a new approach to do so is described and demonstrated.

3.3.2 Theory

The mechanics involved in the transfer of a particle onto a semi-spherical sessile drop is considered first. In the case of a solid spherical particle of radius r located at the apex of the liquid-gas interface (position a in Fig. 30A), the gravitational, buoyancy, surface tension and pressure forces that act can be given respectively by

$$F_G = \frac{4}{3}\pi\rho_S g r^3 \tag{13}$$

$$F_B = \frac{1}{3}\pi\rho_L g r^3(2 - 3\cos\alpha + \cos^3\alpha) \tag{14}$$

$$F_{ST} = -2\pi\gamma r \sin\alpha \sin(\theta - \alpha)\mathbf{n} \tag{15}$$

$$F_P = \pi r^2 \sin^2\alpha \left(\frac{2\gamma}{R} - \rho_L g Z\right)\mathbf{n} \tag{16}$$

where ρ_S = particle density, g = gravitational acceleration, ρ_L = liquid density, α = the filling angle between the drop-particle centreline and the connecting line from the particle centre to the three-phase contact, γ = surface tension, θ = contact angle between liquid and particle, and $\mathbf{n}$ = the unit vector directed away from the centre of the drop to the particle's centre, R = radius of the drop, and Z = height difference between the drop apex and the centre of the three-phase contact line.

When the particle is at the apex position of the drop, it can remain stationary there despite the values of F_G, F_B, F_{ST}, and F_P not being equal to each other, as long as $F_G + F_{ST} = F_B + F_P$. However, this is difficult to maintain when the particle is at any other location b (Fig. 30A). Particles typically have higher densities than liquids, and the displaced liquid volume should always be smaller than the volume of the sphere, consequently $F_G > F_B$. If turning moments are taken about the centre of the sessile drop, a resultant torque will develop that moves the particle towards the drop's three phase contact line.

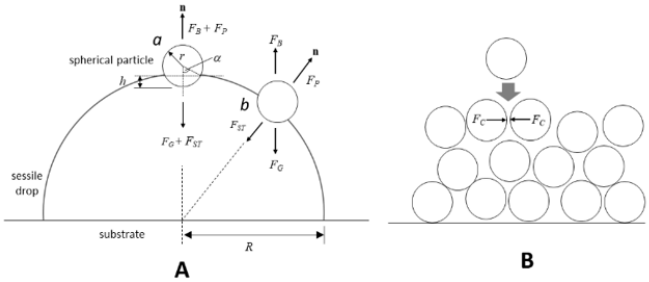

Figure 30 The location of a spherical particle at the liquid-gas interface of a sessile drop (A) is determined by gravity, buoyancy surface tension, and pressure forces (F_G, F_B, F_{ST}, and F_P respectively). A particle is located exactly at the apex a of the drop is able to remain stationary there through a balance of forces. At any other location b, however, where $F_G >$

F_B, a resultant torque will direct the particle towards the three-phase contact line of the drop. The size of the particle relative to the drop has been exaggerated to visualise the action of forces. As the particles accumulate upwards at the three-phase contact line, capillary attractive forces F_C holds each particle to its neighbour (B). Perturbations of the local curvature of the liquid-gas interface will cause incoming particles to be inserted into the interstices of the existing particle assembly that would engender poor control in the creation of the Janus liquid marbles.

As these particles accumulate upwards from the contact line, each particle is attracted to its neighbour by capillary forces (F_C) (see Fig. 30B). In models advanced for particles floating on liquid surfaces, this force has been found to depend on the local curvature of the liquid-gas interface [129, 130]. Hence, the transfer of new particles via the brush's bristles at the particle assembly's proximity can "insert" incoming particles at the interstices of the existing particle assembly rather than to "stack" above it. A preponderance of such events will stymie the controlled formation of JLMs.

3.3.3 Materials and Methods

3.3.3.1 Substrate Creation

The substrate was created using the same method as described in chapter 3.2.3.

3.3.3.2 Experimental Method

The method proposed here has a liquid drop first dispensed and seated stably on a hydrophobic substrate with a hole (Fig. 31A) [11, 20, 127]. This drop is then fully encapsulated with type I particles via their application with the bristles of a mini brush close to the apex of the drop (Fig. 31B). The insertion of tip at the apex then fills the drop with liquid with type I particle partially but uniformly filling its bottom (Fig. 31C). A second application of type II particles near the apex using the mini brush then completes the JLM construction (Fig. 31D).

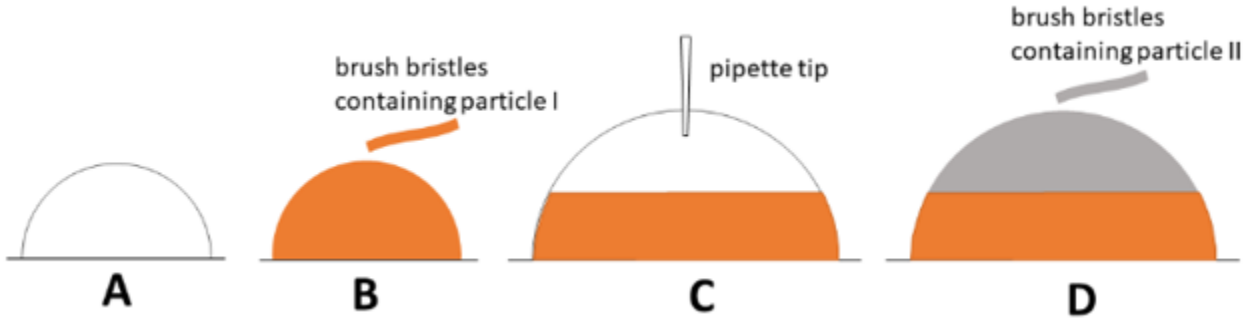

Figure 31 Proposed controlled Janus liquid marble creation method in which a liquid sessile drop (A) created on a hydrophobic substrate with a hole, will be encapsulated with type I particles following transfer using brush bristles near the drop's apex (B). The delivery of additional liquid via a pipette tip has the type I occupying the base of the drop (C), wherein which type II particles can be transferred using brush bristles near the drop's apex to create the Janus liquid marble (D).

3.3.4 Results and Discussion

An experiment was conducted using Talc particles (Sigma, T2015) where clusters of particles of various sizes were transferred to the drop. Their movements were tracked using a high-speed camera (Fastec) operating at 250 frames per second. A positive correlation trend between particle cluster velocity (towards the base of the drop) and surface area coverage was found (Fig. 32). This finding supports the model advanced where the turning moment of the particle cluster about the centre of the drop was primarily responsible for the downward travel, (since a larger cluster size would approximate to a sphere with larger radius, thereby causing the value of F_G - F_B to be larger).

However, significant data spread was observed despite this trend nonetheless. In addition, the trend was no longer observed for area sizes in excess of 0.18 mm^2, wherein a stochastic

distribution was obtained. These observations may be accounted for by considering that particle clusters can assume one of two different forms: as aggregated spheres or monolayer island granules. It should be noted that the use of imaging for assessment here, provides a measure of the surface area coverage rather than the volume of the cluster. Clusters of smaller area sizes would tend to display an architecture closer to that of a single sphere with varying radius as depicted in the model. This then explains why the speed versus area trend was observable (notwithstanding the spread) when the area size was below the threshold of 0.18 mm^2. From an application standpoint, the transfer of more particles with each application of the mini brush should accumulate and build up the liquid marble more quickly.

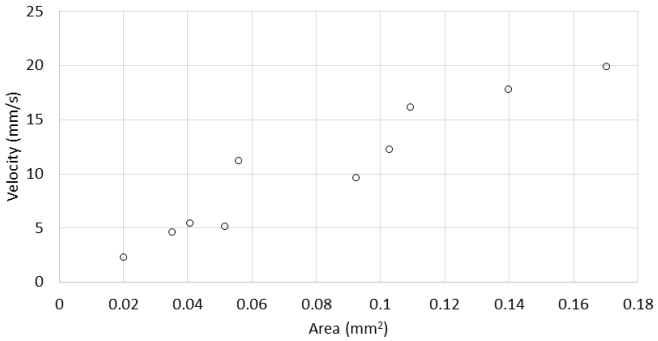

Figure 32 Graph of travel speed against the measured area of the cluster size of the Talc particles after transfer to the drop using the mini brush. The trend supports the model of the particle cluster moving down due to the action of a turning torque about the centre of the drop.

Figure 33A shows a 10 µL deionized (DI) water drop initially dispensed above the hole on the substrate that was fully encapsulated with copper powder (Sigma, 266086) following their transfer using brush bristles close to the drop's apex. Subsequently, an additional 10 µL of DI water was dispensed, the encapsulating copper particles clearly segregated to occupy only the bottom section of the drop, mimicking a "friar tuck haircut" appearance (Fig. 33B). After a second transfer using the brush bristles close to the drop's apex, this time with graphite powder (Sigma, 282863), a JLM with the copper and graphite particles clearly separated was achieved (Fig. 33C). The method of JLM creation was then repeated, but this time with the brush bristles transferring the graphite particles further away from the apex of the drop. In this case it was found that JLM generated was no longer composed of the clear separation of the copper and graphite particles (Fig. 33D). This result confirmed the hypothesis that strong perturbations of the local curvature of the liquid-gas interface would more likely permit the graphite particles to "insert" into the interstices of the copper particle assembly rather than to "stack" above it.

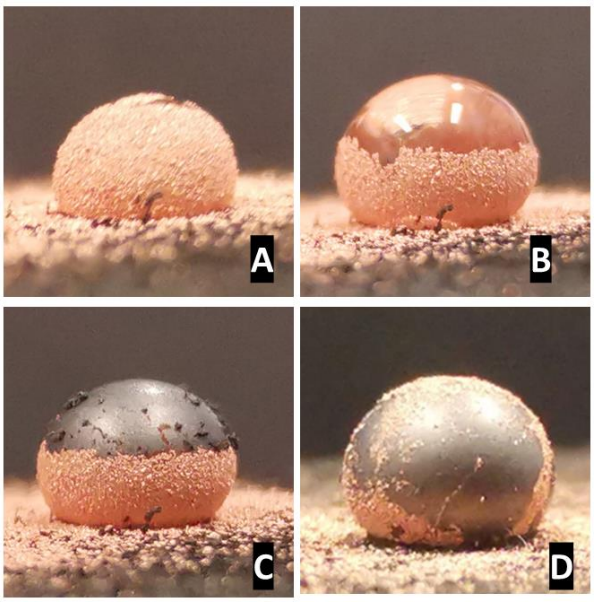

Figure 33 A 10 µL water drop dispensed on the substrate that was encapsulated by copper particles through brush transfer from its apex (A). An addition of 10 µL of water through a pipette tip caused the copper particles to accumulate

at the bottom (B) from which a second brush transfer of graphite particles from the apex created a Janus liquid marble with the two types of particles well segregated (C). A separate attempt with the method but with particles brush transferred away from the apex produced a Janus liquid marble with the two types of particles poorly separated.

While the method was demonstrated here using a brush transfer approach, it is envisaged that other more efficient ways of particle delivery may be devised to increase production throughput. Since the substrate is thin, a large array of JLMs could be produced concurrently, using the brush bristles, allowing for a higher throughout of JLMs. The essential requirement however will be for the delivery to cause as little perturbation as possible and at the apex of the drop.

As strongly hydrophobic substrates tend to allow liquid drops dispensed on them to displace more readily, the use of a substrate with a hole here provides the additional positional stability needed for the JLM creation process. There has been considerable interest in understanding the mechanics of how LMs are stressed when they deflate. Not surprisingly, these studies are based on the LM undergoing evaporation [129-131]. The presence of the hole in the substrate conveniently permits for the insertion of a capillary tube there to draw liquid from the JLM in a highly controlled manner as an alternative to evaporation, which is dependent on environmental conditions.

Figure 34 The removal of liquid from the Janus liquid marble via the substrate's hole tends to disrupt the uniform separation of the graphite and copper particles at the outset. The final outcome, however, is a structure that strong deviates from a sphere.

From studies conducted (Fig. 34), it was found that despite how slow the liquid was drawn out, the uniform separation between the copper and graphite particles would be disrupted from the outset. It can be deduced, therefore, that the flow of liquid out tended to cause the same local curvature changes at the liquid-gas interface that affected the interparticle capillary attraction which would in turn disrupt the original organization of particles. With the progress of further liquid evacuation, the JLM was found to lose its semi-spherical shape, imputing the action of a mechanism in which the JLM needed to maintain a constant surface particle density and surface area, which consequently forced it to adopt the shape deviation [129].

3.3.5 Conclusions

Using Talc particles to create clusters of particles of various sizes transferred to the drop, it was found that there was a positive correlation trend between particle cluster velocity and surface area coverage. This supported the model where the turning moment of the particle cluster about the centre of the drop was primarily responsible for its downward travel.

With a 10 µL deionized (DI) water drop initially dispensed above the hole on the substrate that was fully encapsulated with copper powder it was found that an additional 10 µL of DI water caused the copper particles clearly segregated to the bottom section of the drop. After a second transfer using the brush bristles close to the drop's apex, this time with graphite powder, a JLM with the copper and graphite particles clearly separated was achieved (Fig. 33C).

In summary, this section outlined the mechanics needed for JLMs with good separation between different types of particles to be created. It also presented a preparation method that is shown to do so. The method, with further development on the particle transfer aspect, is amenable for high throughput JLM production.

The findings in this section have been submitted for publication under E.S. Lin, Z. Song, H.A. Abid, J.W. Ong, O.W. Liew, T.W. Ng, Stable creation of Janus liquid marbles.

3.4 Capillary Evacuation of Liquid Marble Contents

3.4.1 Introduction

In sections 3.2 and 3.3, the brush method of creating LMs and JLMs is essentially based on a liquid drop dispensed first on a superhydrophobic substrate with a hole. The ability of liquid drops dispensed this way to be stable, had previously been demonstrated [11]. If the plate is thin enough, the drop will split into two components, above and below the hole, which are named the overhead and overhanging components respectively. The drop is rendered immobile by the solid phase's pinning action at the hole's edge (Fig. 35A) [11]. One important advantage with this LM and JLM architecture is the ability to extract the liquid contents through the hole (from the overhanging component) without disturbing the particle encapsulation.

In order to drain the liquid contents without any particle carryover, a capillary tube is inserted into the overhanging component of the drop and a method to coat just the sessile component of the drop is established (Fig. 35B). It is useful to utilise capillary tubes for liquid drainage since they don't require any external energy source, enabling the development of scientific applications based on this idea [15]. The mechanics of how this can done effectively is investigated in this section.

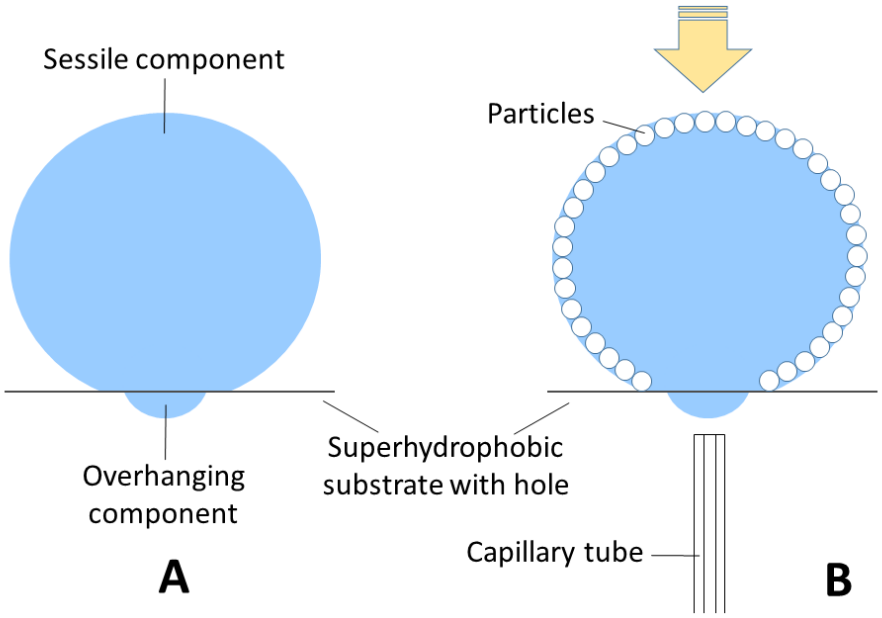

Figure 35 A liquid drop resting onto a superhydrophobic substrate with a hole creates a body with a (A) sessile and overhanging component. (B) Particles are coated from above onto the sessile component to create a LM above the hole while the overhanging component remains uncoated. Once established, a capillary tube placed in contact with the overhanging drop component would be able remove only the liquid contents of the body without particle contamination.

3.4.2 Materials and Methods

3.4.2.1 Substrate Creation

The thin superhydrophobic plate was made by first drilling 2 mm-diameter holes through copper plates that were 0.1 mm thick. The plate samples were polished until they were shiny, then ultrasonically processed for 3 minutes in ethanol (70% v/v) and acetone, followed by another 15 minutes in deionized (DI) water. The substrates were subjected to a 5-minute oxidation process in a solution comprising 2 M NaOH and 1.5 M $(NH_4)_2S_2O_8$. The phase transition from hydroxides to oxides was then completed by allowing the samples to synthesise in an oven at 180 °C for 120 minutes. The substrates were taken out of the solution following the reaction, rinsed several times in DI water and ethanol, and then dried with compressed air.

Finally, the substrates were silanized with FAS (1H,1H,2H,2H-perfluorodecyl-triethoxysilane) to produce a layer with low surface energy, excellent corrosion resistance, and thermal stability. The substrates were submerged in a FAS-ethanol solution for 30 minutes before being dried for 10 minutes at 150 degrees Celsius.

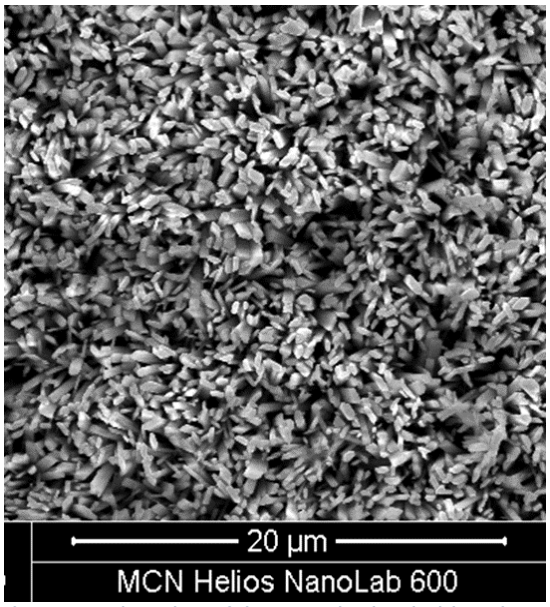

Figure 36 Scanning electron microscopy imaging of the superhydrophobic substrate created revealing prismatic nanostructures.

Using Scanning Electron Microscopy (SEM) and optical profilometry, a sample of superhydrophobic copper substrate was studied. Using conductive adhesive, the substrate was adhered to a stub and analysed using a SEM (Helios NanoLab 600). Since the samples were conductive, 10 keV could be used for imaging. Optical profilometry pictures of the SH sample were acquired by affixing the sample to a flat silicon reference surface. This was then positioned within the profilometer (Bruker Contour GT-I) and optical scans were performed. On the instrument's accompanying software, processing and analysis were executed (Contour Elite). Due to the rather broad area that needed to be mapped, numerous photos were captured, and the stitching capabilities was employed to build a map with an extended field of view.

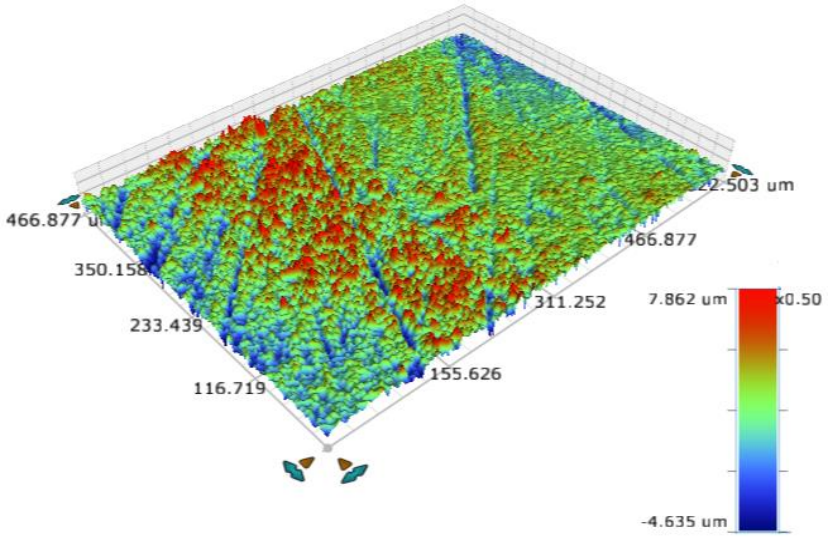

Figure 37 Optical profilometry of the superhydrophobic substrate created showing microscale structures that are random in nature.

3.4.2.2 Drop Creation

In this work, an alternative method to create the liquid marble was adopted from that described in sections 3.2 and 3.3. Commercial grade (Sigma Aldrich, 243604) hydrous magnesium silicate (Talc) of size 10 µm was used to create the LMs with deionized (DI) water as the internal core. The water was dyed with Methylene Blue to enhance visibility. The sessile and overhanging drop configuration was achieved by dispensing 20 µL volume drops over the holes on the plate. A plastic funnel was utilised to guide Talc particles to entirely cover the component of the overhead sessile drop (Fig. 38A). The excess talc particles were subsequently dispersed using compressed air at precise pressures to make a complete, clean LM.

The technique of dispensing particles onto a drop can also be used to produce LMs (Figs. 38C-D) although it results in the wastage of particles. It was discovered that removing superfluous particles with compressed air might permit clean encapsulation of the sessile component alone, but not the overhanging component of the liquid body (Figs. 38E-F). This gives further support for the previously proposed concept in which two contact lines are produced, one for the sessile component on the top surface and another for the overhanging component at the hole's margins. If this is maintained, effectively two distinct liquid-air surfaces will be produced.

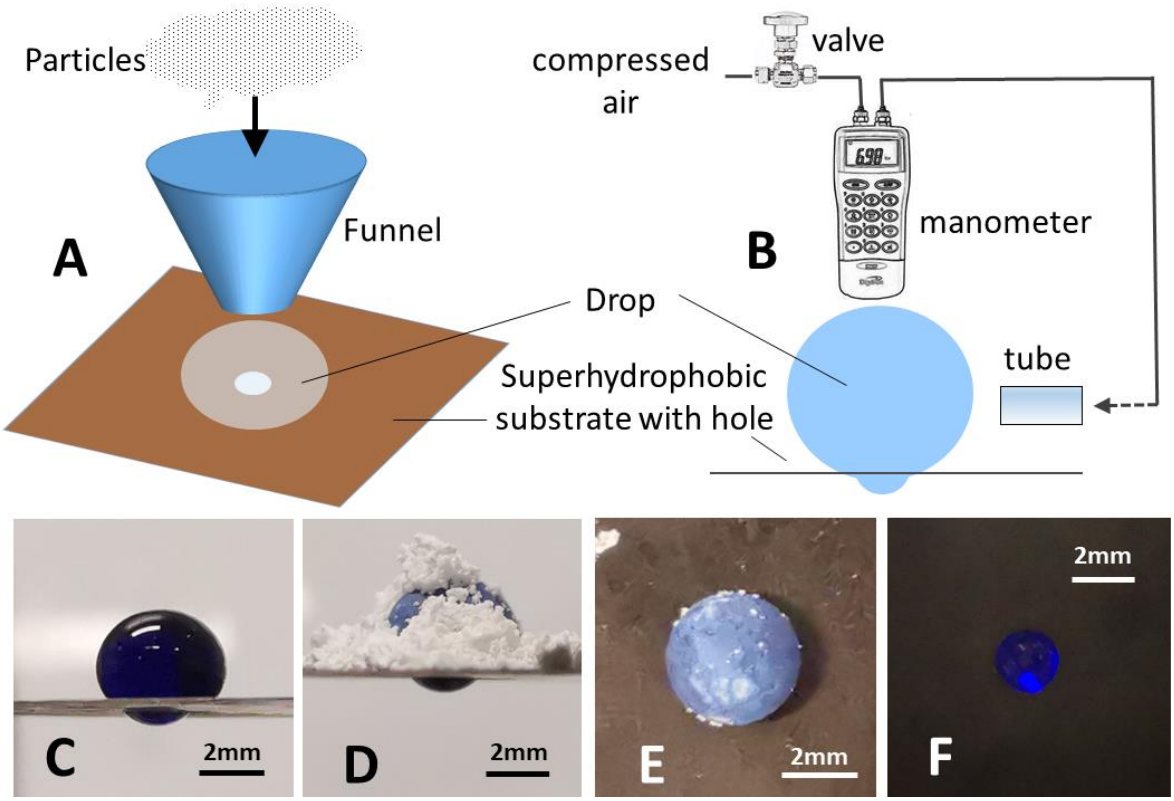

Figure 38 Process for LM creation, particles passed through a funnel (A) on to the drop. Compressed air was used to clean up excess particles, controlled by a manometer and valve (B). A side view (C) of a drop of water (coloured blue using food dye) on the SH substrate with hole where the upper sessile component is transformed into a LM (D) with excess particles. The top view of the drop (E) clearly shows the LM effect retained on the sessile component, while a bottom view (F) indicates access to a clean liquid core without particle contamination.

3.4.2.3 Liquid Extraction

Capillary tubes made of borosilicate glass with inner diameters of 0.6 mm and 1.0 mm and a length of 75 mm were held vertically with the top end slightly below the overhanging portion of the drop. The plate was manually lowered on an optical translation stage until the overhanging drop component just touches the capillary tube's bottom end. Using a high-speed camera (Fastec) and processing software, images of liquid draining from a drop were captured at 250 frames per second. The movement of the meniscus within the capillary tube was traced over time (Tracker,

version 5.05). Liquid extraction can be stopped at any time by translating the plate upwards to interrupt contact between the overhanging drop and the capillary tube, or by sealing the capillary tube's bottom end.

3.4.3 Results and Discussion

When the upper end of the capillary tube comes into contact with the overhanging portion of the liquid body (Fig. 39), liquid is observed draining from the drop. The drain rate within capillary tubes with inner diameters of 0.6 mm and 1.0 mm exhibits very linear patterns (Fig. 39) with R^2 values exceeding 0.99. The rate of liquid drainage was estimated to be 81.5 mm/s and 197.2 mm/s for capillary tubes with an inner diameter of 0.6 mm and 1.0 mm, respectively. It is well acknowledged that the velocity u of liquid flow in capillary tubes follows Darcy's law [132].

$$u = -\frac{r^2 \delta p}{8L} \tag{17}$$

where r is the inner radius of the tube, and δ_p the pressure drop across the length L. Based on this calculation, the usage of a tube with a diameter of 1.0 mm over 0.6 mm should result in a speed ratio of 2.77:1, which is comparable to the empirically determined ratio of 2.4:1. This suggests that the creation of LMs is consistent with the physics of fluid behaviour. Eventually, some particles will enter the capillary tube if the process is not terminated before the liquid is entirely drained, and 1µL of liquid must remain in the sessile drop component. As a result, the use of capillary tubes with a smaller inner diameter and a slower draining rate is preferable, as it affords greater control and minimises the issue of carry-over particles during liquid extraction.

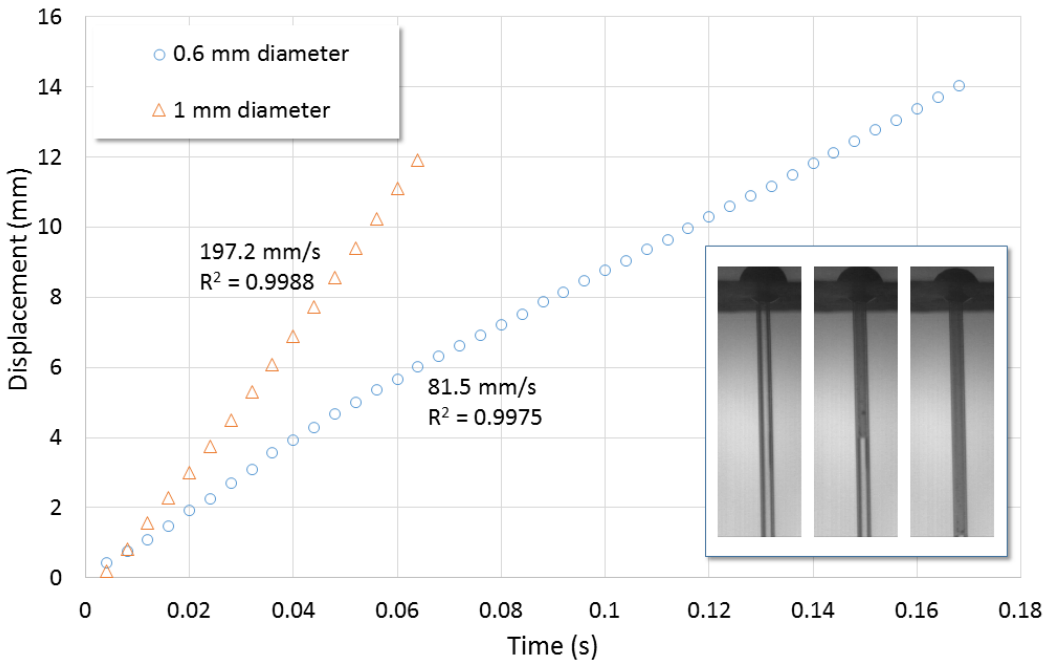

Figure 39 Plots of displacement of the liquid meniscus in capillary tubes of 0.6 mm and 1.0 mm inner diameters due to drainage from the LM body. The rates of drainage are highly linear, with a 2.4:1 speed ratio obtained with the larger diameter tube over the smaller.

3.4.4 Conclusions

On superhydrophobic surfaces, liquid bodies exhibit a sessile and overhanging component, each of which forms their own three-phase contact lines. A method of coating particles onto the sessile drop component, followed by the removal of surplus particles with compressed air, has been demonstrated to change solely the sessile component into a LM while leaving the liquid-vapor interface of the overhanging component uncoated. Since the forces associated with the application

is determined by the flowrate produced by the compressed air valve, it offers a more controllable method of LM creation without deformation compared to the method suggested in section 3.3. However the former method is advantageous with its lower powder wastage. By placing one end of a capillary tube in contact with the overhanging component, controlled drainage of liquid from the droplet could be achieved. It is determined that the rate of drainage follows Darcy's Law. Such a method makes it relatively simple to examine the contents of the LM without unintended transfer of the enclosing particles.

3.5 Particle Separation using Liquid Marbles

3.5.1 Introduction

From the investigations done in sections 3.2 and 3.3, it has been found that particle-encapsulated laden droplets in the form of a LM have non-wetting soft solid qualities. It has proven challenging to remove the covering particles from the LM in order to reach the liquid core and determine its biological and chemical state. The utilisation of optical radiation [12], ultrasonic fields [13], and timed disintegration with wettability change [14] are some of the methods that have been tried to accomplish this. However, the characteristics of the liquid, the wetting properties of the liquids and particles, the delivery of motive forces through actuators, and the design of the equipment required to provide the non-contacting fields are just a few physical factors that can affect the effectiveness of these approaches. In section 3.4, a method of evacuation using capillary tubes has been described. One of the important goals in liquid marbles is to harness them for applications.

Particle separation is a widely sought process in industry and scientific progression. The major aim for such a process is to minimise usage of solid and liquid to limit contamination in the environment. Powdered mixtures used in pharmaceutical and cosmetic formulations comprising dried particles of different wettability can be contaminated with unwanted hydrophilic material. The manufacture of talcum powder, for example, has been reported to contain heavy metal particle contaminants [133], due to its high surface to volume ratios along with the large number of Mg-O- and OH- bonds present, allowing metallic nanoparticles to attach.

Current techniques of particle separation include use of membranes [109] and coagulation-flocculation [110]. The former is subject to fouling, whereas the latter operates with the solid particles already in solution. When separation of particles in their solid state is required, exploiting the differences in wetting characteristics can be used, therefore a separation technique that achieves this would be greatly useful. This section investigates the use of LMs created in the form of pendant and sessile drops to achieve particle separation based on their differential wettability.

Particle separation of pendant and sessile drop LMs are shown in Figure 40. With the pendant droplet, liquid is dispensed from the lower distal end of a capillary tube with the assistance of a syringe placed at the top. It is then lowered onto a powder bed consisting of a mixture of nanoparticles with different hydrophobicity. Separation is achieved when the non-wetting particles coat the outside of the drop whilst the wetting particles are mixed into the liquid core. The liquid can then be drawn up from the LM using the same capillary tube to recover the wetting particles. The method used to investigate the sessile droplet is the same as chapter 3.2.

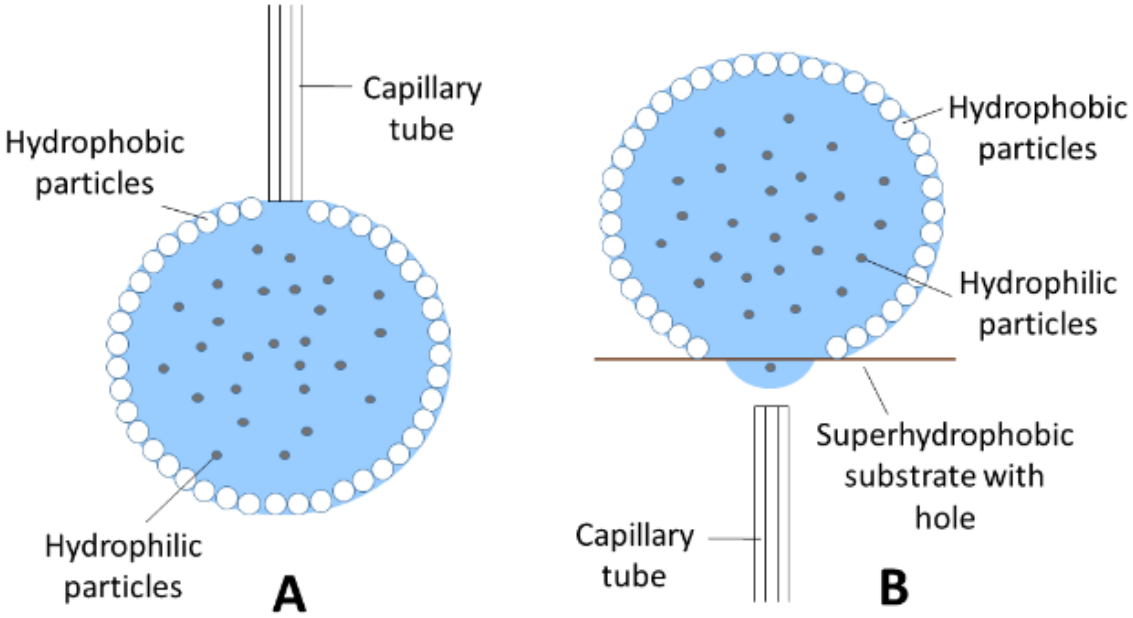

Figure 40 The schemes of separating a dry mixture of hydrophobic and hydrophilic particles via LMs formed from (A) pendant and (B) sessile drops. In both cases, the liquid core containing the hydrophilic particles are drawn out using a capillary tube. In the sessile drop approach, the dispensation of liquid onto a superhydrophobic substrate with a hole creates a liquid body with an overhanging component that is not coated by hydrophobic particles. This allows access of a capillary tube to effect drainage from the liquid core.

3.5.2 Materials and Methods

3.5.2.1 Particle Coating

Silver nanowires were created by dissolving 1 g of Polyvinylpyrrolidone (PVP, Mw ~ 55,000 Sigma-Aldrich) and 0.014 g NaCl in 20 ml ethylene glycol (EG). 0.204 g of $AgNO_3$ was dissolved in 10 mL EG. The PVP-NaCl-EG mixture was heated to 170 °C and then the $AgNO_3$-EG solution was added in to the system at a rate of 5 mL/h with constant stirring. After that, the reaction was kept at 170 °C for 1 h. When the product was cooled down to room temperature, 70 mL acetone was added into the system. The mixture was put in the ultrasonic bath for 30 min. The product was centrifuged at a speed of 7000 rpm. Then acetone was added and the washing procedure was repeated again. The nanowires were finally dried in air under 80 °C.

A mixture of graphite, acting as the superhydrophobic coating, and silver nanowires, acting as a catalyst for the reaction of the liquid is created to form a powder bed. The droplet is comprised of a solution of Methylene Blue (MB) and $NaBH_4$ which react naturally to slowly lose its colour. It is proposed that higher concentration of silver nanowires in the particle mixture would cause the reaction to occur at a faster rate.

3.5.2.2 Liquid Marble Creation

To form the external shell of the LM, graphite powder mixed with 5% (by weight) of silver nanowires were used. Drops of 20µL by volume from a solution comprising 2 mM MB and 0.1 M sodium borohydride ($NaBH_4$) was used as the internal liquid phase of the marble. Particle separation is demonstrated when the silver nanoparticles separate from the non-wetting shell and enters the liquid core where its presence catalyses an $NaBH_4$-MB redox reaction that results in a solution colour change from blue to colourless [134]. The colour was measured using a spectrometer, with the intensity of the blue wavelength reflected noticeably reducing at a faster rate with added concentration of silver nanowires.

3.5.3 Results and Discussion

Although the sessile and pendant drop approaches could be used for creating LMs, achieving uniform coating with the former is more challenging. Optimal airflow pressure enough for distributing the particles over the liquid surface but not to displace the drop is required. In some instances, a strong airflow resulted in distortion of the drop to one side of the hole, allowing the non-wetting particles to breach through and extend over the overhanging component of the sessile drop. When this occurs, complete encapsulation of both the sessile and overhanging component of the drop made extraction of the liquid core unsuccessful as the liquid core was contaminated with powder from the shell. For these reasons, the pendant drop approach for LM formation is more robust even though full encapsulation of the droplet surface was not achieved to afford maximal liquid-air interface for particle separation.

A new method to coat a pendant drop was investigated. The droplet was positioned over a tilt/rotary stage covered with a thin layer of particles (Fig. 41A). The stage is tilted to a fixed angle and lifted towards the drop on a vertical translator. When the particles reach the drop, the stage was rotated around the central axis of the drop, covering the outside in a thin layer of powder. It is observed that the height h1 to which the particles are able to coat the drop relative to its height h0 is dependent on θ up to 15^{o} (see Figs. 41B – C). At higher θ angles (e.g. 30^{o}), the hydrophobic particles tended to coat unevenly (see Fig. 41D).

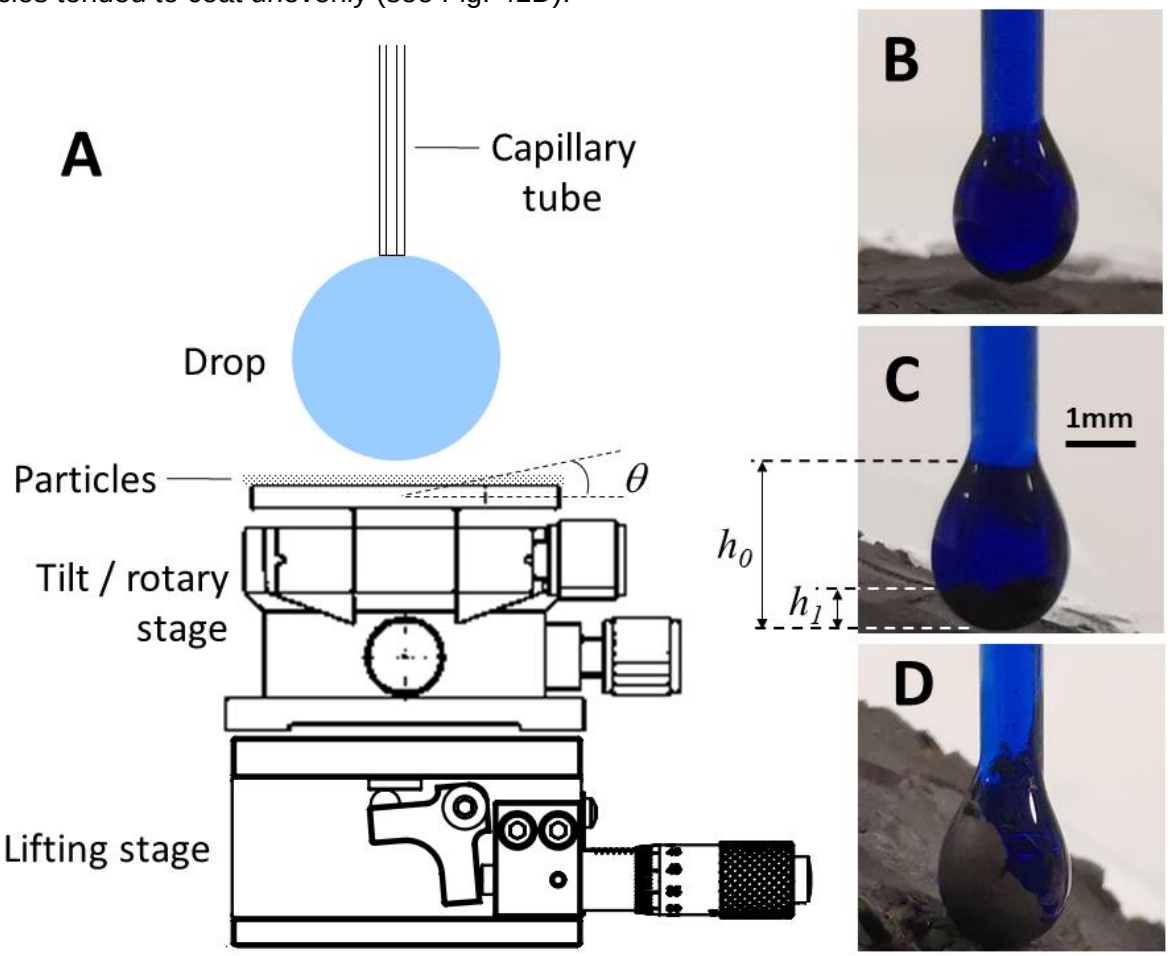

Figure 41 Generation of a LM from a pendant drop held in place by a capillary tube. A rotary stage with hydrophobic particles is placed on top a lifting stage (A). The surface is tilted to an angle of θ, raised to contact the drop, and then rotated to coat the particles on the drop. Varied coating heights h1 in relation to the height of the drop h0 were achieved with platform tilt angles of (B) 5o and (C) 15o. At a platform tilt angle of (D) 30o the coverage tended to be skewed to one side.

It is important to note at this stage that the inability to fully encapsulate the pendant drop with the non-wetting particles does not hinder the utility of this approach. When the stage platform was in a horizontal position, the area of contact between the powder mixture and pendant drop is minimal. At a tilt angle of up to 15^{o}, the coverage of particles over the bottom surface of the droplet was

uniform, thus allowing a quantifiable coverage metric of h1/h0 to be used (Fig. 41C). Figure 42 presents box plots of measurements made at 5^{o} and 15^{o} using graphite and Talcum powder to form the shell. At platform tilt of 15^{o}, an average coverage metric of 0.25 was attained. The advantage of such a low coverage metric is that chance of excess talcum or graphite powder into the capillary tube during the liquid evacuation process is greatly reduced.

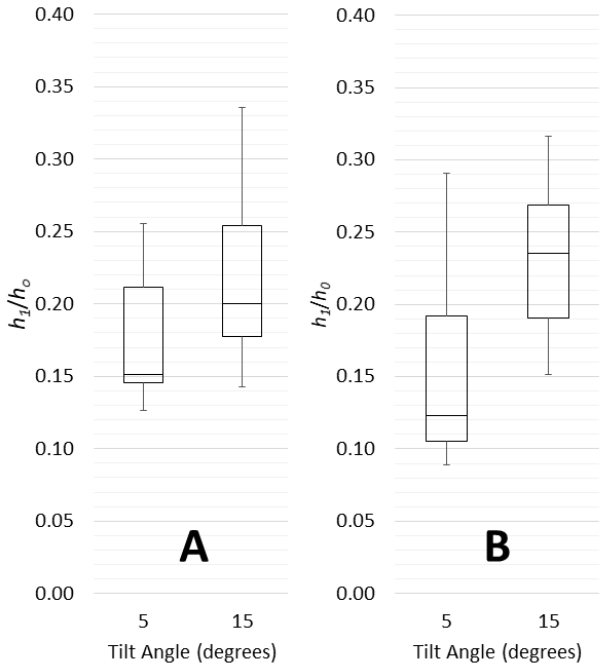

Figure 42 Box plots based off 8 readings of h1/h0 (a metric for LM coverage using the pendant drop approach) determined at platform tilt angles of 5o and 15o for LMs formed from (A) graphite and (B) Talcum powder as the hydrophobic shell component.

The ability of silver nanowires to act as a catalyst in the degradation of 1 mL of the solution of MB and sodium borohydride (diluted by 10-fold) placed in a cuvette is illustrated by colour change. In a LM, the colour changes of the liquid core due to the redox reaction is difficult to distinguish when the outer shell is opaque. To demonstrate separation of silver nanoparticles from the shell into the liquid core, the liquid was drawn out from the pendant drop using the capillary tube and diluted 100 times with distilled water for analysis. As test controls, liquid extracted from the pendant drop without particle coverage (Fig. 43A) or coated with graphite powder alone (Fig. 43B) displayed clear blue tints indicating presence of MB. In contrast, liquid drawn out from the pendant drops coated with graphite and silver nanowire powder is colourless, showing catalytic reduction of MB by silver nanowires separated into the liquid core.

In contrast, the liquid extracted from the pendant drops covered with graphite and silver nanowire powder is colourless, indicating that silver nanowires detached from the liquid core catalysed the reduction of MB. Since the liquid core is withdrawn as soon as the coated pendant drop is created, this suggests that the wettability particle separation mechanism occurs very quickly when the liquid droplet hits the powder mixture. Notably, emptying the liquid core into the capillary tube at flowrates 0.05 mL/s minimises carryover of talc or graphite particles into the capillary tube in the majority of cases. At the end of the liquid drawing process, when the likelihood of talc or graphite entering the tube is greatest, greater care must be taken. Utilizing an absolute displacement syringe device is useful in this situation [135].

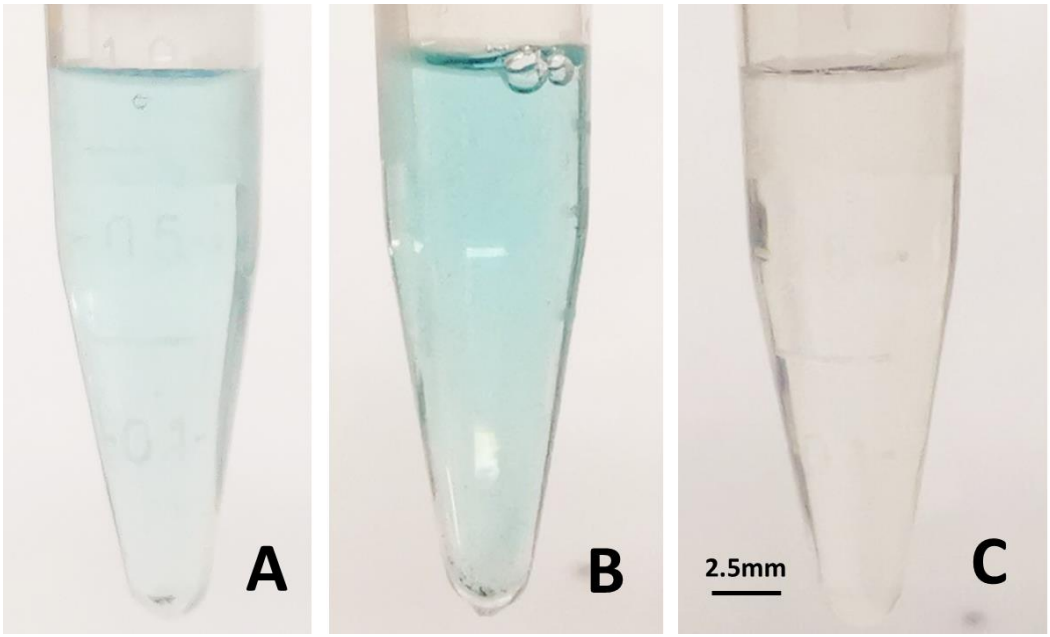

Figure 43 Images of liquid extracted from pendant drops of MB-NaBH4 solution using capillary tubes followed by 100 times dilution with distilled water. In the absence of any LM created, the extracted solution (A) retains the distinctive blue colour of oxidized MB. The blue colour of oxidized MB is also observed from liquid extracted (B) from LMs coated only with graphite powder. Liquid extracted from LMs (C) coated with graphite and silver nanowire powder mixture is colourless due to reduction of MB by silver nanowire particles separating into the liquid core from the hydrophobic shell.

The absorbance spectrum (Fig. 44-45) of the MB-$NaOH_4$ solution was measured using a spectrometer. The log of the initial light intensity divided by the measured intensity is used to determine the range of absorbance wavelengths. The spectrums were noted to peak at a range between 600-680nm, which correlates with the blue absorbance wavelength of 600-640nm [136]. Figure 45 shows the zoom in of the plots at the 600-640nm wavelength, with the different colours indicating duration of reaction. This clearly indicate a decrease in intensity as the reaction progresses, showing the loss of colour after 1 minute.

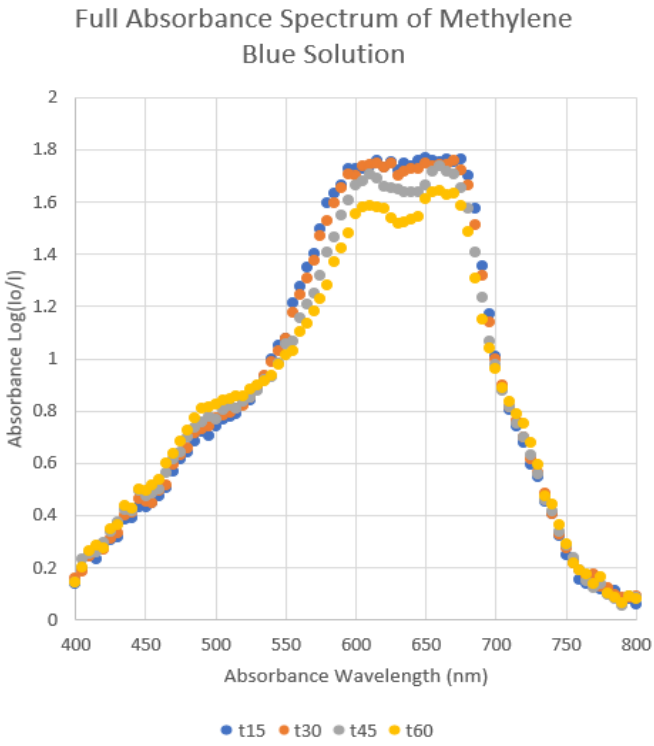

Figure 44 Plot of Absorbance (Log of initial light intensity divided by measured intensity) over the full wavelength spectrum over 60 seconds. Note that the spectrum peaks at the wavelength range between 600-680nm, which correlates with the blue absorbance wavelength range of 600-640nm

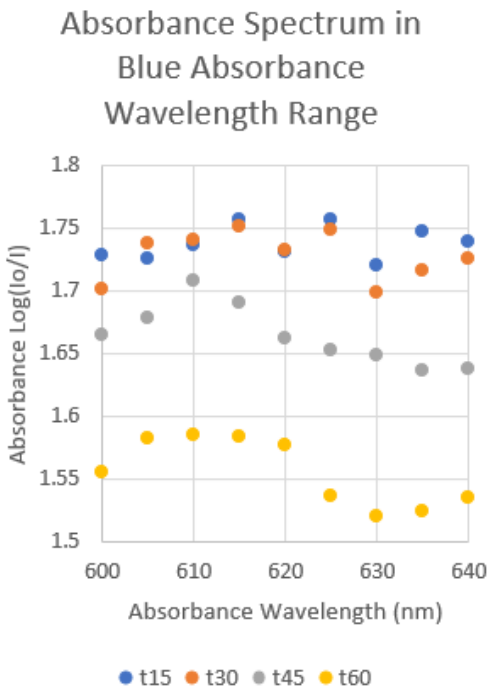

Figure 45 Zoom in on the range of absorbance for the wavelength of blue light, indicating a clear loss of absorbance over time.

Although both the sessile and pendant drop methods can be employed to create liquid marbles, it is more difficult to achieve uniform coating with the former. This requires appropriate airflow pressure sufficient for dispersing particles throughout the surface of the liquid, but not so high as to dislodge the drop. In certain circumstances, the high flow speeds caused the drop to be distorted to one side of the SH hole, allowing non-wetting particles to breach the hole's neck and extend over the overhanging portion of the sessile drop. When this occurs, full encapsulation of the sessile and overhanging components of the droplet makes it difficult to extricate the liquid core.

In addition, the capacity of the sessile drop to remain in place over the hole is predominantly dictated by three-phase contact line pinning on superhydrophobic surfaces [20, 21]. Due to these factors, the pendant drop method for liquid marble creation is more robust, despite the fact that complete encapsulation of the droplet surface was not achieved in order to provide the greatest liquid-air interface for particle separation.

The non-wetting particles accumulated at the ends of capillary tubes with the pendant drop approach after liquid evacuation (Fig. 46A), allows for merging and collection. This differs from the case where vials are used in which particles would typically attach to wall surfaces after liquid evacuation (see Fig. 46D). The entire process may be automated rapidly with the proper automation incorporated.

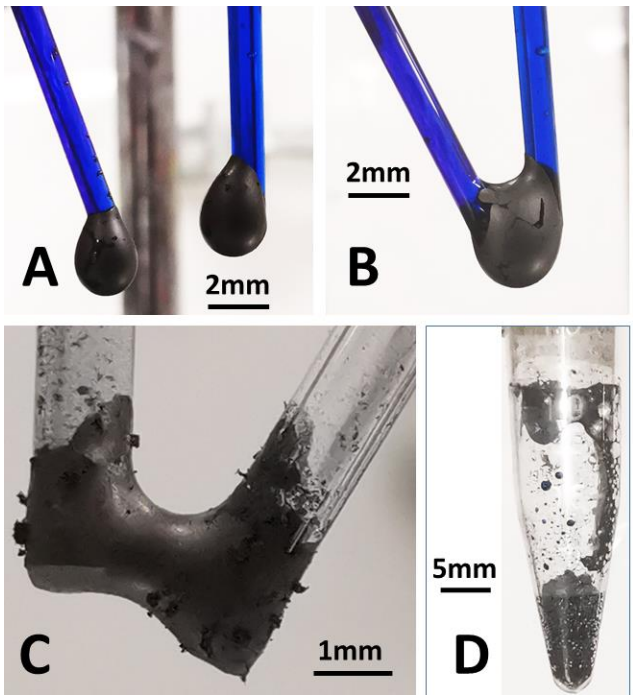

Figure 46 When liquid is drawn out of the pendant LM, the volume of the liquid core is reduced to create a smaller drop (A) at the distal end of the capillary tube covered by a thicker external shell of graphite. Two small pendant marbles can be brought into contact and merged (B) to facilitate further harvesting of the shell particles in the anhydrous state from a point source (C). When liquid is drained out of a typical receptacle (D), there is inevitable particle attachment to the wall that hampers harvesting.

It is important to note that powdered mixtures utilised in pharmaceutical and cosmetic formulations and consisting of dried particles of varying wettability might become contaminated with undesirable hydrophilic material. It has been reported that talcum powder production contains heavy metal particle contamination [137]. The presence of a large number of Mg-O- bonds and OH– bonds, together with the talc powder's high surface-to-volume ratio, enables metallic nanoparticles to adhere. Human health effects of prolonged exposure to these powders contaminated with heavy metals are still under investigation. However, there is a high possibility that findings comparable to asbestos-contaminated talcum powder will be discovered [138].

At this point, it is essential to emphasise that the LM approach does not give a means to differentiate hydrophilic (those with contact angles <90 degrees) and hydrophobic (contact angles >90 degrees) particles. Despite their low surface energies, graphite particles have contact angles below 90 degrees and can nonetheless form the shell of liquid marbles [139, 140]. The ability of graphite to do so augurs well for its utility in separating graphene oxide (GO), which readily dissolves in water due to hydrogen bonding processes [141], when synthesised by dry processing [142]. GO is a material with features that make it applicable to novel applications [143, 144].

3.5.4 Conclusions

The ability to separate wetting and non-wetting particles from an initially dry mixture is achieved by LM formation using pendant drop and sessile drop approaches. The method permitted the wetting particles to be separated into the liquid core which is then easily withdrawn into capillary tubes for analysis without any need for actuator motive forces or careful design of specialized equipment. There is overall greater robustness in using the pendant drop over the sessile drop over a superhydrophobic hole with the approach described here.

A straightforward method for isolating undesirable wetting components from non-wetting powders for contamination analysis has obvious practical implications. The downside of this technique is that liquid marbles cannot be transported. This is typically not an issue, as the fragile nature of most liquid marbles makes them difficult to manipulate. It should also be noted that this method is not limited to the wetting and non-wetting materials utilised in this study.

The findings in this section have been published in E.S. Lin, D.C.K. Chung, J.W. Ong, H.A. Abid, L. Peng, X. Jiang, O.W. Liew, T.W. Ng, Liquid marble particle wetting separation. Colloids and Interface Science Communications. 35 (2020) 100237.

3.6 Chapter Summary

This chapter described the investigations conducted to advance the creation, liquid content removal and applications using liquid marbles in this project.

In section 3.2, a new approach to create LMs with better control and reduced wastage was reported. It was based on using cosmetic brushes to transfer particles from the bed to the bristle, then from the bristle to the liquid-gas interface of the droplet. The method was analysed theoretically and the basis proven through experiments. It was found that both LMs and JLMs could be successfully created using this new 'brush-on' technique.

In section 3.3, studies using clusters of particles of various sizes that were transferred to the drop uncovered that there was a positive correlation trend between particle cluster velocity and surface area coverage. This supported the model where the turning moment of the particle cluster about the centre of the drop was primarily responsible for the downward travel. It was then found that if the mechanics needed were satisfied, it was possible for JLMs having good separation between different types of particles to be created.

A straightforward method for isolating undesirable wetting components from non-wetting powders for contamination analysis has obvious practical implications. Powdered mixture production such as talcum powder utilised in pharmaceutical and cosmetic formulations has been found to contain heavy metal particle contamination [137]. In section 3.5, an ability to separate wetting and non-wetting particles from an initially dry mixture was achieved by LM formation using both the pendant drop and sessile drop approaches. The method permitted the wetting particles to be separated into the liquid core which can then be easily withdrawn into capillary tubes (section 3.4) for analysis without any need for actuator motive forces or the careful design of specialized equipment. This method could alleviate the contamination of heavy metal particles in the production of talcum powder [133].

4. Gas Bubbles in Liquid Marbles

4.1 Preamble

The role of gases in liquids has been widely studied in the literature. The existence of two phases (liquid and gas) together provides an avenue for interesting mechanics to be uncovered which can potentially lead to important applications being developed, such as the presence of hydrogen in aerobic bacteria to support its respiration and carbon fixation [145]. This chapter details efforts to investigate the use of gas bubbles in liquid marbles. A study is first made on the generation of gas bubbles in liquids using a syringe-based fluid dispensation system in section 4.2. In the absence of feedback, estimation techniques to improve fluid delivery precision have limited efficacy [146]. A linear servo-based actuator system was described to provide absolute indications of plunger position.

Subsequently, the ability to measure the flowrates of slowly released gas bubbles using an inverted burette technique was described in section 4.3. Average production rates and total production volumes throughout specified time periods are the two main parameters in gas sensing analysis. Flowrate sensors measure the former parameter in order to derive the latter. Depending on the method used [16-18], the devices and structures needed to achieve this can be expensive and complicated. A direct way of measurement involves sending the gas to an airtight syringe, where the extent of plunger movement over time enables the determination of both parameters [147].

Diverse natural [148] and artificial [149] processes generate modest amounts of gases at velocities slower than 1 mL/s. In such situations, measurements done with conventional flowrate sensors and sealed syringes are fraught with significant levels of uncertainty. To facilitate the measurement of the volume and rate (1 mL/s) of slowly formed gas bubbles, the approach of utilising an inverted burette with camera imaging is examined, showing an accurate determination of the flowrate of introduced bubbles at low speeds.

In section 4.4, a gas bubble method that was found to clear the apex of the LM shell was investigated. It has been proven difficult to add additional reagents into the LM without contamination or deformation. A solution is provided to this via the generation of a singular air bubble within an LM that is deposited on a superhydrophobic substrate with a hole [19-21]. The suspended air bubble causes localised displacements of the outer shell particles, forming open regions at the apex of the LM. Clearly, this allows additional reagents to be added to the LM prior to bubble rupture and shell reformation.

Finally, section 4.5 outlines an application of gas bubbles in LM through the generation of oxygen or hydrogen gas via electrolysis. Electrolysis of water has been used to generate gas bubble streams however, it currently cannot be used to improve the aeration of the internal contents of a LM without disrupting the chemistry in the medium.

This section proposes a method of overhead aeration through the generation of gas by electrolysis, ensuring that the composition in the overhead component is minimally affected in the process. The single gas bubble was able to reside stably within a LM, resulting in the clearance of particles at the shell's apex, causing the transient opening of the particle shell. This ultimately allows for addition of reagents with concomitant bubble rupture followed by full particle reformation, creating a simplified novel approach of exploiting LMs. This technique of on-demand aeration of LMs promotes applications of LMs as microbioreactors. An array of LMs may be created resulting in an upward scaling manner.

4.2 Precision Syringe-based Fluid Dispensation

4.2.1 Introduction

In this section, a linear servo-based actuator system was described to provide absolute indications of plunger position. Infusion pumps are used to provide controlled amounts of hydration/electrolyte fluids, medicine, or nutrition into a patient's circulatory system. Peristaltic pumps feature quick response times, permit pressure control with a flow metre, and can manage fluid volumes up to a few litres. However, syringe pumps are more resistant to backflows, generate fewer hemolytic effects in red blood cell transfusion therapies [150, 151], provide superior volume control in the administration of patient-controlled analgesics [152, 153] and anaesthetics [154, 155].

Due to the ease of use of syringe pumps, new attempts have been made to make them more accessible for general applications through inexpensive manufacturing [156], open source software to control the movement of the syringe piston [157], and electricity-free variants [158]. In healthcare settings, however, the proper operation of syringe infusion pumps is of utmost importance [159]. It should be mentioned that stepper motors are utilised by the great majority of syringe pumps. In the absence of feedback, estimation techniques to improve fluid delivery precision have limited efficacy [146]. Due to the expense of integrating encoders, an alternative is to install a pressure measuring device at the syringe's output [160]. While this may be useful for regulating flow under changing pressure conditions, such as when a patient turns in bed or moves his or her arms, it does not provide indications of excess or under delivery of the prescribed solution.

4.2.2 Experimental Setup

A servo-based actuator system equipped with a potentiometer sensor to offer absolute indications of plunger position that are unaffected by electrical signal interruptions were investigated. Its performance was confirmed using a camera-tracking system. Also explored were the properties associated with varied syringe capacities, plunger movement speeds, and liquids of varying viscosities.

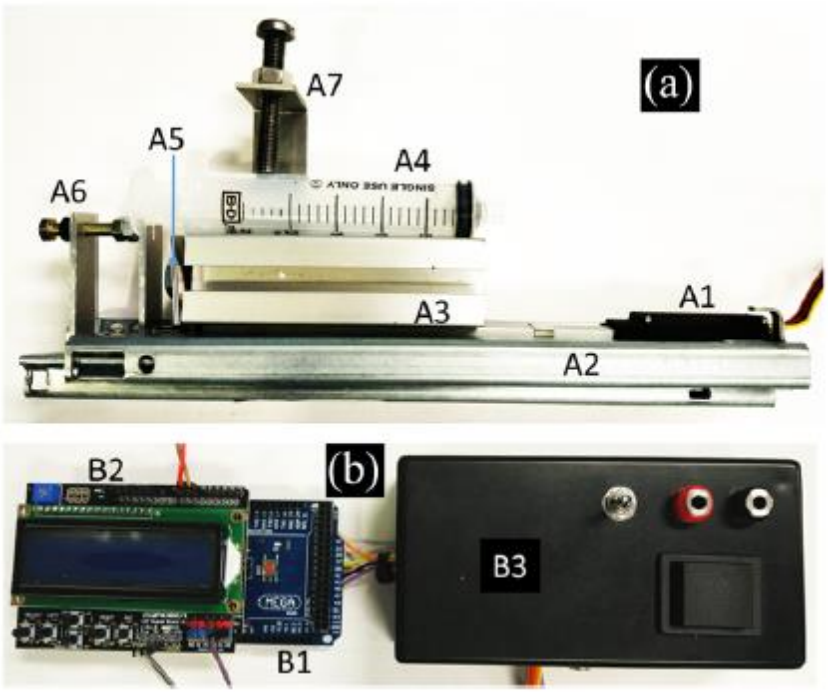

Figure 47 a) Hardware section of the system which includes linear servo actuator (A1), drawer slider (A2), aluminium extrusion (A3), syringe (A4), adapter to locate syringe (A5), adaptor to move plunger (A6) and backing platform (A7) which attaches to the drawer slider, holding the linear servo actuator and the clevis at the stationary end. B) electronic interface comprising of Duinotech MEGA 2560 R3 microprocessor (B1), LCD and keypad shield (B2) and power supply box (B3) [135]

The designed system is comprised of well-fitting components [see Fig. 47(a) (Multimedia view)]. A linear servo actuator with a stroke length of 140 mm and a maximum translation rate of 6.8 mm/s when powered by a 12 V direct current had a stroke length of 140 mm (DC). It is equipped with a potentiometer corresponding rated voltage (based on a 5 V supply) aids to show the actuator's position. The actuator is placed into a cheap drawer slider to assure linear motion. Parallel to the linear servo actuator is a commonly accessible and standard aluminium extrusion piece with adapters for mounting a syringe. The syringe's plunger is moved via an adapter that connects it to the linear servo actuator's moving head. A backing platform that attaches to the drawer slider contains a pin that fits into the clevis at the end of the linear servo actuator that remains stationary. A screw-down stabiliser on the platform holds the syringe firmly in place throughout plunger movement. Using laser machining, the backing platform and adapters were manufactured from aluminium (Coherent, MTA10).

4.2.3 Experimental Method

The performance of syringe pumps was measured by observing the linearity of plunger movement using pure water. The numbered and calibrated speed settings ranged from 1 to 6.6 m/s. A basic setup was created in which a smartphone camera (Nokia Lumia 1020) was used to record 720p at 30 frames per second image sequences (fps). The image sequences were then processed with open-source video tracking software to establish the position of the plunger (Tracker, ComPADRE). The linearity performance of the syringe pump was determined by testing two considerably different syringe sizes (5 mL and 50 mL) with the pump operating at a speed setting of 5. Next, the linearity of the syringe pump's performance was determined by conducting tests at two drastically varied speed settings (1 and 10) while maintaining a constant syringe size (20 ml). For evaluating repeatability, four syringe sizes (3 mL, 5 mL, 20 mL, and 50 mL) were utilised, and the speed setting for each was held constant at 1, 5, and 10, respectively, for a total of 10 repetitions. During infusion, the syringe pump was turned off for interruption testing. After power was restored, the continuation of syringe pump operation from its previous state was monitored. This test was carried out ten times. For medium viscosity effect testing, the linearity performance of the syringe pump with water was tested with greater viscosity fluids, a 50% glycerol-water mixture and Freund's adjuvant (Sigma, F5506-10ML). The former was made by adding glycerol (Sigma, G9012-1L) to water and mixing with a vortex mixer until homogeneous. After 1 hour of settling to eliminate bubbles, the combination was utilised. Using a constant syringe size (3 mL) and two speed settings, the test was conducted (1 and 10).

4.2.4 Results and Discussion

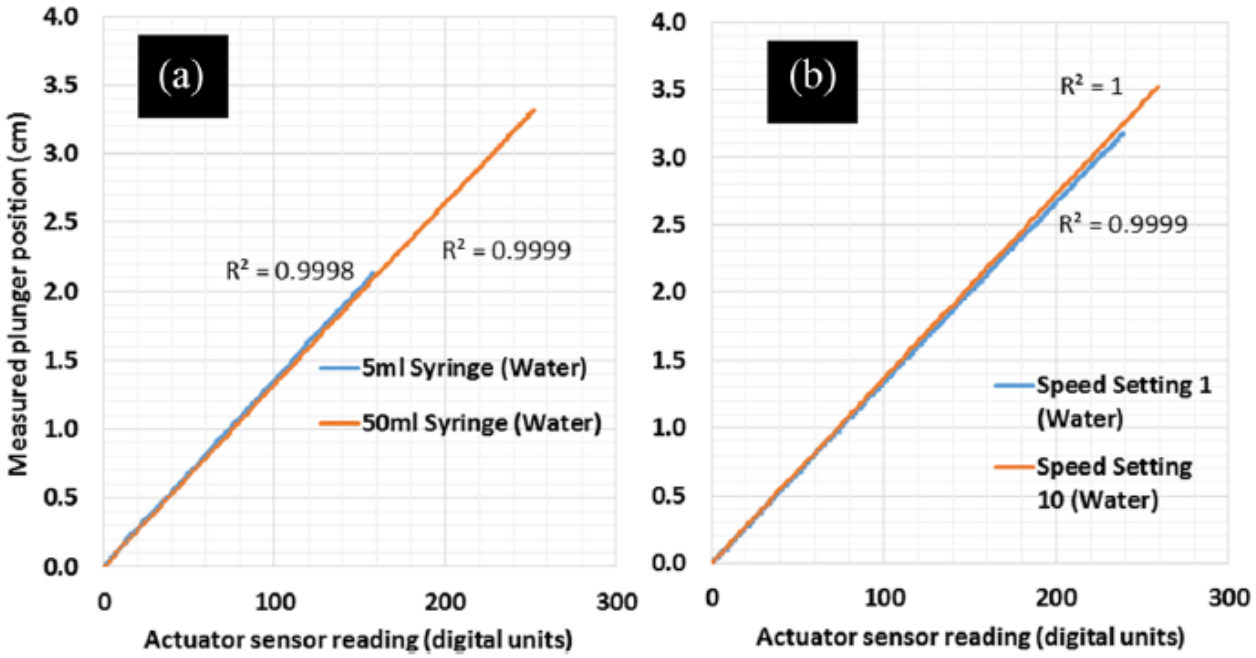

Figure 48 Linearity test using a constant speed setting (a) with varying syringe sizes and constant syringe size (b) with varying speed settings [135]

Under situations of various syringe capacities or speed settings, the measured displacement of the plunger (using image tracking) corresponded extremely well with the readings from the sensor on the linear servo actuator (digitised to 1024 level values) [Figs. 48(a) and 48(b)]. The product moment correlation coefficient (R^2) for the trends is greater than 0.9988, indicating a high degree of linearity. Each digital level corresponds to a displacement of 0.16 mm, which is just one order of magnitude less accurate than the conventional digital Vernier scale.

During an infusion, it is crucial that this linearity does not deviate. The results of the repeatability tests undertaken are displayed in Figure 49(a), demonstrating extremely high levels of repeatability. Over ten simulations of power failures demonstrated the system's capacity to display the same digital level value when power was turned off and when it was restored [see Fig. 47]. Without the capacity to establish the absolute position of the syringe plunger in order to resume interrupted operations, stepper motor systems will require the incorporation of a battery-based power supply component. This has inherent drawbacks because it requires the incorporation of additional circuitry. In addition, battery usage necessitates monitoring of shelf life and has an impact on the environment when batteries are disposed [161, 162].

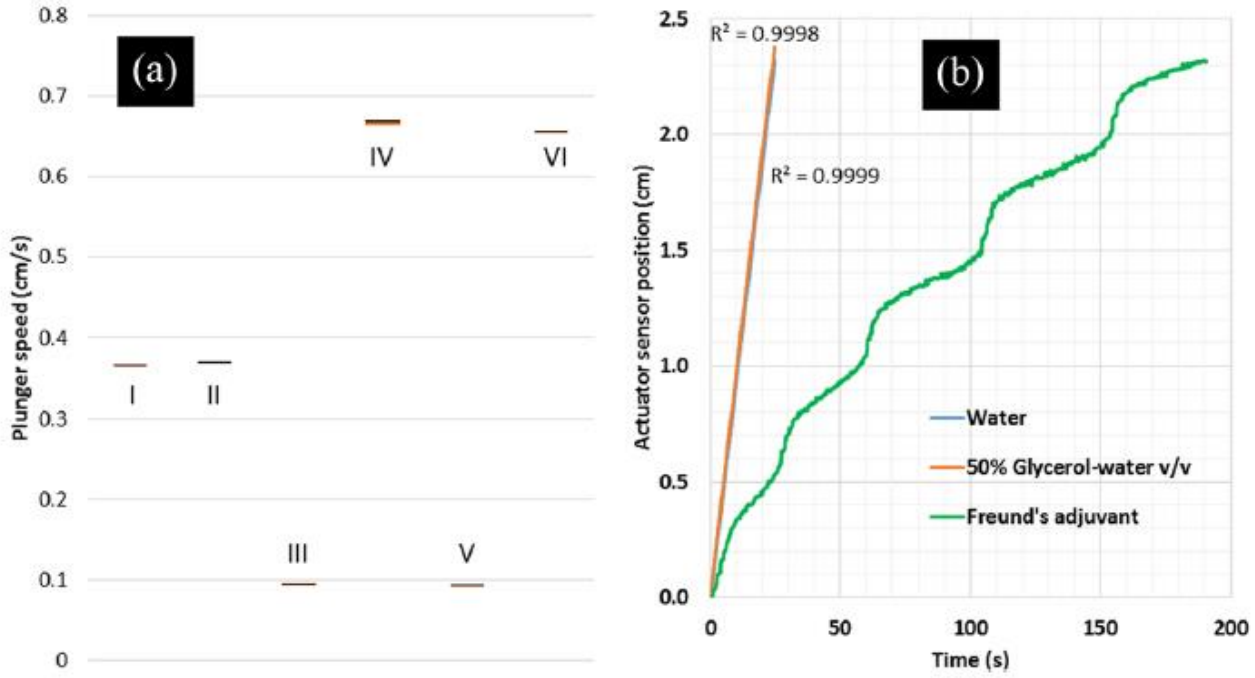

Figure 49 Box plot of (a) slope values obtained with varying syringe size (mL) and speed setting (1-10) combinations of I) 5,5 II) 50,5 III) 20,1 IV) 20,10 V) 20,10 and VI) 3,10 respectively based on the average of 10 runs. Plots of (b) the tracked position of the syringe plunger over time at speed settings 1 and 3 mL with different liquids inside the syringe of water, 50% glycerol-water (v/v) and Freund's adjuvant respectively. [135]

In addition, the system's ability to handle the transport of viscous fluids was investigated. It is well known that viscosity affects the performance of infusion pumps [163-165]. In addition to its extensive use in biochemical applications, glycerol/water solutions offer an easy way to modify the viscosity of the aqueous phase [166-168]. Adjuvants, such as Freund's, are commonly used to augment animal and human immune responses to specific antigens in the host species [169, 170].

The data shown in Figure 49(b) demonstrated that the linear trends of 50% glycerol-water (R^2 = 0.998) were nearly identical to those of water. This was the case despite the fact that the viscosity of 50% glycerol-water (6.80 mNs/m2) was 7.6 times that of water (0.89 mNs/m2) and was unaffected by the speed setting (1–10). With Freund's adjuvant, which has a viscosity approximately 36 times that of water, the situation is different, and a nearly cyclic stick slide behaviour is observed at speed setting 1. This behaviour is not unexpected given that the adjuvant consists of three-dimensional microdroplets of antigen spread in a continuous paraffin oil phase []. The ability to inject the reagent at steady flowrates at low plunger speeds can be hindered by stick-slip behaviours. The system's utility resides in its capacity to detect such features, providing users with quantitative values to better explain these nonuniformities and, if needed, implement corrective steps. We anticipate that the technique will also be used to evaluate the quality of syringes [171]. Recently, instances of substandard syringes resulting in needlestick injuries have been documented [172].

4.2.5 Conclusions

A vast majority of syringe pumps operate on stepper motors, which limits their effectiveness for precision fluid delivery using estimation algorithms. Such a system also hampers the ability to ascertain if the infusion or aspiration instruction has been correctly carried out in the event of power interruptions. In this work, a linear servo-based actuator system was described to provide absolute indications of plunger position. System performance in terms of linearity and reliability of plunger translation were verified using a camera tracking system with syringe capacities ranging from 3 to 50 mL and at syringe plunger speeds ranging from 1 to 6.6 mm/s when distilled water was used as the medium. In investigations involving more viscous liquids, the system revealed

similarly linear characteristics with 50% glycerol-water (v/v) but cyclical stick-slip behaviour with Freund's adjuvant.

While the syringe pump system here was shown to provide a precise method of generating liquids, there is a possibility for it to deliver air as well. In particular, it may be used to generate bubbles with specified volumes. Naturally, tests of varying speed settings and syringe sizes will need to be conducted to show the repeatability and precision of such an approach. If found possible, this technique will open up new avenues of research in applications where precise aeration is required [127].

The findings in this section have been published in J.W. Ong, D.C.K. Chung, E.S. Lin, H.A. Abid, O.W. Liew, T.W. Ng, Syringe infusion pump with absolute piston displacement control. Review of Scientific Instruments 90 (2019) 076108.

4.3 Slow Bubble Release and Measurement

4.3.1 Introduction

In section 4.2, a precise method of syringe pump actuation was achieved, allowing for accurate injection of air bubbles of specific volume and flow rates. This section explores the measurement of these flowrates using an inverted burette and camera setup.

In fields such as agriculture [173], environmental monitoring [174], food production [175], fuel production [176], and materials processing [177, 178], the compositional characterisation and volume measurement of gases emitted from liquids are crucial. The biological entities present inside these aerosolized gas samples can be detected utilising techniques such as DNA profiling [179].

In addition to compositional elucidation, two more parameters that are essential for gas sample analysis are their average production rates and total production volumes throughout specified time periods. Flowrate sensors measure the former parameter in order to derive the latter. Depending on the mensuration principle employed [16-18], the devices and structures needed to accomplish this can be expensive and complicated. A more direct way of measurement involves sending the gas to an airtight syringe, where the extent of plunger movement over time enables the determination of both parameters [147].

Diverse natural [148] and artificial [149] processes generate modest amounts of gases at velocities slower than 1 mL/s. In such situations, measurements done with conventional flowrate sensors and sealed syringes are fraught with significant levels of uncertainty. Priestley [180] originally described the process of collecting bubbles over an inverted jar in the eighteenth century [174, 177, 178, 181, 182]. This is because gas bubbles that rise to the top liquid surface only experience minimal resistance at the gas-liquid interface, where they mix and aggregate in the head space of the jar. Nonetheless, it is vital to ensure that these bubbles do not collide with and adhere to highly hydrophobic surfaces as they ascend inside the liquid, since this would impact volume and rate measurements [183, 184].

Difficulties in establishing the height of the gas column within the jar compromise the accuracy of gas volume and production rate measurements made using the inverted jar method. In addition, the inaccessibility of the head area makes it difficult to collect the gas stored there for compositional study.

The use of an inverted burette configuration that enabled volume and time-course tracking of bubble movement using camera imaging is demonstrated to be an improvement over the traditional inverted jar (or beaker) method for detecting gases created in small volumes and at low rates (below 1 mL/s). Comparing discrete gas volume measurements produced at 0.57 mL/s with pre-set air volume delivered by a syringe pump revealed remarkable correspondence, linearity, and repeatability.

4.3.2 Experimental Method

Using a jar with a large cross-sectional area (e.g., 40 mm diameter for a conventional 50 mL beaker) to collect gas samples will not result in accurate volume measurements based on the height of the column. However, the use of a narrow cylinder with a tiny cross-section will prevent the gas sample from easily passing through the liquid column and into the collection headspace. In the apparatus designed (see Fig. 50), a typical 50-mL capacity burette (Haines, LW150701) with a 13 mm inner diameter meets the requirements for sensitive volume measurements and easy bubble passage. The burette is inverted with the stopcock pointing upwards, and an adaptor with two tubes with Luer connector ends is attached to the open end of the inverted burette using silicone (to prevent water leakage). One tube delivers gas, while the other is connected to the base of a water-filled reservoir. To fill the burette with water, one must first open the stopcock and plug

the gas inlet end of the Luer connector. This ensures that any liquid that fills the burette cannot escape through this opening.

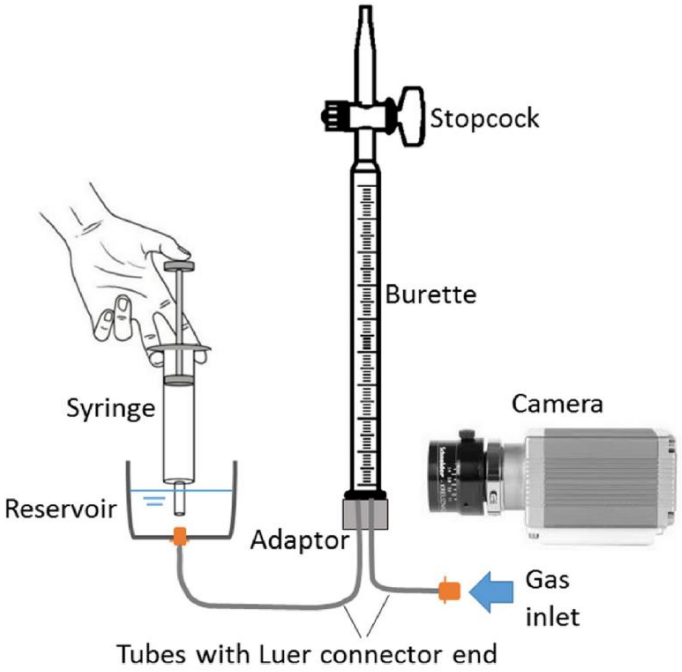

Figure 50 Experimental setup that allows for volumetric and rate measurements of slowly generated bubbles [185]

Using a syringe, water is drawn from the reservoir and injected into the Luer connector at the reservoir's base. When the required water level is reached in the burette, the stopcock is closed to maintain the position of the meniscus. The introduction of gas to an unplugged Luer connector during an experiment causes the formation of buoyant bubbles at the bottom of the burette. The passage of these bubbles is captured by a high speed (Fastec Troubleshooter) and low resolution (Hitachi SX14Q004) camera, with spatial resolutions of 640 x 480 and 320 x 240 pixels, and recording rates of 500 fps and 30 fps, respectively. The volume of gas delivered is calculated by the difference between the initial and final positions of the liquid meniscus as measured on the burette's graduation scale. This was accomplished with a regular camera (Moticam 3) with a resolution of 2048 by 1536 pixels and 12 frames per second (fps). To allow greater visibility of the meniscus, food colouring might be added to the liquid.

4.3.3 Results and Discussion

To validate the operating functionality of the system, a precise source of air delivery is required. This was achieved with the use of a syringe infusion pump with absolute piston displacement control as discussed in chapter 4.2 [135]. In this system, a 10-bit analog-to-digital converter with a maximum error of 3 bits was utilised. This resulted in a 0.41 mm positional inaccuracy. Due to the 15.78 mm diameter of the syringe, the volumetric inaccuracy is restricted to 0.08 mL. In the initial round of testing, the syringe infusion pump was configured to deliver discrete quantities of air to the upside-down burette. The collected air volume was then measured using the graded markings on the burette (on the burette).

In order to assess correspondence, linearity, and repeatability, measurements (of the syringe pump and inverted burette) were repeated ten times for each volume of air delivered. In the second series of testing, the syringe infusion pump was programmed to supply continuous amounts of air to the inverted burette at flowrates of 0.20, 0.32, and 0.57 mL/min. The camera was used to count the number of bubbles that passed across a specific horizontal plane of the burette. Using the video sequences at each flowrate, the number of these bubbles was then measured in relation to the volume of air given and the duration of the procedure from beginning to conclusion. To verify repeatability, each volume and time setting was carried out ten times.

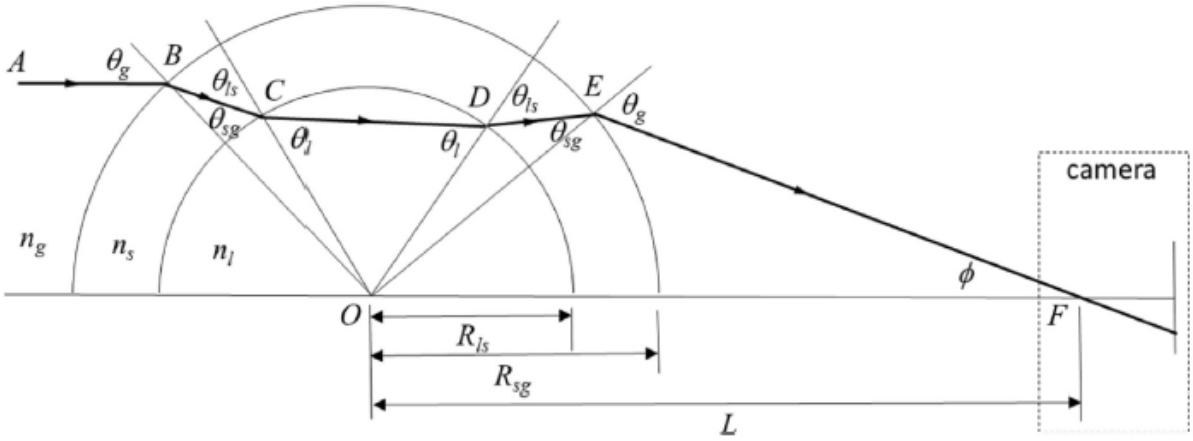

Figure 51 Deviation of a single parallel ray of light by refraction as it traverses from air (refractive index = n_g) into a cylinder with inner and outer radius of R_{ls} R_{sg} (material refractive index = n_s) containing water (refractive index = n_l) and converges at a common point F. The combination of these parallel rays forms the image of an object in the cylinder form the viewpoint of the camera, regardless of if they are occluded or not. [185]

If the produced bubbles are properly resolved by high-speed imaging, the flowrate can be calculated by determining the bubble volume. As the bubbles are confined within a cylinder, picture distortion caused by light refraction must be considered. As shown in Fig. 51, any incoming ray of light, beginning at point A, suffers refractive deviation as where n_g, n_s, and n_l are the refractive indices of the gas, solid, and liquid media, respectively.

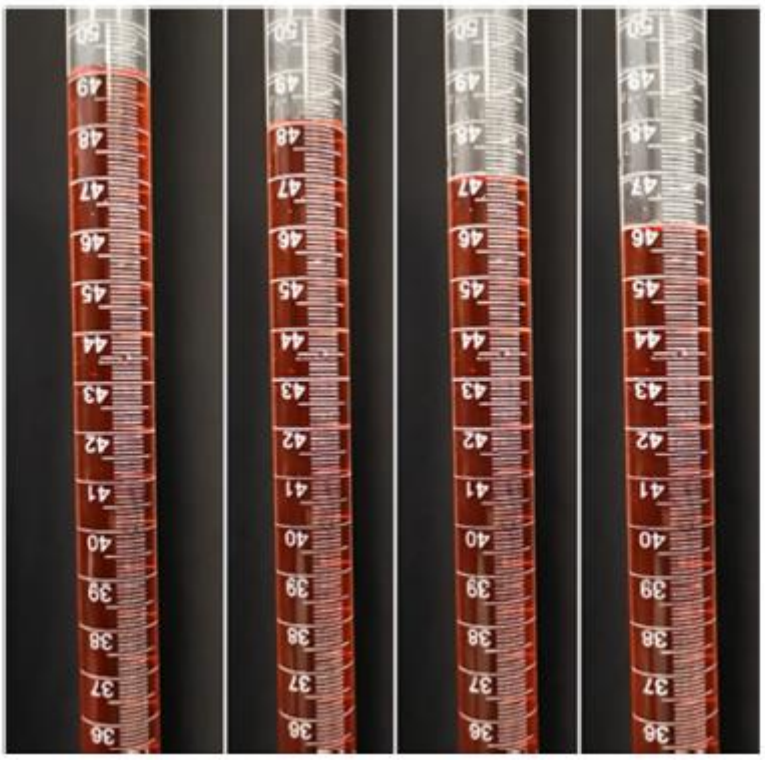

Figure 52 Sequence of images showing the visibility of liquid inside the inverted burette [185]

Even though the rising bubbles are vulnerable to visual blurring, computer-based vision can detect them if they are sufficiently distanced. Image segmentation, often known as separating the bubble from its background, is a standard first step in image processing. Thresholding is the simplest approach for image segmentation. In a normal greyscale image, both the backdrop and the object will be represented by values between 0 and 255. The thresholding procedure produces a binary image in which a grey level value of 0 (black) indicates the background and a grey level value of 255 (white) indicates the object. In order to create a binary image, it is necessary to specify the right threshold level for each recorded frame. This is due to the fact that the ambient lighting

environment is not always constant. A conventional method described by Otsu [186] for doing this includes iterating through all conceivable threshold values and calculating a measure of spread for the pixel levels on each side of the threshold, i.e. the pixels that either fall in the foreground or background. The purpose is to determine the threshold value that minimises the total of foreground and background spread. While this approach is resilient, it is not computationally efficient.

Compared to the conventional method of inverting a gas jar over a trough of water, the accurate filling (and refilling) of the inverted burette with water prior to gas delivery was shown to be substantially easier with the inverted burette. Obviously, the water level in the reservoir should always be maintained below the lowest liquid level in the burette to facilitate liquid drainage during air collection in the burette headspace. In addition, it is possible to incorporate all the components of the apparatus (shown in Fig. 50) on a single retort platform, facilitating portability and storage after use. If desired, any gas collected in the inverted burette can be harvested from the top of the burette (simply by opening the stopcock and pouring more water into the burette) for further compositional analysis.

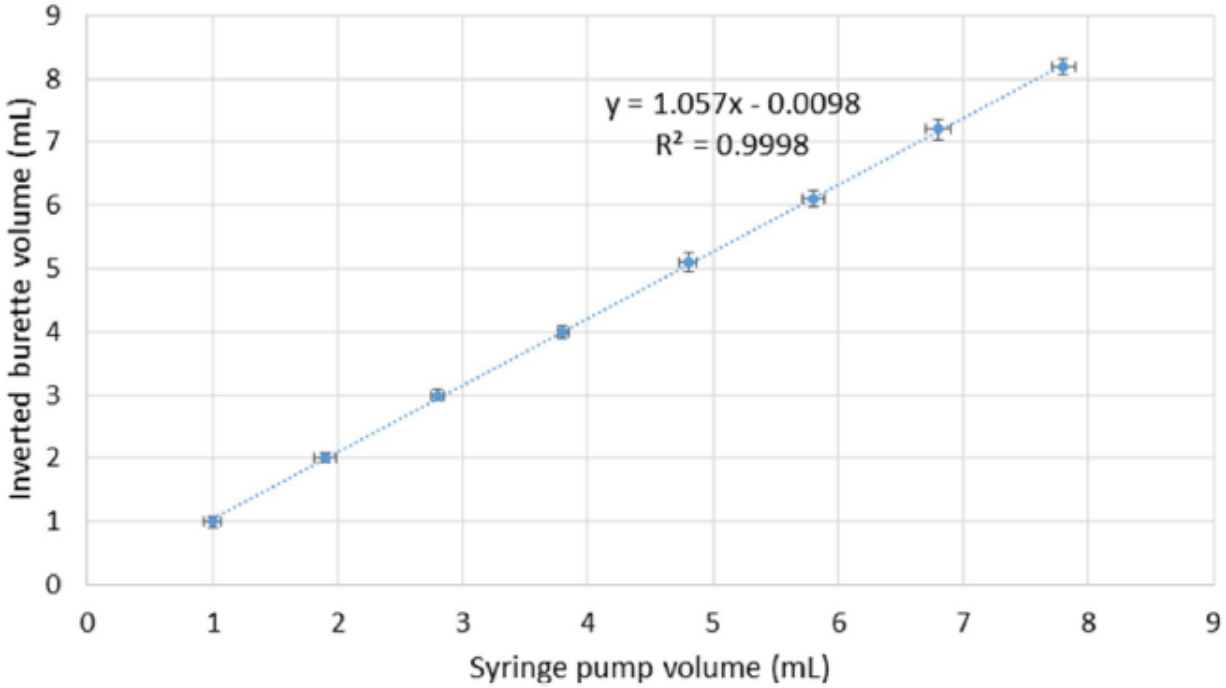

Figure 53 Graph of gas volumes measured on the inverted burette against the discrete volumes delivered using the syringe pump [185]

When the gas volume is provided discretely at a flowrate of 0.57 mL/s (less than the 1 mL/s used to define slow), the water level in the inverted burette is easily distinguishable to enable volume determination (see Fig. 52). Each 0.1 mL graduation corresponds to 10 pixels in the image. If one pixel spacing length is regarded as the measurement precision, then the volume measurement accuracy using this method is 0.01 mL. This 50 mL burette has a 13 mm diameter, whereas a 50 mL beaker has a 40 mm diameter. Using the same recording magnification, the accuracy of measuring from the beaker would be 0.95 mL (based on one-pixel spacing length). The inverted burette method enhances the accuracy of volume measurement by 9.5 times over the inverted jar method.

The findings of the first set of trials (see Fig. 53) indicate that there is a nearly perfect correlation (slope 1) and linearity ($R^2 > 0.9998$) between the pre-specified air volume delivered by the syringe pump and the collected gas volume measured from the inverted burette. In addition, the modest error margins (standard deviation 0.12 mL) of the 10 readings collected at each volume setting demonstrate the high degree of repeatability. When a constant gas flow rate is given (refer to Fig. 54), it is simple and straightforward to establish the flowrate by measuring the bubble volume and the time gap between successive bubbles. This, however, is contingent upon each bubble created

having a fixed volume and the time interval between bubbles remaining constant at any given flowrate.

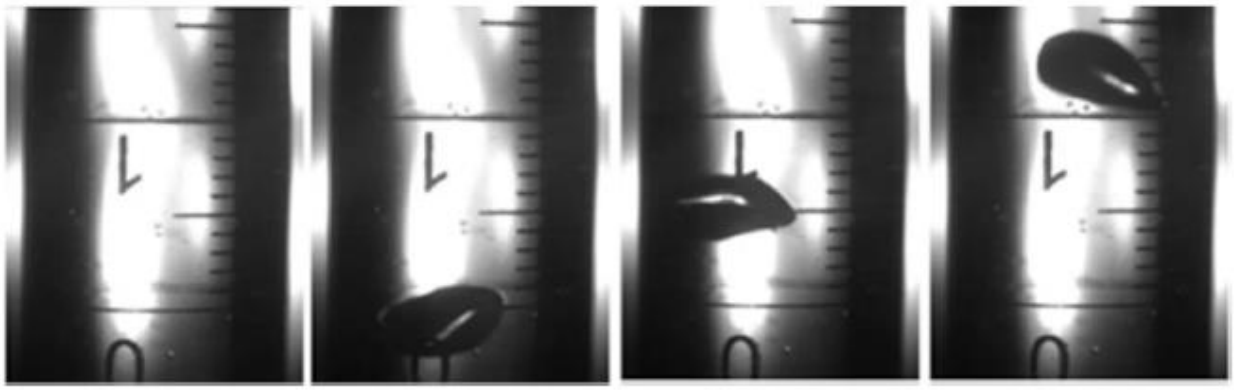

Figure 54 Sequence of images recorded at 125 fps showing the delivery of bubbles form the adapter at the base of the inverted burette [185]

The average bubble count vs volume follows a very linear trend (R^2 > 0.99 in all three cases) in Fig. 55 at each of the three measured flowrates. These results demonstrate that the volume of each bubble (at any flowrate) remains constant, hence satisfying the prerequisite for measuring the flowrate by bubble imaging. In addition, the minimal variance in average counts (1.5) suggested that the procedure is highly repeatable. Based on the slope information, it was determined that the average bubble volumes for flowrates of 0.20, 0.32, and 0.57 mL/s were 55.5, 57.9, and 61.7 µL, respectively.

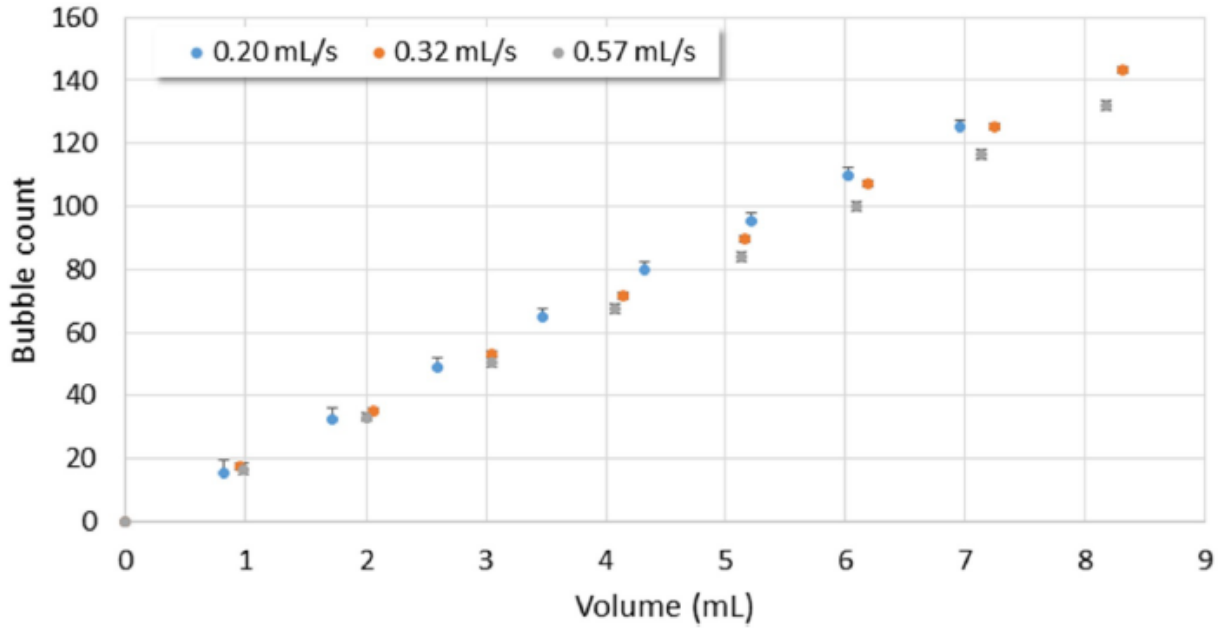

Figure 55 Plots of the average bubble count against the volume at different flowrates of 0.20, 0.32, 0.57 mL/s respectively, averaged over 10 readings [185]

Figure 56 demonstrates that the average bubble count vs time followed a very linear pattern (R^2 > 0.99 in all three cases) for all measured flowrates. These results demonstrate that the time intervals between the formation of any two bubbles (at a given flowrate) are quite regular, so satisfying the second condition for the use of bubble ageing to estimate gas flowrate. As with volume measurements, the average count variance in relation to time is minimal (1.8), indicating that the technique is highly repeatable in this regard as well. When expected, as the gas flowrate increased, the slope of the count-versus-time relationship increased. This results in an average time between bubbles of 0.42, 0.29, and 0.24 seconds for flowrates of 0.20, 0.32, and 0.57 mL/s, respectively.

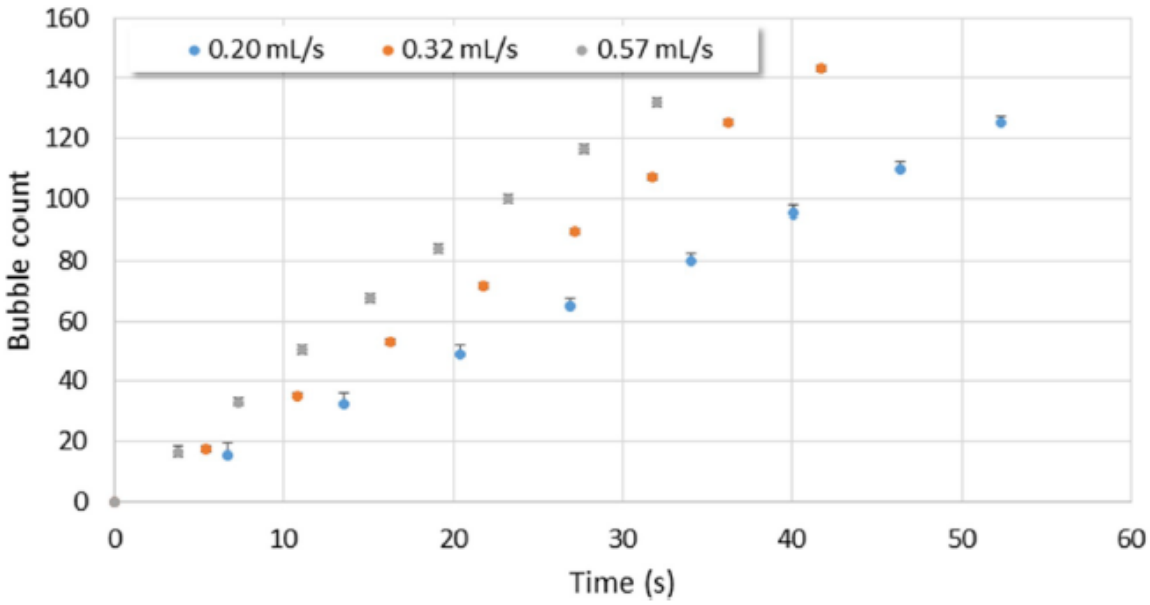

Figure 56 Plots of the average bubble count against the time at different flowrates of 0.20, 0.32, 0.57 mL/s respectively, averaged over 10 trials.

The bubbles do not develop spherical shapes as expected by the Gaddis and Vogelphl model [187] as shown by the image sequences in Figure 54. This is likely due to the effects of the liquid on the bubbles, the bubbles on the liquid, and the interactions between adjacent bubbles, which are worsened by the bubbles' requirement to climb through a relatively confined cross-section. Using imaging techniques to analyse the shape and size of bubbles continues to evolve [188-190]. As the cross-sectional diameter of the cylinder is not significantly larger than the size of the bubble, the current methods do not account for the effects of light refraction, which can be substantial in this situation (see Fig. 54). Fig. 57A–C depicts three instances of ray tracing with varied settings. In all instances, light is visible to be warped towards the central axis. This implies that unless corrections are made, the width of the bubble will be underestimated. When the cylinder's wall thickness is decreased, the degree of distortion increases somewhat (see Fig. 57A and B). However, increasing the thickness of the inverted burette is not possible since it would impede the upward migration of the bubbles. In addition, ray tracing demonstrates that increasing the imaging distance has no effect on distortion (see Fig. 57A and C).

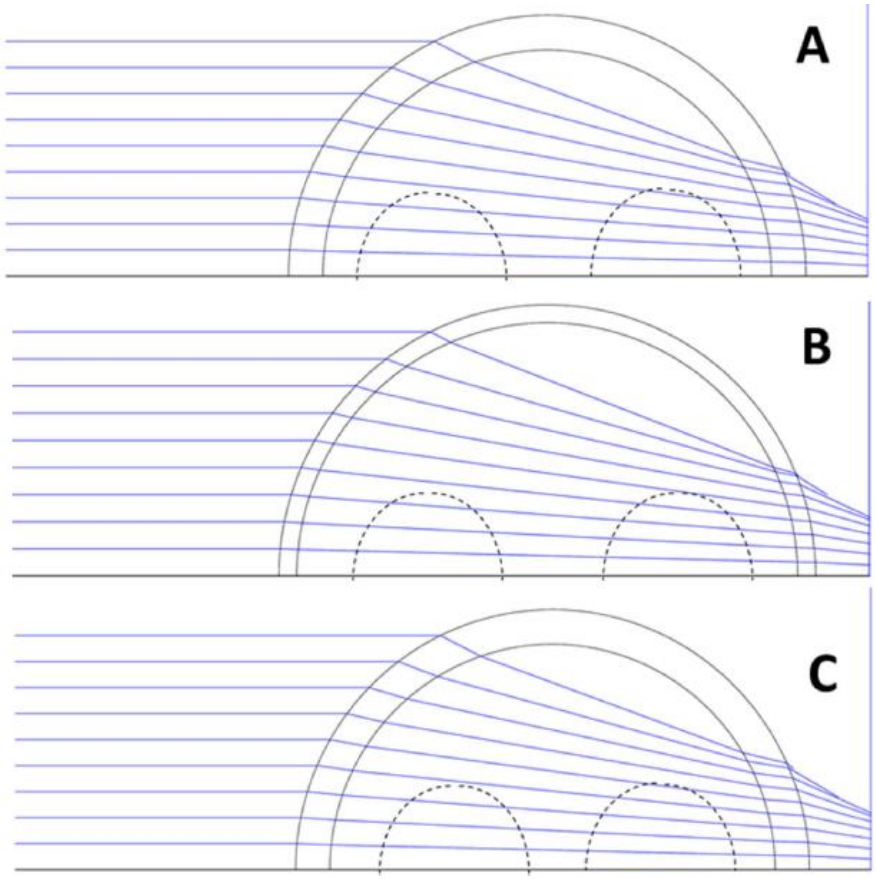

Figure 57 Ray tracing of the deviation of input light beams for A) L = 150 mm, R_{sg} = 7.5 mm, R_{sl} = 6.5 mm, B) L = 150 mm, R_{sg} = 7.5 mm, R_{sl} = 7 mm, C) L = 500 mm, R_{sg} = 7.5 mm, R_{sl} = 6.5 mm. Hypothetical bubble shapes (dashed) are drawn closer and away from F to highlight the imaging distortion in relation to their position in the cylinder. [185]

Efforts to do image rectification are rendered more difficult by the position of the bubble in relation to point F. (see intersection of ray traces relative to the dashed lines indicating bubbles of the same size in Fig. 55A–C). In other words, the correction must also rely on the availability of depth information relative to point F. There is a requirement for a stereo imaging system in which the number of images to be processed is twofold [190]. As the bubbles ascend the liquid column in the burette, they will have a zigzag trajectory [191], making this endeavour more difficult. All of these considerations make it imperative to establish the flowrate by photographing the volume of each bubble. It is also noteworthy that the apparent differences in sizes of the bubbles in Fig. 52 also show the image distortion effect as their positions relative to the camera are not invariant.

Clearly, the optimal method for finding the flowrate is to execute a calibration process (with multiple flowrates given) and then use either bubble counting (during a short time period) or bubble interval measurement to establish the flowrate. This technique should not even necessitate the use of high-speed cameras.

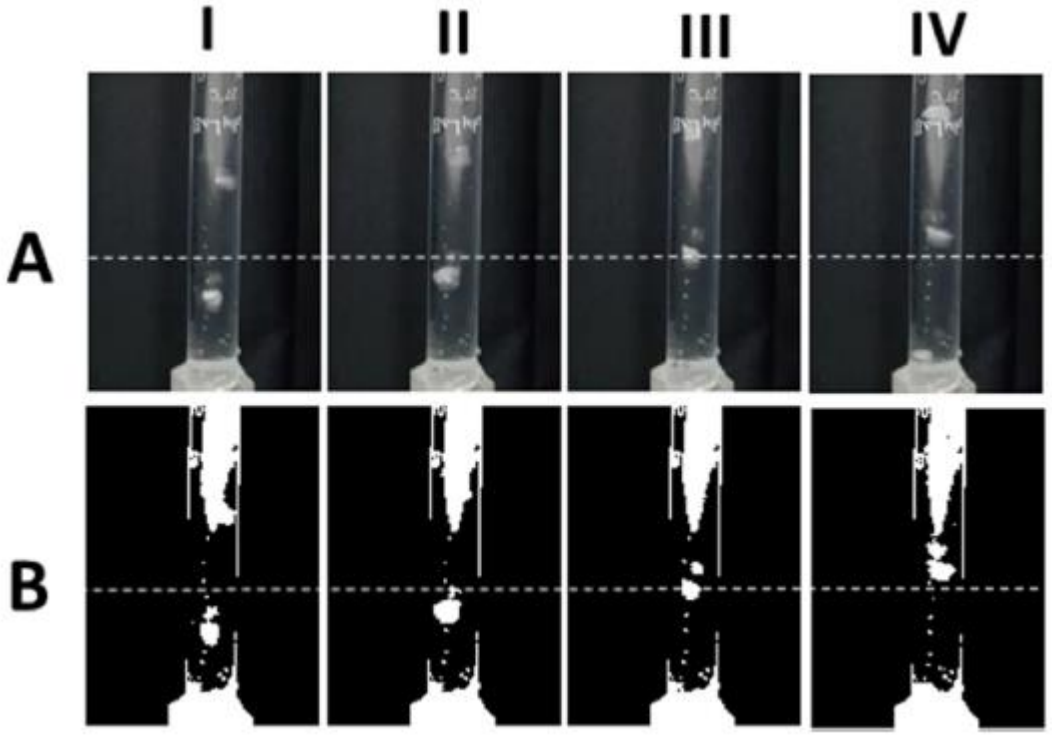

Figure 58 Sequence of images (A) starting from I to IV showing a bubble rising in a column of water in an inverted burette using a standard camera. Sequence of images (B) show the same sequence after binarization. The horizontal dashed line represents the virtual gate for each image sequence. [185]

Figure 56A provides a series of photos (I to IV) depicting the ascent of a single bubble. At low resolution (320 x 240 pixels) and typical 30 frames per second imaging, the bubble appears fuzzier but is still distinguishable from its surrounds. Setting up a horizontal "virtual gate" is a useful method for bubble counting and measuring the interval between bubbles (indicated by the arbitrary dashed line in the images). Traces of the intensity versus location graphs from this gate reveal that it is difficult to determine with certainty the presence of a bubble (see Fig. 57A). The relevant sequence of images from Figure 57A, after being subjected to the binarization procedure based on the thresholds (of each image) obtained, is shown in Figure 57B. Here, the binary state versus location plots (Fig. 57B) reveal that it was accurately predicted that pictures I and IV would not have high binary states along the gate. This facilitates establishing the flowrate using these processed photos by counting bubbles or determining the time between bubbles.

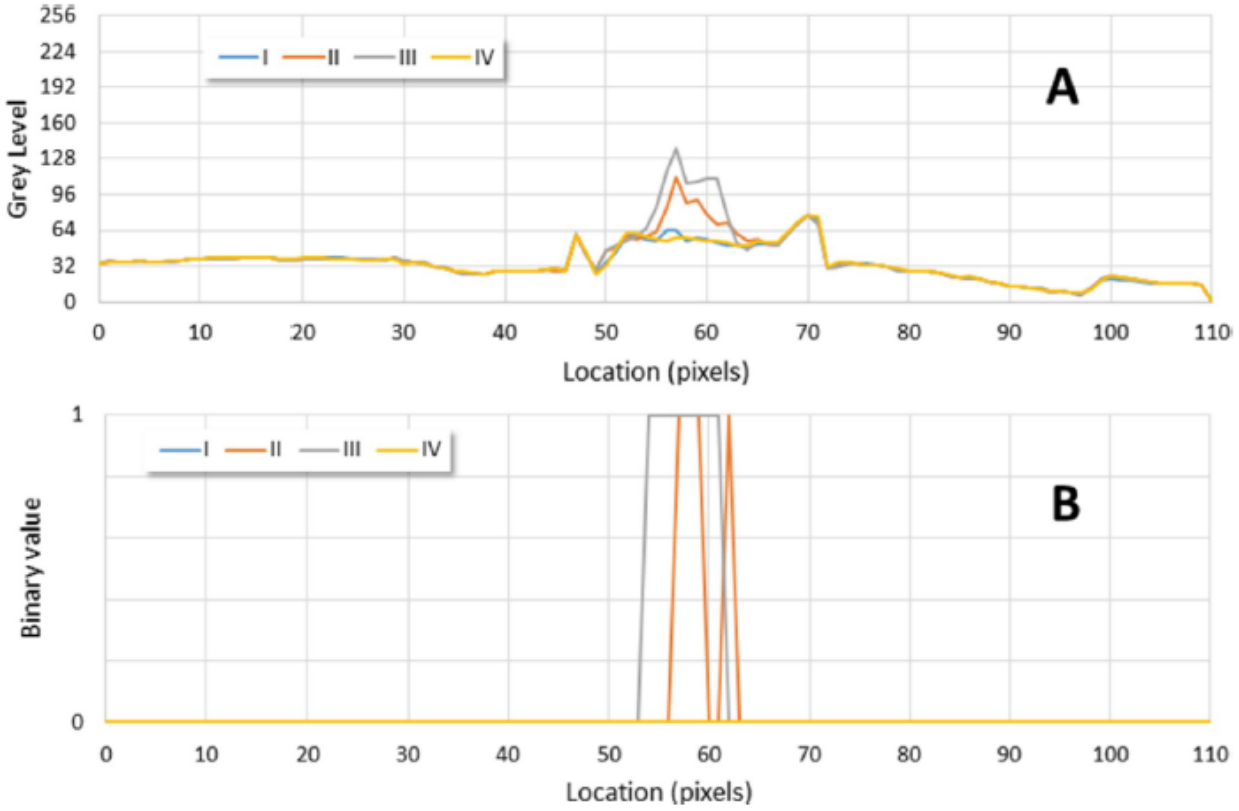

Figure 59 Line plots of the virtual gate position of the image at different times (I to IV) of original image sequence (A) and after binarization (B). [185]

It should be noted that this measuring setup can be modified for travel and storage convenience after usage. In addition, it enables a higher measurement throughput and the simple recovery of collected gas samples for compositional analysis, if required. This technique is advantageous not only for research but also for laboratory experiments and demonstrations involving the creation of gases [181, 192] due to its simplicity of application. It also augurs application in the field for measuring undersea gas emissions [174].

4.3.4 Conclusions

To facilitate the measurement of the volume and rate (1 mL/s) of slowly formed gas bubbles, the approach of utilising an inverted burette with camera imaging is examined. When the gas volume given is discrete at a flowrate of 0.57 mL/s (less than the 1 mL/s used to define slow), the water level in the inverted burette can be separated clearly to simplify volume determination. The pre-set air volume delivered by the syringe pump and the collected gas volume measured from the inverted burette exhibited a slope-to-slope correspondence of 1, linearity of $R^2 = 0.9998$, and repeatable standard deviation of 0.12 mL. Using continuous gas flow, tests at 0.2, 0.32, and 0.57 mL/s found linearity trends of $R^2 > 0.99$ between the average bubble count and volume, indicating that the volume of each bubble (at any flowrate) is constant. Also, for these three investigated flowrates, the average bubble count vs time exhibited linear trends with R^2 values more than 0.99 and a standard deviation of 1.8. This revealed that the time intervals between the formation of any two bubbles (at a specific flowrate) are regular and allow volume estimation.

According to ray tracing calculations, light distortion along the centre axis would result in an underestimation of the bubble's width. This indicated that the optimum way to calculate the flowrate would be to undertake a calibration process (with multiple flowrates provided) and then use either bubble counting (within a short amount of time) or bubble interval measurement. Using an image binarization technique, it was discovered that camera recordings with modest resolutions (320 x 240 pixels) and typical 30 frames per second imagery may be utilised to determine the flowrate by

counting bubbles or determining the duration between bubbles. This showed an accurate determination of the flowrate of introduced bubbles at low speeds.

The findings in this section have been published in H.A. Abid, J.W. Ong, E.S. Lin, O.W. Liew, T.W. Ng, Volume and rate measurement of slowly generated gas bubbles. Flow Measurement and Instrumentation. 72 (2020) 101694.

4.4 Liquid Marble Behaviour with Bubble Delivery

4.4.1 Introduction

The precise actuation of air delivery described in section 4.3, that was based on the system outlined in section 4.2, allowed the speed of slowly released bubbles to be determined with an efficient measurement method, as demonstrated in section 4.3. With the knowledge and capabilities that have been gained, the effects of gas bubbles delivered into a LM are explored in this section.

Micro-bioreactors offer reduced reagent usage and energy consumption, as well as increased control over reaction parameters. It has been used in many fields such as blood typing [59], cell culture [52], and deoxyribonucleic acid (DNA) amplification in polymerase chain reactions (PCRs) [193]. The particle coated layer in LMs limits the ability of gases diffusing into them, acting as a barrier at the liquid-gas interface.

This section explores the generation of a singular air bubble within an LM that is deposited on a superhydrophobic substrate with a hole [19-21]. The suspended air bubble causes localised displacements of the outer shell particles, forming open regions at the apex of the LM. Clearly, this allows additional reagents to be added to the LM prior to bubble rupture and shell reformation.

4.4.2 Theory

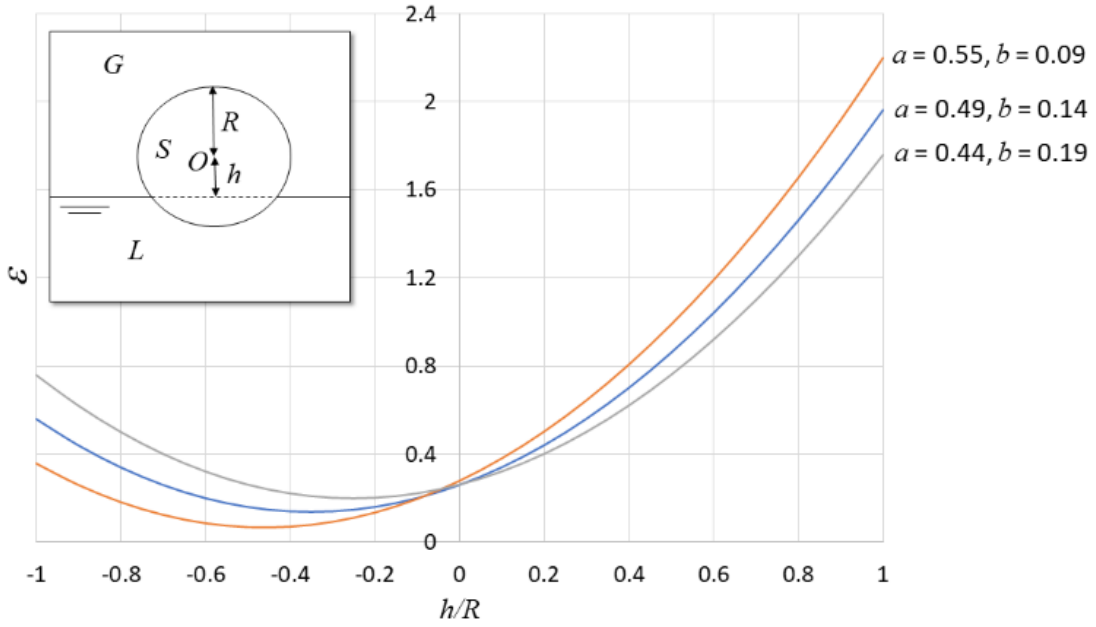

Figure 60 Plots of theoretical surface energy change ε that would occur with h/R relating the position of a particle to the liquid level for different values of proportional parameters (a and b) that relate to the surface tensions of the solid [194]

LMs tend to form a single layer of particles that is governed by capillary forces and free energy. Assuming that each particle is spherical with radius R and its centre O located at height h above the liquid level (Fig. 58), the total surface is given by [195]

$$E = 2\pi R^2 \sigma_{SV}\left(1 + \left(\frac{h}{R}\right)\right) + 2\pi R^2 \sigma_{SL}\left(1 - \left(\frac{h}{R}\right)\right) - \pi R^2 \sigma_{LV}\left(1 - \left(\frac{h}{R}\right)^2\right) \quad (18)$$

where σ_{SV}, σ_{SL}, and σ_{LV} are the surface tensions of the solid-vapour, solid-liquid, and liquid-vapour interfaces, respectively. Using $a = \sigma_{SV} / \sigma_{LV}$ and $b = \sigma_{SL} / \sigma_{LV}$, the equation can be simplified to:

$$E = \pi R^2 \sigma_{LG} \varepsilon = \pi R^2 \sigma_{LV} \left(\left(\frac{h}{R} \right)^2 + 2(a-b) \left(\frac{h}{R} \right) + 2(a+b) + 1 \right) \quad (19)$$

This equation states that for identically sized particles with unaltered LV, describes variations in surface energy with respect to h. The stated values for a and b are 0.49 and 0.14, respectively [196]. Using these values and two other combinations of a and b, it is evident from the plots in Fig. 58 that when the particle is released just above the surface of the liquid (h = R), the equation demonstrates that it will not be completely submerged in the liquid (h = -R) but will instead be partially floating. A LM is formed when a multitude of such particles are present in the shell.

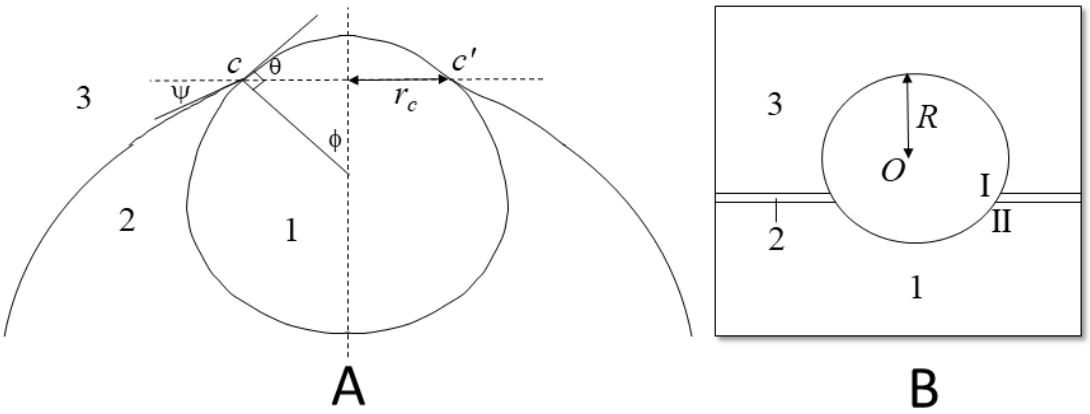

Figure 61 A figure of (A) a bubble at a free surface in the initial static equilibrium position without rupture of film (region extending from c to c') where 2 is in liquid phase, 1 and 3 are in gaseous phases. Hypothetically, in the case of (B) where the shell particle can sit within the thin film, its stability will be governed by the conditions at the three-phase contact point located at I and II. [194]

The stability condition for a single gas bubble within a sessile drop is also analysed. The gas bubble rises due to buoyant forces and creates a liquid thin film at the top of the drop that extends from c to c' (Fig. 59A). Point c and c' can be considered a three-phase contact point if the film is assumed to be thin. If σ_{ij} are the surface tensions of the interfaces (i,j) then force balances in the r- and z-directions respectively give

$$\sigma_{13} \cos\cos\theta = \sigma_{12} \cos\cos\emptyset + \sigma_{23} \cos\cos\varphi - \frac{K}{r_c} \quad (20)$$

$$\sigma_{13} \sin\sin\theta = \sigma_{12} \sin\sin\emptyset + \sigma_{23} \sin\sin\varphi \quad (21)$$

where K is the line tension at the intersection of the 3 phases.

The bubble can attain a position of static equilibrium in which the upward component of surface tension is balanced by the buoyant force. In contrast, the boundary film gradually thins over time and ruptures when it reaches a threshold thickness or when a destabilising force is introduced.

Considering the conditions at the three-phase contact points I and II independently when analysing this hypothetical case (Fig. 59B). According to equation 18, the prescribed height h should be positive at I and negative at II, providing two distinct values for the surface energy. Theoretically, this would render the system energetically unstable. The system has two possible responses. Initially, the shell particle is forced to remain on the film, but as it is unable to remain in this position indefinitely, it will eventually cause the bubble to break, although this is quite rare. The second response, in which the buoyant bubble thin film first forms at the apex before spreading to extend from c and c', is more realistic. This enables the shell particles that were initially located at the bubble's apex to move away from the apex to avoid the unfavourable energy situation.

4.4.3 Materials and Methods

For the particles acting as the LM's protective shell, 10 µm-sized hydrous magnesium silicate (Talc) of commercial quality (Sigma Aldrich, 243604) was utilised. A 40 µL volume droplet of

deionized water was deposited on a superhydrophobic substrate containing a hole, where a large liquid component dwells above the hole and a smaller liquid component hangs over the hole [19-21]. Utilizing a plastic funnel, the Talc particles were directed to completely coat the top component. The excess particles were then removed with compressed air, resulting in a clean LM.

In order to insert air bubbles into the LM, one end of a flexible tube is connected to a 100 µL pipette tip, while the other end is connected to an air-filled tube syringe (1 mL). The syringe was mounted on a precision actuator setup from chapter 4.2 [135] so that its plunger could pump discrete quantities of air. Air quantities varying from 8 to 28 µL could be introduced by placing the pipette tip into the overhanging portion of the LM or sessile drop portion. After delivering the air bubble, the pipette tip was withdrawn from the drop's base. Using a camera (Fastcam), side-view photos of the air bubble in LM and water were captured for study.

On the superhydrophobic substrate, a LM containing a confined air bubble is located. 5 µL of water was added to the top of the LM using the same delivery technique as detailed in the preceding section. For examination, side view photos of the LM with a confined air bubble were captured at 250 frames per second using a high-speed camera (Fastcam). Water was introduced to the overhanging component of the LM using the same delivery system described above, with images taken with the high-speed Fastcam camera.

4.4.4 Results and Discussion

Figure 62A depicts the capacity to create a LM over a superhydrophobic substrate with a hole. The air bubbles of 20 µL and 28 µL, as depicted in Fig. 60B and 60C, clear the LM's apex and displace the particles away from the centre.

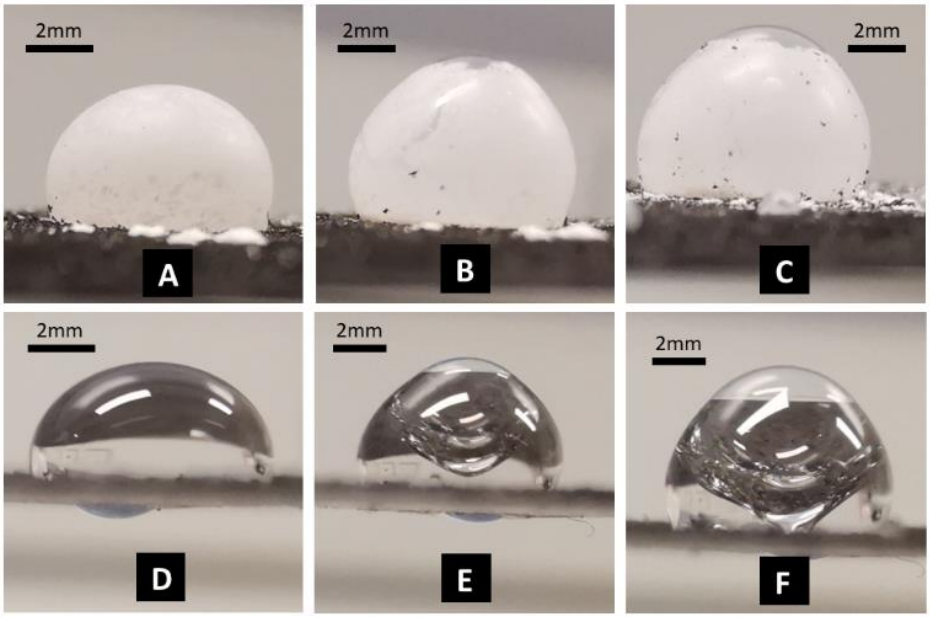

Figure 62 Images obtained of LM with (A) no air bubble, and air bubbles of (B) 20 µL, (C) 28 µL volume inserted. The particles are cleared from the top of the LM. Sessile water drops with (D) no air bubble, and air bubbles of (E) 20 µL, (F) 28 µL volume inserted. [194]

Due to the opacity of the particle shell, the internal air bubble could not be seen clearly; nonetheless, its shape within a sessile water drop may be observed (Figs. 62D – F). As with the LM, the air bubble floats on top of the liquid drop due to buoyancy factors. Due to its superaerophilic characteristics, the bubble can connect to a superhydrophobic substrate at greater gas volumes. This generates a unique circumstance in which the overhanging portion of the drop can be considered distinct from its overhead portion. Additionally, a three-phase contact point is produced on the substrate surface and hole edges (Fig. 63). Experiment results revealed that the air bubble was stable within the LM for up to 10 s before spontaneously rupturing, allowing the

marble to be used in processes for practical applications. As soon as the bubble bursts, the particles return to the apex and rebuild a whole marble (Fig. 62A).

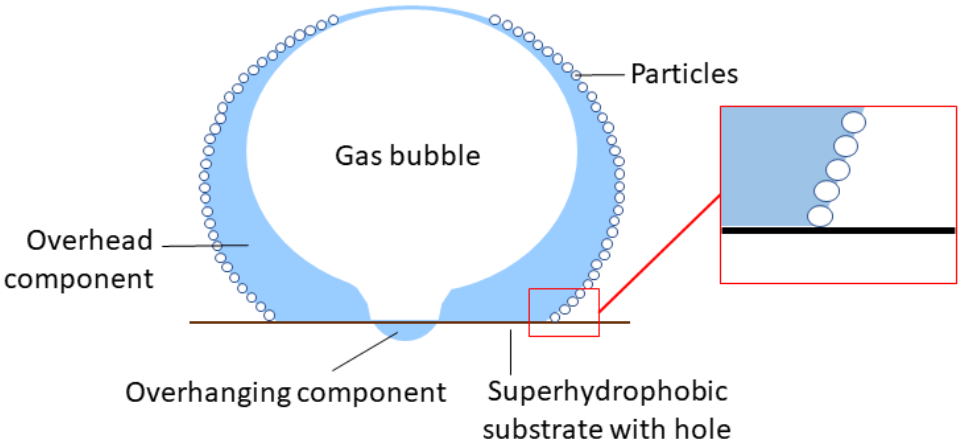

Figure 63 Schematic depiction of the case when the volume of the introduced air bubble is large enough to create contact with the substrate surface. The interaction of shell particles at the contact line is highlighted in the inset. [194]

Both the water drop and the LM exhibit the behaviour of a buoyant bubble. Figure 64 depicts the form profiles of the droplets in relation to the gas volume. Due to the growing buoyant forces, it is noticed that the addition of increasingly larger air bubbles would induce an increase in height in both instances. However, the water drop (Fig. 64A) and LM (Fig. 64B) without a restricted bubble have different shapes, with the former having a flatter, wider shape on the surface. Nonetheless, at the highest volume of injected gas bubbles, the drop morphologies assume comparable geometries.

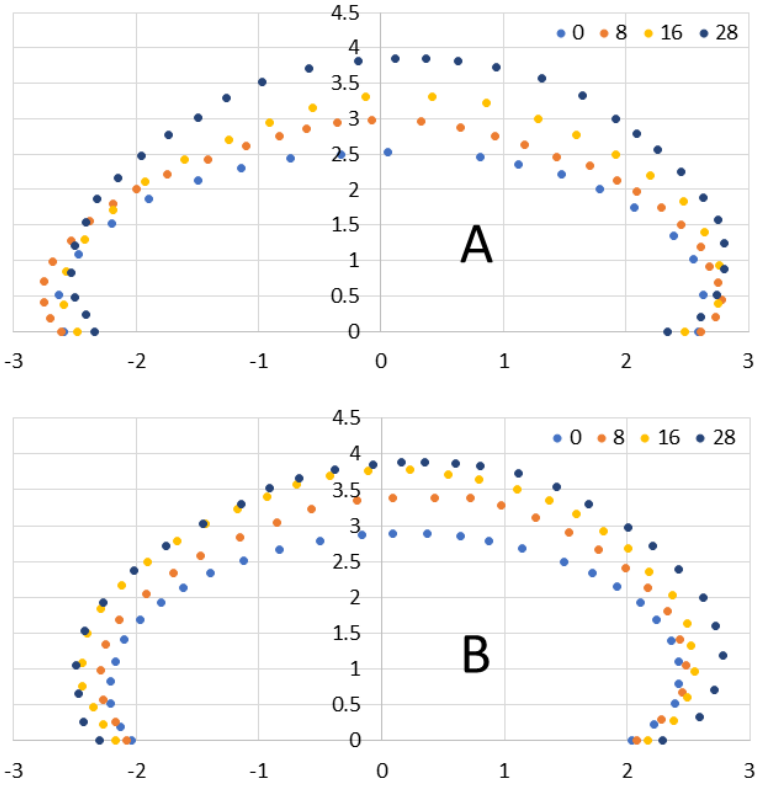

Figure 64 Shape profiles of height versus length measurements are obtained from side view images of (A) water drops and (B) LMs with internal air bubbles of volumes 0, 8, 16 and 28 µL. Different shapes were observed without the internal gas bubble, however, they converged towards almost similar geometries when large enough bubble volumes (> 28 µL) were introduced. [194]

These observations can be explained by the actions that take place at the contact lines. It has been demonstrated that when sessile droplets are disturbed, their positions and angles at the contact lines change [197]. As soon as 8 µL of gas bubble is added, the contact angle of sessile

water drops shifts from an equilibrium position of around 94° to an advanced state of 110° (Fig. 65A). To account for the floating bubble within, the liquid body responds by pushing the contact line radially inwards (Fig. 65B). The drop of the liquid's base length from 5.2 mm to 4.9 mm when 0 and 20 µL air bubble volumes were supplied, respectively, indicates that this movement is not significant. Regardless of the amount of the confined gas bubble, the LM's contact angle remains roughly constant (see Fig. 65A). In the absence of an air bubble, the LM has a greater contact angle (116°) than the sessile drop (94°).

This is consistent with prior findings indicating that the contact angle increases when particles completely enclose the liquid body to create LMs [198]. The observation that the contact angle of the LM without a confined air bubble coincided closely with the contact angle of the sessile drop containing a gas bubble with a volume greater than 8 µL (Fig. 65A) indicates that the presence of shell particles at the interface instantly transformed the contact angle from equilibrium to advancing (inset of Fig. 63). This initial transformation also moves the contact line inwards radially towards a minimum with a base length of 4 mm (Fig. 65B). As the size of the air bubble increases, the base length increases proportionally. For a 20 µL gas bubble, a tiny change of 4.3mm was recorded for a water drop, where the same behaviour happens.

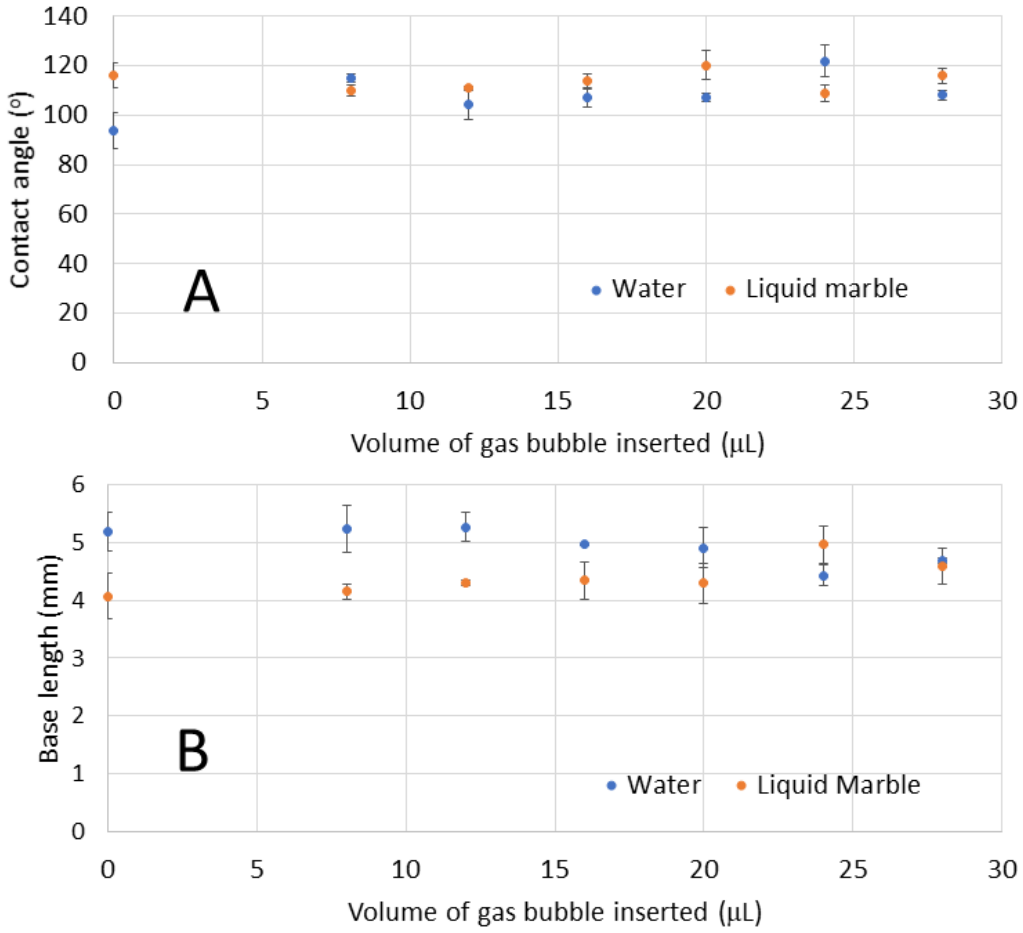

Figure 65 Plots of the (A) contact angles and (B) base lengths measured versus the volume of gas bubble introduced, based on 5 repeated measurements. [194]

With a 28 µL gas bubble, the water droplet and LM contact angle and base length values are extremely similar. At this volume, the internal gas bubble reaches the substrate in the water drop (Fig. 62F) and is presumed to touch the substrate in the LM due to the lack of interaction between the gas bubble and the particles. Since the internal bubble is now affixed to the substrate, the liquid body no longer modifies its contact angle and contact line in response to variations in energy caused by system disturbances. This may be observed in both the water drop and the LM. This

pinning effect also explains why a liquid drop and a marble with a 28 µL air bubble have the same height, but not at smaller volumes.

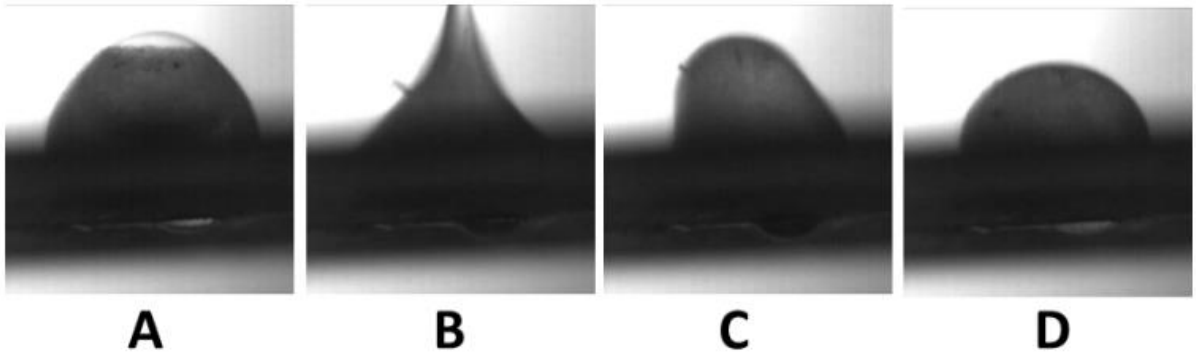

Figure 66 A sequence of high-speed camera images of a 40 µL LM with a 12 µL confined gas bubble (A) where the shell particles are moved away from the apical region. When 5 µL of water was dropped onto the apex, jetting was observed (B), and then a series of oscillations with reduced axial amplitude (C) and finally stabilised to the original LM shape with complete particle encapsulation (D). [194]

When the air bubble in the LM is removed, either spontaneously or through contact, the initially displaced particles at the top will re-join, restoring the LM's entire encapsulation. The sequence of high-speed camera photos from (A) to (D) in Fig. 66 depicts the condition in which a drop of liquid administered at the apex of an LM containing a 12µL air bubble ruptures the bubble. Since energy cannot be dissipated by outward-traveling radial waves, the LM must experience a series of axial self-oscillations with diminishing axial amplitude to regain equilibrium (Fig. 65C). Eventually, the oscillations cease with the full restoration of the LM (Fig. 65D). Using this simple confined air bubble technique, it is possible to introduce chemicals into LMs by the generation of temporary localised shell-free surface areas.

The jetting must be performed directly above the LM's apex for two liquids to combine. If the drop is offset from the apex (Fig. 66B), the bubble can deflect the extra liquid away, even if some of it touches it (Fig. 66C). Due to buoyancy, the bubble then returns to its location at the top of the LM (Fig. 66D). As the perturbations are rapid, the motion of the particle clearing region acting within the energy limitations to maintain stability demonstrates the system's potential to adapt dynamically as opposed to quasi-statically.

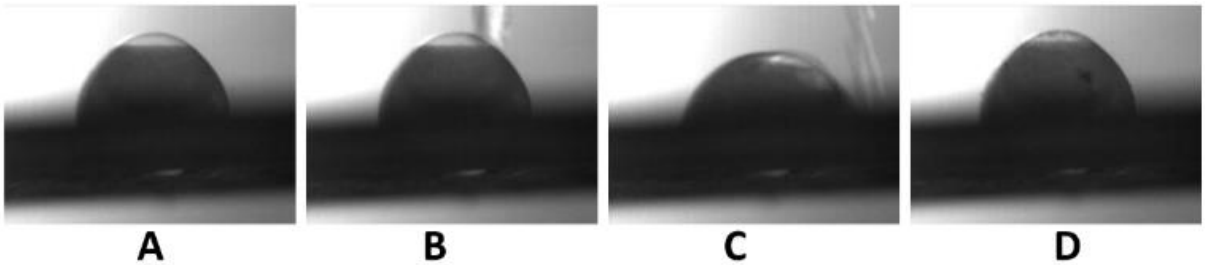

Figure 67 A sequence of high-speed camera images of a 40 µL LM containing a 12 µL gas bubble inserted (A), where 5 µL of water dropped at a slight offset position from its apex (B) resulted in the added liquid being deflected away (C), which leaves the initial LM unchanged (D). [194]

Since the LM is sitting on a superhydrophobic substrate with a hole, it might be argued that reagents can be added through its overhanging component, rendering the air bubble approach unnecessary. However, the addition of liquid simply increases the size of the overhanging component, which exhibits features of a pendant droplet (Fig. 68). This demonstrates that even if the droplets are connected through the hole, they can behave independently.

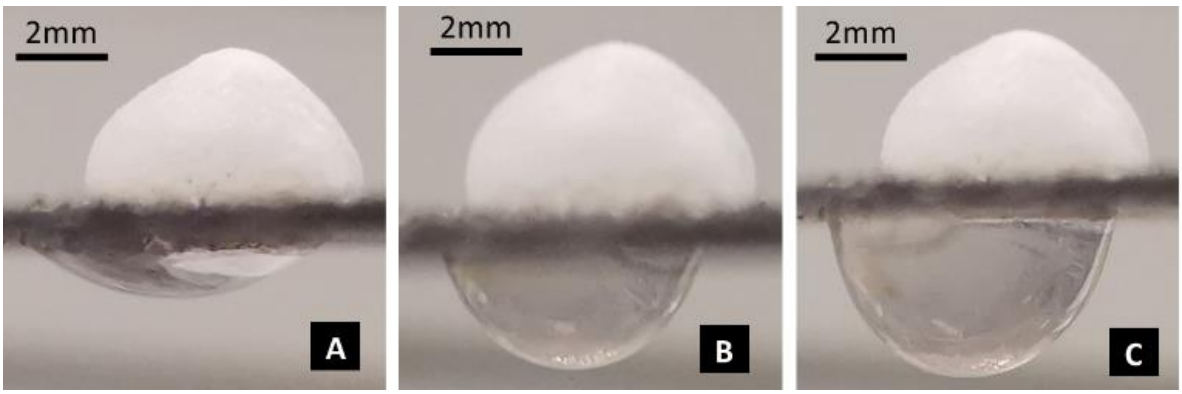

Figure 68 Images of a 40 µL LM with (A) 20 µL, (B) 40 µL, and (C) 60 µL water delivered via its overhanging component. [194]

4.4.5 Conclusions

This section shows the ability to dispense a single gas bubble to reside stably within a LM, resulting in the clearance of particles at the shell's apex. The physics in which the particles will eschew the thin film region of the bubble due to unfavourable energetic conditions is shown. This causes the transient opening of the particle shell allowing for addition of reagents with concomitant bubble rupture followed by full particle reformation, allowing for a novel simplified approach of exploiting LMs.

The findings in this section have been published in E.S. Lin, Z. Song, J.W. Ong, H.A. Abid, D.C.K. Chung, S.H. Huynh, O.W. Liew, T.W. Ng, Liquid marble clearance and restoration using gas bubble insertion and bursting. Soft Matter. 17 (2021) 2512-2517.

4.5 Electrolysis Driven Bubble Delivery in Liquid Marbles

4.5.1 Introduction

As highlighted in section 4.4, air bubbles can stably reside in a LM only for a certain period of time. This section examines a method of introducing gas bubbles into the reaction region with minimal contamination (Fig. 69). As described previously, a drop is first dispensed onto a non-wetting substrate with a hole. Subsequently, a second droplet is added to the underside of the plate. Two liquid regions are formed, the overhead and overhanging respectively, which are separated by the hole in-between. The electrodes are placed in the overhanging component, where an external voltage supply starts the electrolysis reaction.

It has been shown that sessile drops can be sustained on non-wetting substrates with a hole [19-21], from which LMs can be created and gas bubbles introduced into the liquid body through that hole [194]. The wetting characteristics of the substrate have also been found to permit the liquid body to assume an overhead (sessile) as well as overhanging (pendant) component that is connected through the hole of the substrate [20]. This feature is harnessed here in an attempt to create a LM microbioreactor out of the overhead component, that can be aerated on demand via electrolysis as shown in Figure 69.

Electrolysis of water has been used to generate gas bubble streams, which are harnessed for flow visualisation in fluid experiments [199]. The use of these hydrogen/oxygen bubble streams can remove waste contaminants, generate hydrogen for energy and be used to monitor the progression of processes [200, 201]. However, it cannot be used to improve the aeration of the internal contents of a LM without disrupting the chemistry in the medium.

The generation of gas by electrolysis in the overhanging component ensures that the composition in the overhead component is minimally affected in the process. Apart from this, investigations were also conducted to establish the interaction of the bubbles with the encapsulating particles as well as the stability of the bubbles needed for aeration.

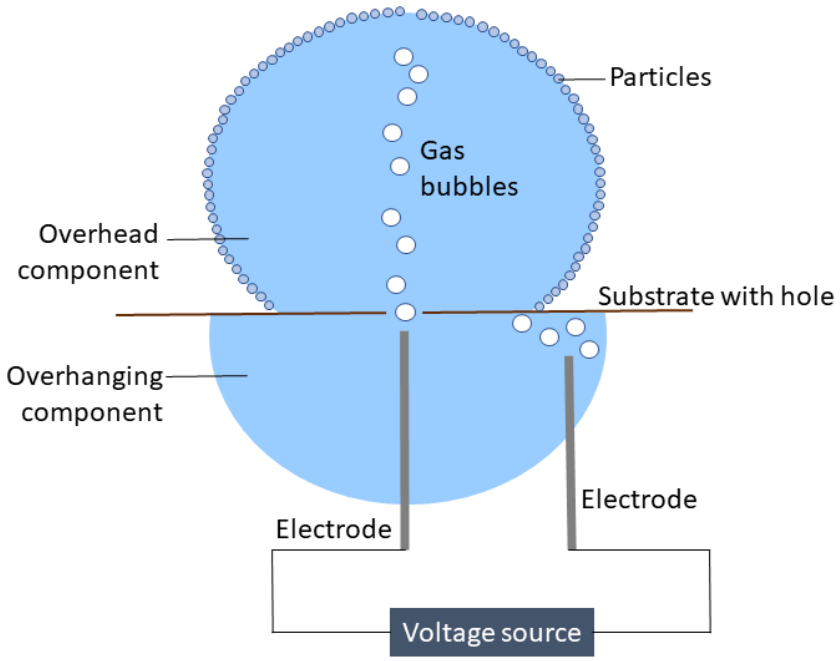

Figure 69 Schematic description of the method where a liquid body deposited over a hole on a non-wetting substrate forms an overhead and overhanging component. Coating of the overhead component with hydrophobic particles produces a LM. Electrodes inserted into the overhanging component create bubbles when an electrical voltage is applied. By placing one electrode near the hole, a stream of gas bubbles is produced and travels upwards by buoyancy into the overhead component. Placement of the other electrode near the contact line of the overhanging component facilitates release of the gas generated there to the environment. [127]

4.5.2 Theory

Two situations based on the medium used to fill the overhanging component are considered here. With sodium chloride solution, its electrolysis yields

$$2NaCl + 2H_2O \rightarrow 2NaOH + H_2(g) + Cl_2(g) \quad (22)$$

Hence, by keeping the electrode near the substrate hole as the cathode, hydrogen gas bubbles can be released to the overhead component. As a dense energy source and good electron donor, hydrogen can be exploited by aerobic bacteria to support respiration and carbon fixation [145].

When water is used as the overhanging component, its electrolysis produces

$$2H_2O \rightarrow 2H_2(g) + O_2(g) \quad (23)$$

By having the electrode near the substrate hole acting as anode, oxygen gas bubbles can be generated to aerate the overhead component. Although the shell of a LM is deemed to be gas-permeable, it is unclear whether simple diffusion will allow physiologically-relevant oxygen levels to be maintained within its interior. Hence, the capacity for on-demand oxygen supplementation would be useful in fine-tuning oxygen concentrations to meet cellular requirements and minimize hypoxic conditions that can lead to aberrant gene expression and cellular behaviour [202].

4.5.3 Materials and Methods

4.5.3.1 Substrate Creation

The substrate was created using the same method described in section 3.2.3.

4.5.3.2 Experimentation

The slide was oriented with its highly non-wetting side facing upwards and distilled water of 10 µL was dispensed above the hole on it using a pipette to form the overhead component. Following this, 10 µL of liquid (either distilled water or 0.1 mM sodium chloride solution) was dispensed below the hole to form a prominent overhanging component. Copper electrodes of 0.4 mm diameter were then inserted into the overhanging component and driven by a stabilized DC electrical supply ranging from 1 to 10 V. Initially, no particulates were deposited on the overhead component to form the LM shell. This was to allow visual confirmation that the bubbles generated from the electrode placed near the hole were small enough to traverse the hole and move upward into the overhead component. The overhead component was later coated with Talc to form a LM to assess the influence of the electrolytic generated bubbles on the particulates.

4.5.4 Results and Discussion

From the images of drops created via the deposition of distilled water on the substrate, the average apparent contact angle was 158°. This indicated that the surface was superhydrophobic.

When the electrode was properly located relative to the substrate hole, it was found that the bubbles generated from it were able to traverse past the hole and move upward into the overhead component. This was found to reproducibly achieved (see Fig. 70a). Misalignment of the electrode however would result in collection of the bubbles at the bottom surface of the substrate (see Fig. 70b). When the overhead component was coated with Talc to form a LM, the passage of bubbles did not result in shell clearance at the apex (see Fig. 70c), a phenomenon that was previously shown in section 4.4 to occur when a large enough bubble was created [194].

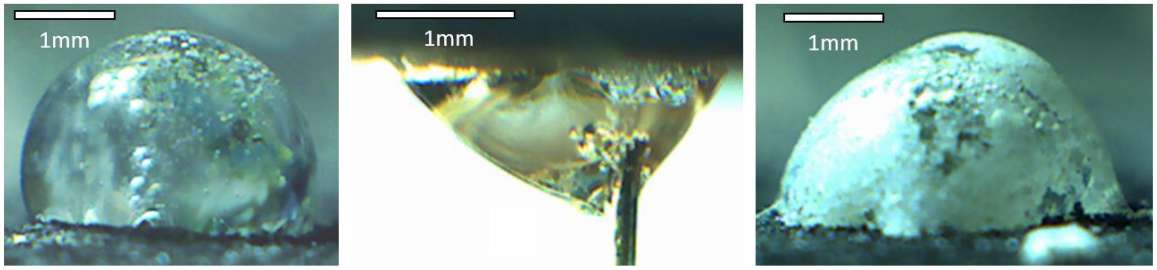

Figure 70 Image of (a) the overhead component without particulate encapsulation where bubbles generated from the overhanging component by electrolysis are able to traverse the hole in the substrate and enter the overhead component. Poor alignment of the electrode causes (b) bubbles to be trapped at the bottom surface of the substrate. When (c) the overhead component is encapsulated by particulates, the passage of bubbles into it did not result in clearance of the particles from the apex. [127]

The physics of gas evolution from the electrodes due to electrolysis proceeds through three phases: nucleation, growth and detachment [203]. Bubbles start to nucleate at the electrode once the liquid becomes highly supersaturated. They grow with the dissolved gas diffusing onto the electrode surface or by coalescence with other nearby bubbles. Detachment then occurs when the forces that push them away overcome the surface forces that bind them (to the electrode). The mechanisms involved in these three phases are understandably complex and have been extensively studied.

In this application, the motivation is to generate a stream of bubbles at low enough detachment rates to be measured by image analysis [185] in relation to the voltage that is applied across the electrodes, as shown in section 4.3. These low rates are also amenable for the purposes of aeration. The outcomes, shown in Figure 69, indicated an expected increase in oxygen and hydrogen bubble generation rate as the voltage was increased. The rate was significantly higher with the latter (~28 times at 6 V) due to the ionic nature of the sodium chloride solution that facilitates electrolysis. It is also noteworthy that in the case of hydrogen generation, the bubble generation rate reached its maximum when the electrode potential attained 6 V.

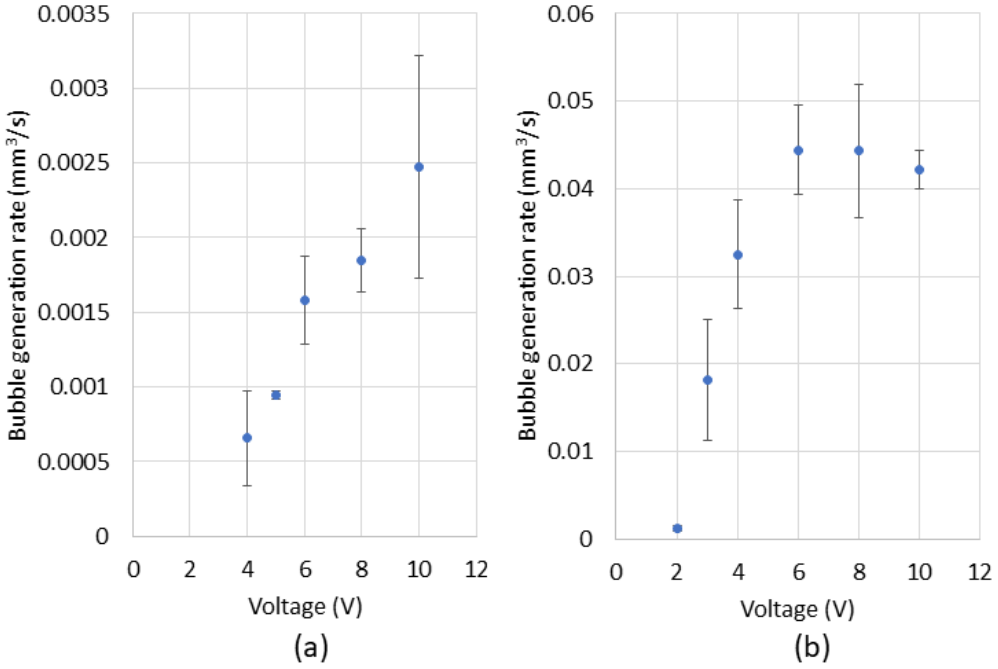

Figure 71 Graphs of the bubble generation rate of (a) oxygen and (b) hydrogen measured as a function of the voltage applied to sodium chloride solution in the electrolysis experiments. [127]

When the bubbles floated upwards, they would eventually interact with the liquid-gas surface. The liquid film that is created there would then undergo thinning to a point where it is no longer

sustainable, resulting in bubble rupture [194]. If this rupture is instantaneous (as soon as the bubble reached the interface), the generated bubble stream may not be helpful in aerating the overhead component. The parameter that controls the thinning rate of the bubble film (and thus impacts its longevity) is the Bond number (Bo) [204, 205].

$$Bo = \frac{\rho g R^2}{\sigma_o} \tag{24}$$

where ρ = liquid density, g = gravitational acceleration, R = bubble radius and σ_o = surface tension at the bubble/liquid interface. From the average size of the bubbles generated, we have Bo ~ 0.002, and for low Bo ≪ 1 systems, surface tension should dominate, causing the bubble to remain typically spherical under the surface as buoyancy is not strong enough to deform the interface. Based on lubrication theory, the film for small bubbles would decay as a function of extensional viscous stresses and capillary drainage [206]. The image sequence in Figure 72 shows that the rate of arrival of the bubbles at the interface is clearly greater than the rupture rate. This then permits their accumulation, which in turn helps to aerate the overhead component. The bubbles also predominantly assumed spherical shapes that do not deform the interface, affirming the Bond number characterization of their behaviour [204, 205]. It is noteworthy that the upward movement of some of the bubbles, in particular those that were larger in size, can result in their assumption of shape asymmetry and even experiencing break up. This corresponds to the observations previously reported [207]. As expected, the small bubbles spread out near the apex of the overhead component with time due to buoyancy (see Fig. 72(c)). These smaller bubbles also confer the added benefit of enhancing aeration [208].

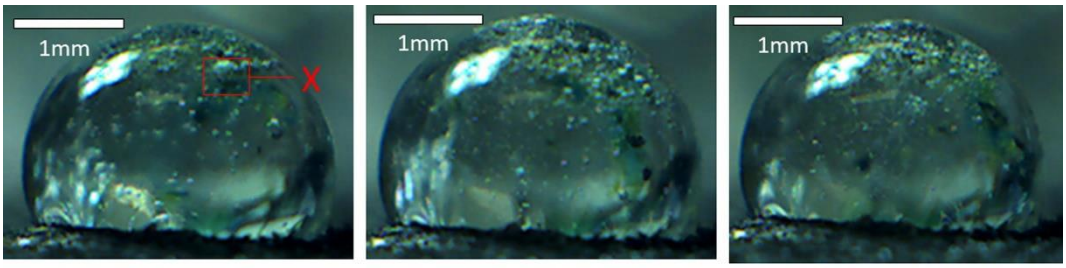

Figure 72 Sequence of time-based images of the bubbles in the overhead component (a) immediately, (b) 3 s, and (c) 5 s after cessation of voltage applied to the electrodes. The tendency of shape asymmetry and break-up of the relatively larger bubbles (such as that indicated by X) and their accumulation at the apex with time was found.[127]

At this juncture, it is important to note that when particulates are present at the liquid-gas interface, the ability of gas bubbles arriving there to maintain their stability may be altered. Yet, if bubble deformation and thus the Bond number remains the primary factor in determining stability, surface tension alterations would likely play the most significant role. Previous studies have shown that increases in surface tension are exhibited when PTFE particles were used to construct the LM [209]. However, this would in turn lower the Bond number even further, allowing the majority of gas bubbles arriving at the interface to remain spherical. As a consequence, one would envisage there to be no significant alteration in the behaviour of the majority of gas bubbles arriving by buoyancy at the liquid-gas interface.

For this reason, it is fair to assume that the generated small bubbles would behave similarly and distribute out at the apex of a shell-covered overhead component, even though visual confirmation was not possible. When these bubbles interact with the particles, they may appear to be stably supported by a “negative pressure” acting down on them due to the force interaction between hydrophilic floating microparticles [210].This mechanism however should not be operational here since the Talc particles used are hydrophobic. It should be noted that the absence of any particle clearance at the apex followed by rupture does not imply that all the bubbles generated would remain in the overhead component indefinitely. The sequence of images in Figure 73 exhibited movements in the cluster of particles with time, providing indirect evidence of bubble bursting

processes at the interface. While the aeration method here was demonstrated on LMs created with a solid phase encapsulation, it should conceivably also work with composite LMs (containing a solid and liquid phase encapsulation) that have been found to be more resistant to coalescence [211].

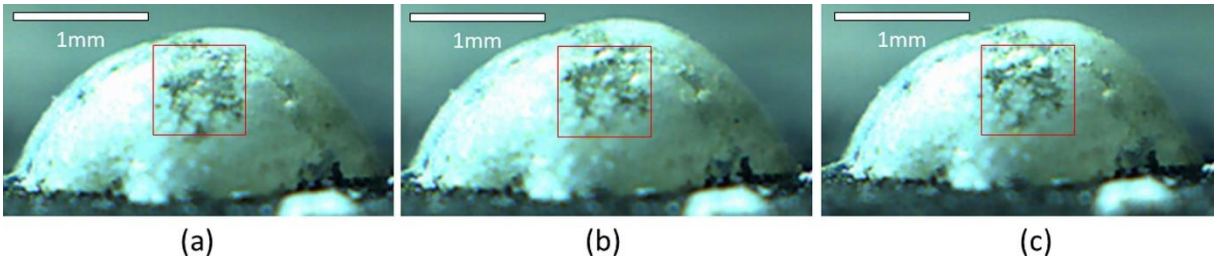

Figure 73 Images of the overhead component encapsulated with particles with time (a) to (c) showing cluster movement in the region bounded by the box that indicates bubble bursting processes occurring. [127]

4.5.5 Conclusions

This section shows the generation of hydrogen and oxygen bubble via electrodes after applying <10V in the overhanging component of the LM. Proper alignment of the electrodes allowed the gas bubbles to travel to the overhead component, providing aeration with minimal alteration of the chemistry. Aeration is assisted by the break-up of bubble into smaller sizes that spread over the apex of the droplet. This technique of on-demand aeration of LMs promotes applications of LMs as microbioreactors [69]. Hydrogen gas has been found to support the respiration and carbon fixation of aerobic bacteria [145], by implementing this technique, controllable, low contamination method of hydrogen aeration is established. Since it is conducted on a sheet of non-wetting surfaces, an array of LMs may be created resulting in an upward scaling manner of aeration.

The findings in this section have been published in E.S. Lin, Z. Song, J.W. Ong, H.A. Abid, O.W. Liew, T.W. Ng, Liquid marble microbioreactor aeration facilitated by on-demand electrolysis. Results in Chemistry. 4 (2022) 100334.

4.6 Chapter Summary

The efforts in this chapter relate to studying the role that gas bubbles can play in liquid marbles. This was done because when two phases (liquid and gas) exist together, the mechanics is no longer as straightforward. Understanding this well enough then opens up possibilities for new applications to be developed.

Section 4.2 served as a preparatory effort in terms of getting the instrumentation needed to deliver the gas bubbles effectively. It was found that the use of syringe pumps was shown to provide a precise method of delivering liquids precisely. Hence, it provided a platform of generating bubbles with specified volumes in a slow and controlled manner.

Section 4.3 served as another preparatory effort in which a method was developed to facilitate the measurement of the volume and rate (1 mL/s) of slowly formed gas bubbles. It was found that when the gas volume is delivered discretely up to a flowrate of 0.57 mL/s (less than the 1 mL/s used to define slow), the water level in the inverted burette method can be separated clearly to simplify volume determination. This section also found through ray tracing calculations for the volume determination to be compromised by distorted. It also found that an image binarization technique, obtained through camera recordings with modest resolutions (320 x 240 pixels) and at typical 30 frames per second imagery. may be utilised to determine the flowrate by counting bubbles or determining the duration between the bubbles.

In section 4.4, the investigations conducted found that the dispensation of a single gas bubble inside a liquid marble would result in the clearance of particles at the shell's apex. Through a theoretical analysis, it was found that the physics behind this lies with the particles tending to eschew the thin film region of the bubble due to unfavourable energetic conditions. This caused the transient opening of the particle shell allowing for addition of reagents with concomitant bubble rupture followed by full particle reformation.

Finally, in section 4.5, it was shown that the generation of hydrogen and oxygen bubbles via electrodes was possible by applying less than 10V to the overhanging component of the LM. Proper alignment of the electrodes allowed the gas bubbles to travel to the overhead component, providing aeration with minimal alteration of the chemistry. Interestingly, the break-up of bubble into smaller sizes that spread over the apex of the droplet would assist in aeration that would facilitate using LMs as microbioreactors.

5. Liquid Marble Freezing

5.1 Preamble

In chapter 4, the effect of gas bubbles in liquid marbles was investigated. In this chapter, the role of freezing, which is a popular method used to convert all liquid phases into solid phases, is considered. Due to the shape similarities between liquid drops and liquid marbles, section 5.2 first investigates the viability of using frozen sessile drops for the cryopreservation of bacteria samples. It has been found that semi-spherical drops are able to improve the survivability of Staphylococcus epidermidis during cryopreservation without the use of cryoprotectants over the use of standard vials. This storage method can be applied to biobanks where the reproducibility and sustainability of bacteria samples are preserved during long-term storage.

Arising from it, the viability to use liquid marbles for a similar purpose was discussed. The freezing of water drops typically results in conical shapes with tip points at their apexes. In section 5.3, the feasibility of using this approach to determine if frozen liquid marbles made from pure or adulterated copper powder could be differentiated was assessed. The availability of this test method can be vital in additive manufacturing, where fabrication using copper powders that have been contaminated has been known to result in poor quality engineering components.

5.2 Cryopreservation with Sessile Drops

5.2.1 Introduction

The phase transformation from liquid to solid via freezing has important ramifications in many engineering and biological applications [212, 213]. Liquids in the form of sessile drops are relatively difficult to handle and to store compared to those that are kept in containers. However, these problems are ameliorated somewhat when the drops are frozen.

The transformation of frozen sessile drops from a spherical morphology to one with a sharp cusp is a result of volume expansion during the phase change from water to ice. It is well understood that the freezing of sessile drops involves two phases: nucleation/recalescence and solidification, with the former occurring instantaneously and is brief in duration. This latter phenomenon occurs at a slower rate and is principally responsible for the transition from liquid to solid drop shape.

Cryopreservation is a regularly used technology for long-term preservation that ensures the quality and viability of microorganisms in laboratories and biological resource institutions. However, microbial viability is negatively impacted by freeze-thaw damage and variations in osmotic pressure throughout the cryopreservation procedure [22]. Utilizing the unique thermal properties of semi-spherical drops, a novel cryopreservation technique is developed that eliminates the requirement for cryoprotectants.

5.2.2 Materials and Methods

Using the same technique as in chapter 3.2.3, the hydrophobic substrate is produced. A culture of Staphylococcus epidermidis was harvested and separated into groups labelled A through F. Sets A through E are distributed as 50 µL of 'bulk' culture contained in 1.5 mL Eppendorf tubes. Set A consisted of original sample, set B consisted of the "killed" sample subjected to thermal treatment at 80 ^{o}C for 45 minutes and allowed to cool to room temperature for 15 minutes, and set C was the "working" sample maintained in the incubator (temperature = 35 ◦C and relative humidity = 80%) for 24 hours. The sets D, E, and F are prepared and then frozen. Set D consists of the original sample, while Set E consists of the original sample with 10% v/v of glycerol added as a cryoprotectant. Set F is identical to Set D except that it is dispensed over the substrate perforations as a series of 10 µL drops.

Sets D, E, and F were frozen by placing the vials of sets D and E as well as the substrates containing set F in a custom container containing dry ice held at 70 C for 24 hours while preventing sample acidification [214]. The samples from sets D, E, and F were thawed to room temperature for five minutes before to testing. Erythrosine B (EB) was utilised to rapidly examine the viability of bacteria.

To make the stain, 0.08 g of EB (200964, Sigma) was dissolved in 100 mL of 10 mM Tris-HCl pH7.5 to achieve a final working concentration of 0.08% w/v. The samples from sets A through F were stained with the EB solution, incubated for 5 minutes, and then centrifuged. Using a pipette, the excess solution was withdrawn from the labelled cell concentrate and the cells were resuspended in 25 µL of PBS. Sets A through F, each containing 10 µL, were put into a Neubauer enhanced disposable hemocytometer (C-Chip, INCYTO) and photographed using a fluorescent inverted microscope (TU2000U, Nikon) and a 40 objective. The camera settings and exposure times for each shot were fixed. The photos were digitally processed (MATLAB, MathWorks) to acquire the intensity measurements at 550 nm wavelength filters that correspond to the death of bacteria cells.

5.2.3 Results and Discussions

Figure 74a depicts the capability of liquid semispherical drops to remain stable on a flat substrate despite the existence of a hole (a). This is because the margins of the hole provide a high degree of pinning despite the strong nonwetting property of the treated substrates [215]. In fact, the substrates can be tilted up to 15 degrees from the horizontal before the droplets are displaced. When these geometries were then frozen at 70 ◦C for 24 hours (see Fig. 74b) in the cold chamber and then thawed to room temperature (see Fig. 74c), they were preserved. In the first 15 minutes, the average cooling rate of the cold chamber was 5.3 ^{o}C/min, as measured by the temperature data. The 122^{o} contact angles of the drops (see Fig. 74d) indicated that it may take a highly semispherical form. Bacteria-containing droplets were removed using a capillary tube and put into the hemocytometer following thawing.

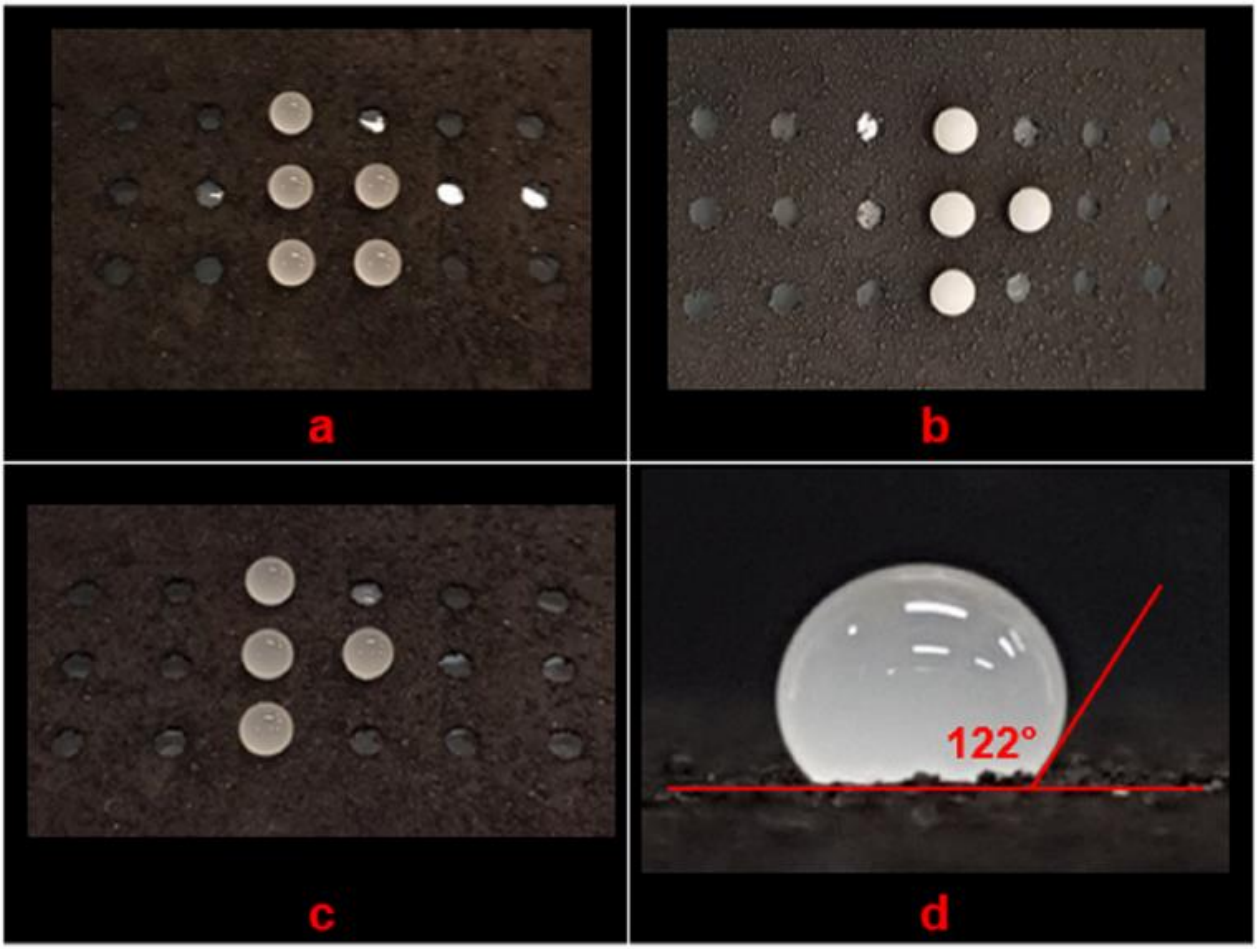

Figure 74 Top view of 5 x 10 µL droplets produced from set E (a) before being frozen, (b) immediately after retrieval from being frozen for 24 h and (c) after thawing in the incubator at 35 ^{o}C for 5 min. Side view of the droplet resulted in a contact angle of 122^{o} (d) [216]

EB functions as an exclusion dye and is excluded in live cells but not in dead cells; thus, samples with a greater proportion of dye-positive dead cells should provide images with greater intensities. Comparing Figure 75a and 75b, the decreased intensity in the former suggested that cryogenic culture storage with drops improved the viability of bacteria cells in comparison to freezing storage in normal vials. In terms of the viability of the bacteria, the intensities recorded from the photographs of the bacteria in sets A and B can be interpreted as better or worse.

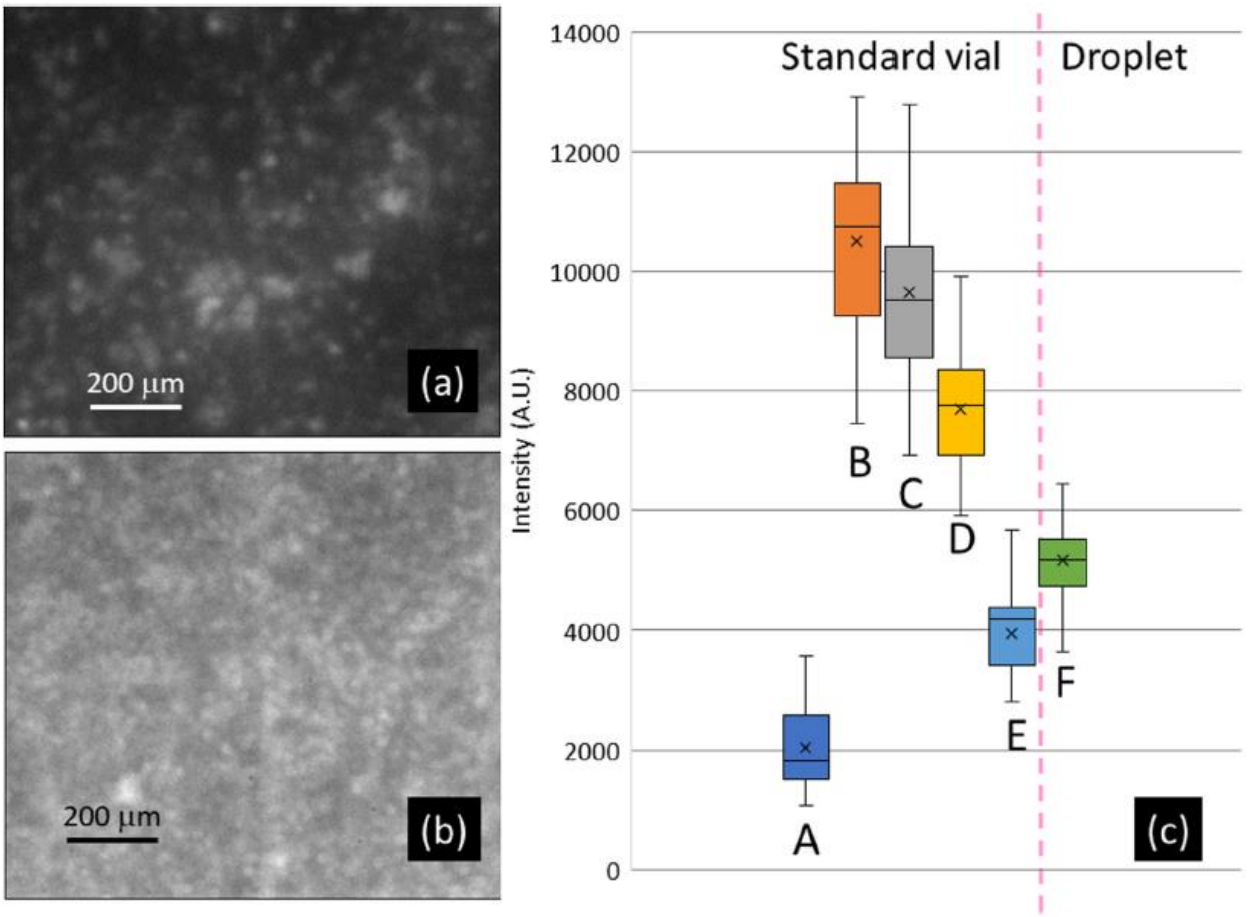

Figure 75 Example microscopic hemocytometer images recorded of the bacteria samples frozen without any cryoprotectants and reconstituted from storage (a) in standard vials (set D) and (b) as semi-spherical drops (set F). Box plots of the intensity readings (c) recorded from 80 samples taken of set E and F as well as the other test sets (A = sample as is, B = sample kept at 80 ◦C for 45 min. C = sample kept at 35 ◦C and relative humidity 80% for 24 h, D = sample frozen with cryoprotectant) are also presented. In each plot, x and horizontal line denote the mean and median respectively. [216]

From this a metric can be developed to describe the relative fraction of bacteria viability in any set x using

$$f(x) = \frac{I_B - I_x}{I_B - I_A} \tag{25}$$

The f values for the samples in sets C,D,E,F were determined to be 0.1, 0.33, 0.77, and 0.63, respectively, based on the collected data. Using semi-spherical drops in cryogenic storage without cryoprotectants improves the survivability of bacteria cells by 1.91 times compared to storage in normal vials, which is close to the 2.33 times improvement reached when cryoprotectants are employed.

In a freezer, substrate sheets holding an assortment of frozen drops will be stored. This offers the advantage of being able to thaw predetermined sample volumes, as opposed to a normal vial. This helps avoid the common practise of exposing stored samples to freeze-thaw cycles, which may affect the viability of bacteria in ordinary vials. For this, fragile frozen drops can be moved with tweezers while the remainder remains undisturbed. Using multichannel pipettes or automated liquid handlers can improve processing throughputs for dividing and dispensing the culture into minute droplets.

Compared to sample storage in traditional vials, the flat sheet design has the advantages of requiring less storage space, being simpler to produce, and producing less plastic waste. The semi-spherical droplets do not roll off the substrate despite an inclination of greater than 15 degrees. The survival rate of frozen Staphylococcus epidermidis samples was comparable to the

standard approach of using hazardous cryoprotectants, indicating the potential uses of frozen droplets.

Keeping samples frozen at the optimum temperature during movement inside and between facilities is essential for preserving the stability of proteins and other molecules of interest in test specimens [215]. During transport to storage or testing facilities, dry ice (solid CO_2) has been utilised for the cryopreservation of tissues, proteins, and blood. It plays a crucial part in cold chain activities due to the fact that it is simple to manufacture, readily available, and simple to manipulate with insulated gloves.

Cryopreservation of blood samples during transport is a crucial component of sample management quality in scientific research. For the purpose of encapsulating a 1.5 mL vial of frozen blood sample, a heat-insulating design employing salt water with a weight-to-volume ratio of 23.3% was investigated. The dry ice-cooled PCM and vial sample were maintained at 20^{o}C prior to flight and could be maintained at -20^{o}C for 70 minutes.

Simulations demonstrated that freezing the vial containing the blood sample with dry ice before to shipment resulted in a more uniform temperature distribution over time (Fig. 76). The temperature parameters derived from simulations agreed well with the results of prior research [217], indicating that whole blood preserved at -20^{o}C was highly resistant to the PT test. The sample that was completely frozen prior to sloshing had a greater PT and aPTT value, suggesting that freezing helped to reduce the extent of blood coagulation caused by sloshing.

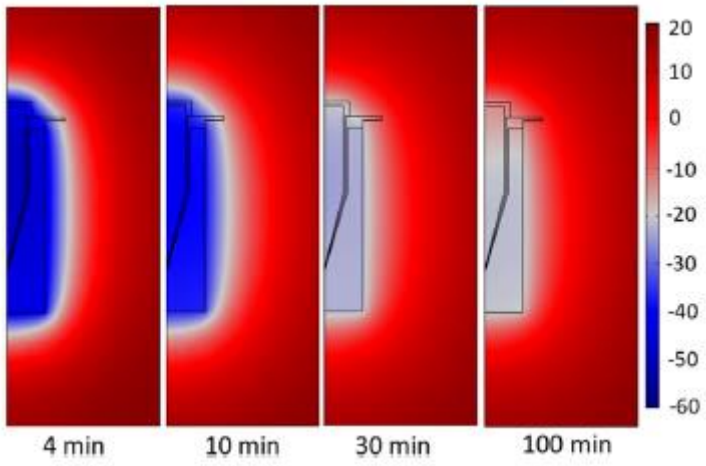

Figure 76 Temperature distributions of the system after periods of 4, 10, 30, 100 minutes in which the vial holder, sample vial and sample were initially stored in dry ice [218]

It is essential to evaluate the freezing rate because it is another component that determines the results of blood coagulation. Despite the freezing temperature and sloshing conditions remaining similar, the faster freezing rates tended to increase blood coagulation, which likely accounts for the improved bacteria survivability in biobanking seen with smaller volume (50uL) semi-spherical drops than typical 1.5 mL vials. By including frozen drops with drone delivery, blood coagulation outcomes may be enhanced. In-battle freezing of blood samples has the potential to reduce cell damage caused by acceleration forces during transit, resulting in tangible benefits.

5.2.4 Conclusions

In this section it has been found that semi-spherical drops are able to improve the survivability of Staphylococcus epidermidis during cryopreservation without the use of cryoprotectants over the use of standard vials. This storage method portends usage in biobanks where the reproducibility and sustainability of bacteria samples are preserved during long-term storage.

The success attained with freezing sessile drops for bacteria survivability naturally raises the possibility of using liquid marbles to do the same. A potential drawback with cryopreservation using a liquid marble instead of a sessile drop lies with the concern that the encapsulating particulate material may have negative effects on the viability of cells. While this can be investigated further, a feasibility study found that significant resources would be needed. For this reason, it was decided that the use of liquid marbles for cell cryopreservation would fall outside the scope of the project, even though the results with sessile drops, as reported in this section, indicated preliminary promise to do so.

The findings in this section have been published in J.W. Ong, Z. Song, H.A. Abid, E.S. Lin, O.W. Liew, T.W. Ng, Cryoprotectant-free preservation of bacteria using semi-spherical drops. Cryobiology. 104 (2022) 98-101.

5.3 Frozen Liquid Marble Assessment of Copper Powders for Additive Manufacturing

5.3.1 Introduction

In section 5.2, the applicability of liquid marbles for cell cryopreservation was not explored notwithstanding the promising outcomes with sessile drops. In this section, a potential use of frozen liquid marbles in additive manufacturing was investigated instead.

Laser powder bed fusion (LPBF) in additive manufacturing has distinct advantages in its capacity for freeform fabrication of complex geometrical parts while minimizing usage and wastage of materials concurrently [219, 220]. Copper has garnered wide interest in LPBF due to its corrosion resistance, high thermal and electrical conductivities [221, 222]. One of the problems in LPBF lies in the potential presence of contaminants in the feedstock which may reduce the quality of the fabricated parts [23]. While it is possible to assess contamination using sophisticated in-process monitoring methods [24], an assessment prior to use would clearly be more effective.

When a water droplet is dispensed onto a superhydrophobic surface and frozen, a conical shape is developed with a sharp tip at its apex. It is known that this shape is present due to the increase in volume when water transforms into ice as the freezing front moves from the base of the drop to its apex. More recent investigations have found that the droplet shape is also dependent on the presence of impurities in it [223].

It has been discovered that LMs made of certain types of particles can significantly alter its initial spherical shape to be more flattened when frozen [224, 225]. The mechanics behind this effect is yet to be fully understood and remains an active area of investigation.

In this section, frozen LMs were created from copper powder, as well as varying levels of copper/hydrated magnesium silicate (Talc) and copper/graphite compositions. The frozen drops were analysed for their tip and contact angles. Consequently, an assessment was made to ascertain if this approach could be developed into a method to monitor feedstock contamination of copper powder in LPBF.

5.3.2 Materials and Methods

5.3.2.1 Substrate Preparation

The substrate was created using the same method described in section 3.2.3.

5.3.2.2 Coating Particles

The particles used to create the liquid marbles were prepared from copper powder (Sigma, 266086; < 425 µm), Talc powder (Sigma, 86255; < 45 µm), and graphite powder (Sigma, 282863; < 20 µm). The copper / Talc and copper / graphite powder mixtures were prepared based on their weight percentages.

5.3.2.3 Cooler Setup

The setup to conduct the liquid marble freezing was created by combining a 68 W Peltier module (Jaycar, ZP9104) of 60mm x 60mm size and a CPU cooler (Thermaltake, CL-P039-AL12BL-A). The Peltier module was orientated with its cold side facing upwards. Aluminium shims of 1 mm thickness were used to raise the substrate to ensure that the overhanging component of the drop did not contact the Peltier module surface. A layer of thermal paste (Thermal Master HTK-002) was dispensed between the substrate, shim, and Peltier module to improve thermal conductivity.

Freezing was achieved by maintaining the substrate temperature at -2ºC as measured using a non-contact infrared probe.

5.3.2.4 Liquid Marble Creation

Each liquid marble was created by using a manual pipette to dispense 10 µL of distilled water over the hole on the substrate to create a drop. The particles were then brushed onto the drop near its apex [11]. The bristles of the cosmetic applicator brush were made from polyester and had an average radius of 500 ± 23 µm, measured using 10 fiber samples via an optical microscope (Olympus BH2). The liquid marbles were then frozen and side view images of them were recorded using a camera (Moticam, Motic) for processing. The contact angles and tip angles (if any) were determined from these images using an image analysis software (ImageJ).

5.3.3 Results and Discussion

With 10 µL of distilled water dispensed over the hole on the substrate, the typical semi-spherical shape of the drop could be seen (Fig. 75A). Measurements made from side view images of these drops found the contact angle to be 133.3º ± 2.2º. Following their freezing, the characteristic conical shape with a pointy tip at its apex was observed (Fig. 75B). In this frozen state, the tip angle was found to be 113.6º ± 3.0º while the contact angle was now 135.8º ± 1.9º. All the measurements were based on measurements using 6 different drops.

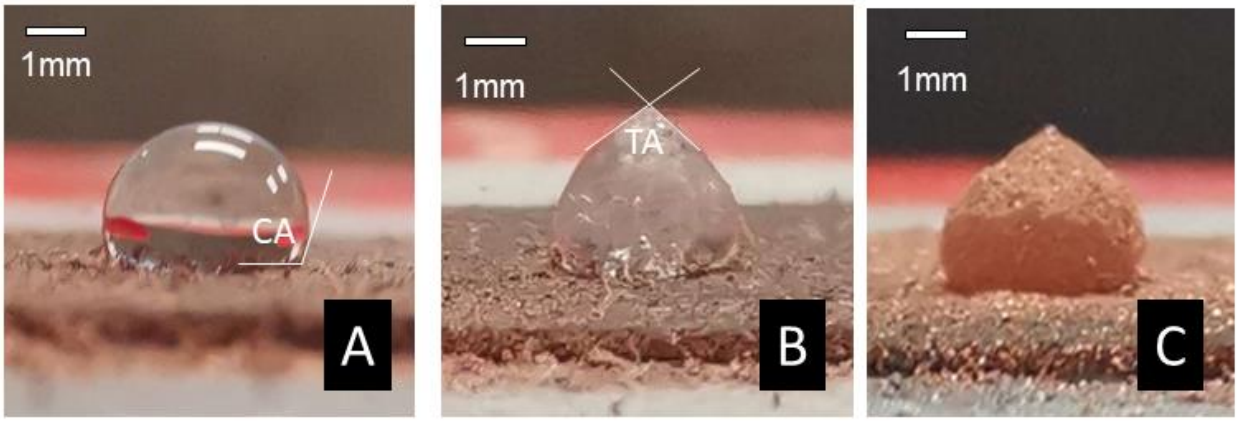

Figure 77 Side view images of a water drop (A) before and (B) after it was frozen. A conical shape with a pointy tip at its apex can be seen with the frozen drop. The frozen liquid marble created using only copper particles (C) exhibited a conical shape with a pointy tip as well. The drops are characterized by their contact angle (CA) and when frozen with a pointy tip, by the tip angle (TA) as well.

With LMs that were created using copper powder only, the conical shape with pointy tip was still visible after freezing (Fig. 77C). The tip angle was reduced to 106.7º on average, which indicated an ability of the powder to affect the late stage freezing of the apex of the drop which primarily determines the tip angle. However, the outcomes from freezing the liquid marbles made using varying compositions of copper / Talc powder (top of Fig. 78) and copper / graphite powder (bottom of Fig. 78) were different. It was found that as the composition of copper was reduced in both cases, the conical shape tip started to disappear while the shape of the drop began to assume a more flattened characteristic. In fact, no tips could be discerned when the copper composition dropped below 90%, also in both cases.

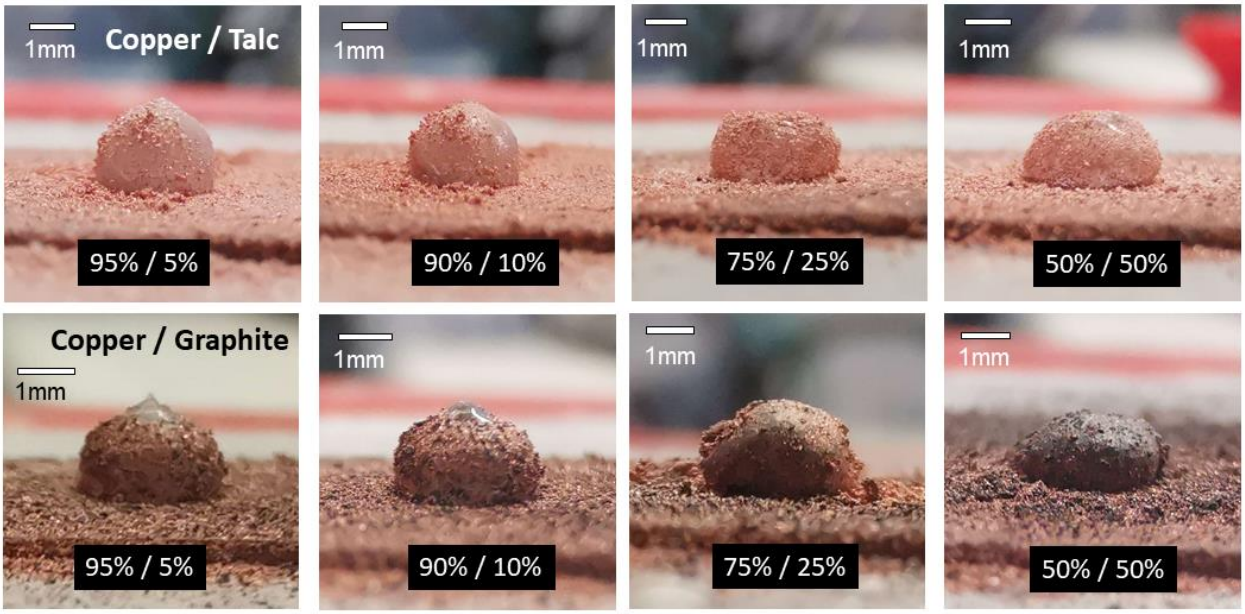

Figure 78 Side view images of the frozen liquid marbles with varying compositions of copper-Talc (top row) and copper-graphite (bottom row). It can be seen that pointy tip will diminish when comparatively lower copper compositions are used in both cases.

A graphical presentation of the tip angles determined of the frozen LMs made from 100% copper powder as well as copper versus Talc and copper versus graphite powders of varying compositions are used for a more quantitative characterization (Fig. 79). Evidently, this approach was able to distinguish the case when the LM was made from 100% copper powder and when it was made with 5% of Talc or graphite mixed in with the copper powder.

When drops begin to assume a more flattened shape, it is intuitively likely that there will be changes to their contact angles as well. Figure 80 gives the graphical depiction of the contact angles determined of the frozen LMs that were made from copper powder as well as from copper / Talc and copper / graphite powders of varying concentrations. In the case of the frozen copper / Talc LMs, there was a noticeable fall off in contact angles when the conical shape pointy tip was no longer visible (corresponding to copper composition < 90%).

However, it was not possible to use this metric to differentiate between when copper compositions of 100% and 95% were used. In the case of the frozen copper / graphite liquid marbles, the trends of change were difficult to establish due to the higher spread in the measured contact angle data. This was primarily due to the graphite particles tending to aggregate (see bottom of Fig. 78) which made the determination of contact angles using the recorded images more difficult. Overall, it can be deduced that it was not very effective to use measurements of contact angle as a means of detecting for contamination in the copper powders.

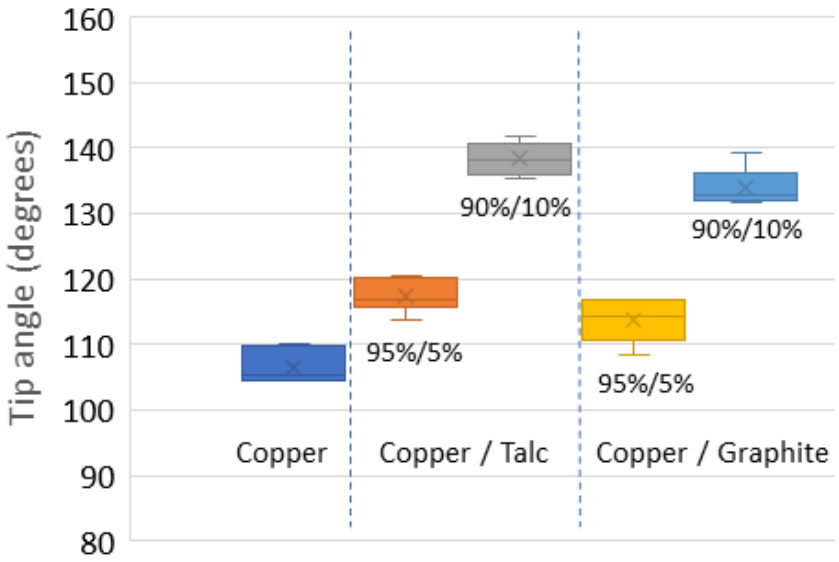

Figure 79 Box-plots of the tip angles measured for frozen liquid marbles that were made from copper powder as well as from copper / Talc and copper / graphite powders of varying compositions. The sample size in each case was 6.

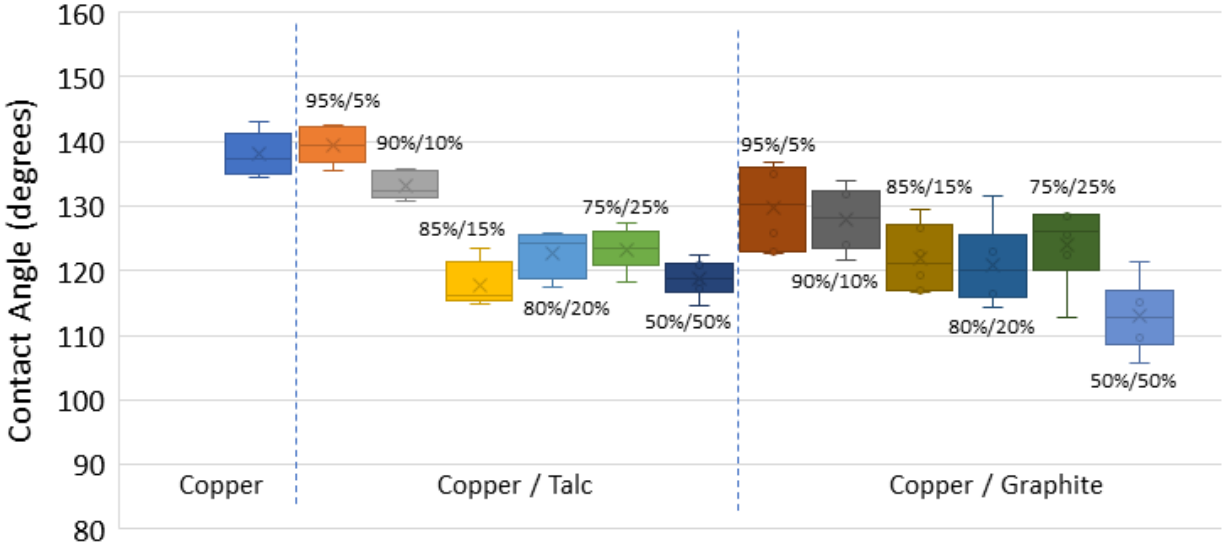

Figure 80 Box-plots of the contact angles measured for frozen liquid marbles that were made from copper powder as well as from copper / Talc and copper / graphite powders of varying compositions. The sample size in each case was 6.

Cursorily, it appeared that the ability of the copper powder to help frozen LMs maintain the conical shape pointy tips like frozen water drops may be due to its much higher thermal conductivity (~398 $Wm^{-1}K^{-1}$) than Talc powder (~10 $Wm^{-1}K^{-1}$). It should be noted however that graphite powder also possesses high thermal conductivities (~200 $Wm^{-1}K^{-1}$). It is likely then that the wetting characteristics of the copper particulates may be the primary factor responsible for this, although a more comprehensive investigation will be needed to provide this confirmation. It is also noteworthy that while the liquid marbles were created here by powder being manually brushed onto the drop, it is possible that more automated approaches will soon be developed to perform this more readily. Overall, a major advantage with this detection method lies in its simplicity and for it to be carried out inexpensively.

5.3.4 Conclusions

This section investigated the appearance of conical shape pointy tips in frozen LMs to ascertain the purity of copper powders that are meant for use in LPBF. It was found that the tip angle when 100% copper was used was clearly distinguishable from when there was 95% copper present in copper/Talc and copper/graphite powder mixtures. Monitoring the contact angle changes, however,

did not provide a similar ability to do so. In future, the findings can be applied to a fast method of detection of copper contamination in drinking water, where excess exposure has been found to cause acute copper poisoning in humans [226, 227].

The findings in this section have been submitted for publication under E.S. Lin, Z. Song, H.A. Abid, J.W. Ong, T.W. Ng, Drop freezing detection of feedstock contaminants in copper powder bed fusion additive manufacturing.

5.4 Chapter Conclusions

Liquid drops that are frozen have been widely investigated. As sessile liquid drops and liquid marbles have similar shapes, there is an impetus to gain better understanding of the latter.

In section 5.2, it was found that frozen sessile drops were found to improve the viability of bacteria sample cryopreservation over those stored in standard vials. Despite this success, there is a possibility that frozen liquid marbles may not have the same benefits. This is because of the negative effects that the encapsulating particulate material may have on the viability of cells. As significant resources would be needed to establish conclusively, it was decided that the use of liquid marbles for cell cryopreservation would not be pursued in the project, even though the results with sessile drops indicated a preliminary promise to do so.

Instead of applying frozen liquid marbles in cryopreservation, section 5.3 investigated the use of the conical shape pointy tips in frozen LMs as a basis to ascertain the purity of copper powders that are meant for use in additive manufacturing. It was found that the tip angle when 100% copper was used was clearly distinguishable from when there was 95% copper present in both copper/Talc and copper/graphite powder mixtures.

6. Overall Conclusions & Recommendations

This project has been able, to a significant level, achieve the overall objectives of
- Conducting investigations to better understand the mechanics of liquid marbles
- Devise new methods and equipment to facilitate these investigations
- Develop new applications using liquid marbles based on the investigations conducted

From the literature review conducted in Chapter 2, the fundamental basis of liquid marbles and the salient developments to date using liquid marble technology were outlined. This profoundly guided the efforts conducted to investigate the creation, content removal, and applications of liquid marbles (Chapter 3), gas bubbles in liquid marbles (Chapter 4) and liquid marble freezing (Chapter 5).

In Chapter 3, section 3.2 reported a novel method to create LMs with increased control and reduced wastage compared to current methods [6] using cosmetic brushes. The method was analysed theoretically and then subsequently proven in experiments. It was found that both LMs and JLMs could be successfully created. In section 3.3, studies using clusters of particles of various sizes transferred to the drop found that there was a positive correlation trend between particle cluster velocity and surface area coverage. This supported the model where the turning moment of the particle cluster about the centre of the drop was the cause for the downward travel. As a consequence, the conditions needed to develop stable JLMs was established and demonstrated. Section 3.4, alternatively, investigated the ability to separate wetting and non-wetting particles from an initially dry mixture by LM formation using pendant drop and sessile drop approaches. The method separated the wetting and non-wetting particles into the liquid core, which could then be withdrawn using capillary tubes for analysis.

As recommendation, the brush-on technique could be developed further by incorporating high levels of automation in the process such that arrays of LMs can be created expeditiously. This endeavour would require the strong application of instrumentation methods and likely involve the use of advanced microcontrollers, sensors and actuators. Learnings can be derived from the work of Sreejith et al. [228] that discussed the possibility of an automated on-demand LM generator with sub-microliter capability. The device that was used there applied the effect of electrohydrodynamic pulling of liquid droplets onto a hydrophobic powder bed to create LMs of desired volumes. This approach would likely result in poor volume control of the LMs. The approach used in this thesis, alternatively, would likely result in better volume control. Further work may also be done to explore if jets of particles delivered through fine nozzles can produce the LMs and JLMs in a non-contact fashion instead. If possible, this will also facilitate work that can be done to deliver a dry combination of the wetting and non-wetting types to the liquid drop so as to conduct the separation operation as described in section 3.4 as a LM.

In Chapter 4, section 4.2 reported a new instrumentation for precise liquid delivery. This was adopted in section 4.3 to generate slow bubbles with specified volumes. It was found that discrete bubbles delivered with a flowrate of 0.57 mL/s (less than the 1 mL/s used to define slow) was possible. Due to the image distortion effect, an alternative image binarization technique using camera recordings with lower resolutions (320 x 240 pixels) and typical 30 frames per second imagery was proposed. It was found able to establish the flowrate by counting bubbles or determining the duration between bubbles. Based on the methods developed in sections 4.2 and 4.3, a singular gas bubble injected into a LM was investigated in section 4.4. The apex of the shell was shown to be cleared and through a theoretical analysis, it was found that the physics behind this lied with the particles tending to eschew the thin film region of the bubble due to unfavourable energetic conditions, allowing for the transient opening of the particle shell. Finally, in section 4.5, it was shown that the on-demand generation of hydrogen and oxygen bubble via electrodes was possible by applying less than 10V to the overhanging component of the LM. Gas bubbles were able to travel to the overhead component given proper electrode alignment. Aeration was possible with minimal contamination of the overhead component.

As recommendation, further work could be conducted to better control the particle clearing at the apex of LMs as illustrated in section 4.4. Following the injection of air into the LM, there is currently only a short period before the bubble eventually ruptures. It is plausible, with better gaseous control techniques introduced, for the bubble to remain inside the LM for a longer period of time so that more elaborate processes could be incorporated. Nikoilov et. al [229], for instance, has developed a piezoelectric-acoustic technique to monitor the bubble rupture time and frequency of oscillation. With the appropriate modification, this could potentially be applied in future to determine the rupture time of an air bubble residing in a LM. In fact, if the gas bubble should ideally be drawn back into the nozzle, thereby preventing the rupture process altogether, it could prevent any inadvertent liquid loss from the LM from occurring. In developing further on the technique described in section 4.4, the location of live bacteria at the overhead section of the LM could be used to ascertain the level of aeration of gases that promoted their growth to be investigated. A recent study conducted by Couvert et. al [230] has modelled the effect that oxygen concentration would have on bacterial growth rates. Using those findings as a guide, it ought to be possible to conduct this potential future study under a greater level of confidence. In the same vein, this could also be used to determine the level of aeration of gases that would cause their mortality to be investigated. The influence of bubbles breaking-up into smaller sizes to spread over the apex of the droplet could also be interrogated at the same time.

In Chapter 5, section 5.2 found that frozen sessile drops were able to improve the viability of bacteria sample cryopreservation over those stored in standard vials. Section 5.3 investigated the use of the conical shape pointy tips in frozen LMs as a basis to detect contamination in copper powders in applications of additive manufacturing. It found that the tip angle, when 100% copper was used, was clearly distinguishable from when there was 95% copper present in copper/Talc and copper/graphite powder mixtures.

As recommendation, further work could be conducted to ascertain if frozen LMs would have the same benefits as frozen sessile drops in improving the cryopreservation of bacteria over standard vials. In pursuing this, it will be necessary to establish if the particles themselves can be tailored to have limited or even beneficial effects improving the viability of cells. It is also recommended that further work be done to establish if the ability of LMs to prevent the frozen pointy end of drops from forming is due to the wetting characteristics of the particles. This phenomenon has been extensively researched [101, 231-233], however this issue has not been conclusively resolved to date.

7. References

[1] R. Vadivelu, N. Kashaninejadand, and N.-T. Nguyen, "Liquid marble with embedded hydrogel: A versatile microbioreactor for cell biology applications," in *22nd International Conference on Miniaturized Systems for Chemistry and Life Sciences, MicroTAS 2018, November 11, 2018 - November 15, 2018*, Kaohsiung, Taiwan, 2018, vol. 3: Chemical and Biological Microsystems Society, in 22nd International Conference on Miniaturized Systems for Chemistry and Life Sciences, MicroTAS 2018, pp. 1492-1495.

[2] C. H. Ooi, E. Bormashenko, A. V. Nguyen, G. M. Evans, D. V. Dao, and N.-T. Nguyen, "Evaporation of Ethanol–Water Binary Mixture Sessile Liquid Marbles," *Langmuir,* vol. 32, no. 24, pp. 6097-6104, 2016/06/21 2016, doi: 10.1021/acs.langmuir.6b01272.

[3] Y. Chi *et al.*, "Insights into the Interfacial Contact and Charge Transport of Gas-Sensing Liquid Metal Marbles," *ACS Applied Materials and Interfaces,* vol. 14, no. 26, pp. 30112-30123, 2022, doi: 10.1021/acsami.2c06908.

[4] Z. Zhao, Y. Zhang, L. Ren, B. Xiang, and J. Li, "Facile preparation of colorful liquid marbles and liquid marbles used in water pollutant detection," *Journal of Adhesion Science and Technology,* vol. 31, no. 10, pp. 1125-1132, 2017, doi: 10.1080/01694243.2016.1246021.

[5] C. H. Ooi *et al.*, "Liquid marble-based digital microfluidics-fundamentals and applications," *Lab on a Chip,* vol. 21, no. 7, pp. 1199-1216, 2021, doi: 10.1039/d0lc01290d.

[6] P. Aussillous and D. Quéré, "Liquid marbles," *Nature,* vol. 411, no. 6840, pp. 924-927, 2001/06/01 2001, doi: 10.1038/35082026.

[7] E. Bormashenko, R. Pogreb, R. Balter, O. Gendelman, and D. Aurbach, "Composite non-stick droplets and their actuation with electric field," *Applied Physics Letters,* vol. 100, no. 15, p. 151601, 2012/04/09 2012, doi: 10.1063/1.3702568.

[8] J. O. Castro, B. M. Neves, A. R. Rezk, N. Eshtiaghi, and L. Y. Yeo, "Continuous Production of Janus and Composite Liquid Marbles with Tunable Coverage," *ACS Applied Materials & Interfaces,* vol. 8, no. 28, pp. 17751-17756, 2016/07/20 2016, doi: 10.1021/acsami.6b05321.

[9] A. Tyowua, J. Mooney, and B. Binks, "Janus liquid marbles containing both oil and water stabilised by silica or sericite particles," *Colloids and Surfaces A: Physicochemical and Engineering Aspects,* vol. 560, 09/01 2018, doi: 10.1016/j.colsurfa.2018.09.084.

[10] B. S. Lekshmi, A. S. Yadav, P. Ranganathan, and S. N. Varanakkottu, "Simple and Continuous Fabrication of Janus Liquid Marbles with Tunable Particle Coverage Based on Controlled Droplet Impact," *Langmuir,* vol. 36, no. 50, pp. 15396-15402, 2020/12/22 2020, doi: 10.1021/acs.langmuir.0c02988.

[11] E. S. Lin, Z. Song, J. W. Ong, H. A. Abid, O. W. Liew, and T. W. Ng, "Brushed creation of liquid marbles," *PeerJ Materials Science,* vol. 4, p. e24, 2022/10/12 2022, doi: 10.7717/peerj-matsci.24.

[12] T. T. Y. Tan *et al.*, "Photoresponsive Liquid Marbles and Dry Water," *Langmuir,* vol. 30, no. 12, pp. 3448-3454, 2014/04/01 2014, doi: 10.1021/la500646r.

[13] D. Zang, J. Li, Z. Chen, Z. Zhai, X. Geng, and B. P. Binks, "Switchable Opening and Closing of a Liquid Marble via Ultrasonic Levitation," *Langmuir,* vol. 31, no. 42, pp. 11502-11507, 2015/10/27 2015, doi: 10.1021/acs.langmuir.5b02917.

[14] C. Wang and Y. He, "Timed disintegrating of the liquid marbles containing triton X-100," *Colloids and Surfaces A: Physicochemical and Engineering Aspects,* vol. 558, 09/01 2018, doi: 10.1016/j.colsurfa.2018.09.005.

[15] J. McCraney, M. Weislogel, and P. Steen, "The draining of capillary liquids from containers with interior corners aboard the ISS," *npj Microgravity,* vol. 7, no. 1, p. 45, 2021/11/11 2021, doi: 10.1038/s41526-021-00173-5.

[16] H.-m. Choi, K.-B. Lee, and K.-A. Park, "Measurement of gas flowrate by using a heat pulse," *Flow Measurement and Instrumentation,* vol. 2, no. 3, pp. 188-192, 1991/07/01/ 1991, doi: https://doi.org/10.1016/0955-5986(91)90032-M.

[17] C. Hua and Y. Geng, "Wet gas metering technique based on slotted orifice and swirlmeter in series," *Flow Measurement and Instrumentation,* vol. 30, pp. 138-143, 2013/04/01/ 2013, doi: https://doi.org/10.1016/j.flowmeasinst.2013.02.001.

[18] W. Kang, S.-H. Lee, S.-J. Lee, Y.-C. Ha, and S.-S. Jung, "Effect of ultrasonic noise generated by pressure control valves on ultrasonic gas flowmeters," *Flow Measurement and Instrumentation,* vol. 60, pp. 95-104, 2018/04/01/ 2018, doi: https://doi.org/10.1016/j.flowmeasinst.2018.02.023.
[19] E. S. Lin *et al.*, "Liquid marble particle wetting separation," *Colloid and Interface Science Communications,* vol. 35, p. 100237, 2020/03/01/ 2020, doi: https://doi.org/10.1016/j.colcom.2020.100237.
[20] D. C. K. Chung *et al.*, "Drops on a Superhydrophobic Hole Hanging On under Evaporation," *ACS Omega,* vol. 2, no. 9, pp. 6211-6222, 2017/09/30 2017, doi: 10.1021/acsomega.7b01114.
[21] D. C. K. Chung, M. Katariya, A. A. Ahmad Zahidi, C. Y. Lau, O. W. Liew, and T. W. Ng, "Antibody drop based handling with near-superhydrophobic mesh substrates overcomes condensation sticking," *Materials Science and Engineering: C,* vol. 96, pp. 599-605, 2019/03/01/ 2019, doi: https://doi.org/10.1016/j.msec.2018.11.040.
[22] L. Bircher, A. Geirnaert, F. Hammes, C. Lacroix, and C. Schwab, "Effect of cryopreservation and lyophilization on viability and growth of strict anaerobic human gut microbes," (in eng), *Microb Biotechnol,* vol. 11, no. 4, pp. 721-733, Jul 2018, doi: 10.1111/1751-7915.13265.
[23] M. Horn *et al.*, "Influence of metal powder cross-contaminations on part quality in Laser Powder Bed Fusion: copper alloy particles in maraging steel feedstock," *Procedia CIRP,* vol. 94, pp. 167-172, 2020/01/01/ 2020, doi: https://doi.org/10.1016/j.procir.2020.09.032.
[24] M. Montazeri, R. Yavari, P. Rao, and P. Boulware, "In-Process Monitoring of Material Cross-Contamination Defects in Laser Powder Bed Fusion," *Journal of Manufacturing Science and Engineering,* vol. 140, no. 11, 2018, doi: 10.1115/1.4040543.
[25] Y. Z. Hu and T. B. Ma, "3.12 - Tribology of Nanostructured Surfaces," in *Comprehensive Nanoscience and Technology*, D. L. Andrews, G. D. Scholes, and G. P. Wiederrecht Eds. Amsterdam: Academic Press, 2011, pp. 383-418.
[26] C. Luo, M. Mrinal, and X. Wang, "Self-propulsion of Leidenfrost Drops between Non-Parallel Structures," *Scientific Reports,* vol. 7, p. 12018, 09/20 2017, doi: 10.1038/s41598-017-12279-6.
[27] C. Aberle, M. Lewis, G. Yu, N. Lei, and J. Xu, "Liquid marbles as thermally robust droplets: coating-assisted Leidenfrost-like effect," *Soft Matter,* 10.1039/C1SM06480K vol. 7, no. 24, pp. 11314-11318, 2011, doi: 10.1039/C1SM06480K.
[28] K. Liyanaarachchi, P. Ireland, G. Webber, and K. Galvin, "Electrostatic formation of liquid marbles and agglomerates," *Applied Physics Letters,* vol. 103, 08/01 2013, doi: 10.1063/1.4817586.
[29] A. R. Akande and J. Lowell, "Contact electrification of polymers by metals," *Journal of Electrostatics,* vol. 16, no. 2, pp. 147-156, 1985/05/01/ 1985, doi: https://doi.org/10.1016/0304-3886(85)90038-5.
[30] P. Aussillous and D. Quéré, "Liquid marbles," (in eng), *Nature,* vol. 411, no. 6840, pp. 924-7, Jun 21 2001, doi: 10.1038/35082026.
[31] E. Bormashenko, Y. Bormashenko, R. Pogreb, and O. Gendelman, "Janus Droplets: Liquid Marbles Coated with Dielectric/Semiconductor Particles," *Langmuir,* vol. 27, no. 1, pp. 7-10, 2011/01/04 2011, doi: 10.1021/la103653p.
[32] Y. Zhao, J. Fang, H. Wang, X. Wang, and T. Lin, "Magnetic Liquid Marbles: Manipulation of Liquid Droplets Using Highly Hydrophobic Fe3O4 Nanoparticles," *Advanced materials (Deerfield Beach, Fla.),* vol. 22, pp. 707-10, 02/09 2010, doi: 10.1002/adma.200902512.
[33] X. Lin *et al.*, "Superhydrophobic magnetic poly(DOPAm-co-PFOEA)/Fe3O4/cellulose microspheres for stable liquid marbles," *Chem. Commun.,* vol. 52, 12/17 2015, doi: 10.1039/C5CC08842A.
[34] X. Lin *et al.*, "Superhydrophobic magnetic poly(DOPAm-co-PFOEA)/Fe3O4/cellulose microspheres for stable liquid marbles," *Chemical Communications,* 10.1039/C5CC08842A vol. 52, no. 9, pp. 1895-1898, 2016, doi: 10.1039/C5CC08842A.
[35] R. K. Vadivelu, H. Kamble, A. Munaz, and N.-T. Nguyen, "Liquid Marble as Bioreactor for Engineering Three-Dimensional Toroid Tissues," *Scientific Reports,* vol. 7, no. 1, p. 12388, 2017/09/28 2017, doi: 10.1038/s41598-017-12636-5.

[36] Y. Zhao, Z. Xu, H. Niu, X. Wang, and T. Lin, "Magnetic Liquid Marbles: Toward “Lab in a Droplet”," *Advanced Functional Materials,* https://doi.org/10.1002/adfm.201403051 vol. 25, no. 3, pp. 437-444, 2015/01/01 2015, doi: https://doi.org/10.1002/adfm.201403051.
[37] C. H. Ooi *et al.*, "Liquid marble-based digital microfluidics – fundamentals and applications," *Lab on a Chip,* 10.1039/D0LC01290D vol. 21, no. 7, pp. 1199-1216, 2021, doi: 10.1039/D0LC01290D.
[38] A. T. Tyowua, F. Ahor, S. G. Yiase, and B. P. Binks, "Liquid marbles as microreactors for qualitative and quantitative inorganic analyses," *SN Applied Sciences,* vol. 2, no. 3, p. 345, 2020/02/05 2020, doi: 10.1007/s42452-020-2174-9.
[39] V. Ortseifen, M. Viefhues, L. Wobbe, and A. Grünberger, "Microfluidics for Biotechnology: Bridging Gaps to Foster Microfluidic Applications," (in English), *Frontiers in Bioengineering and Biotechnology,* Review vol. 8, 2020-November-13 2020, doi: 10.3389/fbioe.2020.589074.
[40] G. Minas, "Lab-on-a-Chip Devices for Chemical Analysis," in *Encyclopedia of Microfluidics and Nanofluidics*, D. Li Ed. Boston, MA: Springer US, 2008, pp. 910-927.
[41] Y. Zhang, S. Ge, and J. Yu, "Chemical and biochemical analysis on lab-on-a-chip devices fabricated using three-dimensional printing," *TrAC Trends in Analytical Chemistry,* vol. 85, 09/14 2016, doi: 10.1016/j.trac.2016.09.008.
[42] J. Tian, T. Arbatan, X. Li, and W. Shen, "Liquid marble for gas sensing," *Chemical Communications,* 10.1039/C001317J vol. 46, no. 26, pp. 4734-4736, 2010, doi: 10.1039/C001317J.
[43] T. Arbatan, A. Al-Abboodi, F. Sarvi, P. P. Y. Chan, and W. Shen, "Tumor Inside a Pearl Drop," *Advanced Healthcare Materials,* https://doi.org/10.1002/adhm.201200050 vol. 1, no. 4, pp. 467-469, 2012/07/01 2012, doi: https://doi.org/10.1002/adhm.201200050.
[44] F. Sarvi, T. Arbatan, P. P. Y. Chan, and W. Shen, "A novel technique for the formation of embryoid bodies inside liquid marbles," *RSC Advances,* 10.1039/C3RA40364E vol. 3, no. 34, pp. 14501-14508, 2013, doi: 10.1039/C3RA40364E.
[45] R. K. Vadivelu *et al.*, "Generation of three-dimensional multiple spheroid model of olfactory ensheathing cells using floating liquid marbles," *Scientific Reports,* vol. 5, no. 1, p. 15083, 2015/10/14 2015, doi: 10.1038/srep15083.
[46] S. Ledda, A. Idda, J. Kelly, F. Ariu, L. Bogliolo, and D. Bebbere, *IN VITRO MATURATION OF SHEEP OOCYTES WITH LIQUID MARBLE MICRO-BIOREACTOR*. 2015.
[47] J. Tian, N. Fu, X. D. Chen, and W. Shen, "Respirable liquid marble for the cultivation of microorganisms," *Colloids and Surfaces B: Biointerfaces,* vol. 106, pp. 187-190, 2013/06/01/ 2013, doi: https://doi.org/10.1016/j.colsurfb.2013.01.016.
[48] S. Ikehara, "Grand challenges in stem cell treatments," (in eng), *Front Cell Dev Biol,* vol. 1, p. 2, 2013, doi: 10.3389/fcell.2013.00002.
[49] F. Sarvi *et al.*, "Cardiogenesis of embryonic stem cells with liquid marble micro-bioreactor," (in eng), *Adv Healthc Mater,* vol. 4, no. 1, pp. 77-86, Jan 7 2015, doi: 10.1002/adhm.201400138.
[50] A. Oikonomopoulos, T. Kitani, and J. C. Wu, "Pluripotent Stem Cell-Derived Cardiomyocytes as a Platform for Cell Therapy Applications: Progress and Hurdles for Clinical Translation," (in eng), *Mol Ther,* vol. 26, no. 7, pp. 1624-1634, Jul 5 2018, doi: 10.1016/j.ymthe.2018.02.026.
[51] N. Abi-Gerges, P. E. Miller, and A. Ghetti, "Human Heart Cardiomyocytes in Drug Discovery and Research: New Opportunities in Translational Sciences," (in eng), *Curr Pharm Biotechnol,* vol. 21, no. 9, pp. 787-806, 2020, doi: 10.2174/1389201021666191210142023.
[52] A. J. S. Ribeiro *et al.*, "Considerations for an In Vitro, Cell-Based Testing Platform for Detection of Drug-Induced Inotropic Effects in Early Drug Development. Part 2: Designing and Fabricating Microsystems for Assaying Cardiac Contractility With Physiological Relevance Using Human iPSC-Cardiomyocytes," (in eng), *Front Pharmacol,* vol. 10, p. 934, 2019, doi: 10.3389/fphar.2019.00934.
[53] R. Vadivelu *et al.*, "Generation of three-dimensional multiple spheroid model of olfactory ensheathing cells using floating liquid marbles," *Scientific Reports,* vol. 5, 10/14 2015, doi: 10.1038/srep15083.

[54] D. Bebbere, S. M. Nieddu, F. Ariu, D. Piras, and S. Ledda, "3D Liquid Marble Microbioreactors Support In Vitro Maturation of Prepubertal Ovine Oocytes and Affect Expression of Oocyte-Specific Factors," (in eng), *Biology (Basel),* vol. 10, no. 11, Oct 25 2021, doi: 10.3390/biology10111101.
[55] S. Ledda, A. Idda, J. Kelly, F. Ariu, L. Bogliolo, and D. Bebbere, "A novel technique for in vitro maturation of sheep oocytes in a liquid marble microbioreactor," *Journal of Assisted Reproduction and Genetics,* 02/06 2016.
[56] K. R. Sreejith, P. Singha, N.-K. Nguyen, C. H. Ooi, D. V. Dao, and N.-T. Nguyen, "Noninvasive refilling of liquid marbles with water for microfluidic applications," *Applied Physics Letters,* vol. 120, no. 6, p. 064102, 2022/02/07 2022, doi: 10.1063/5.0074887.
[57] E. Bormashenko and A. Musin, "Revealing of water surface pollution with liquid marbles," *Applied Surface Science - APPL SURF SCI,* vol. 255, pp. 6429-6431, 04/01 2009, doi: 10.1016/j.apsusc.2009.02.027.
[58] D. Bebbere, S. Nieddu, F. Ariu, D. Piras, and S. Ledda, "3D Liquid Marble Microbioreactors Support In Vitro Maturation of Prepubertal Ovine Oocytes and Affect Expression of Oocyte-Specific Factors," *Biology,* vol. 10, p. 1101, 10/25 2021, doi: 10.3390/biology10111101.
[59] T. Arbatan, L. Li, J. Tian, and W. Shen, "Liquid Marbles as Micro-bioreactors for Rapid Blood Typing," *Advanced Healthcare Materials,* https://doi.org/10.1002/adhm.201100016 vol. 1, no. 1, pp. 80-83, 2012/01/11 2012, doi: https://doi.org/10.1002/adhm.201100016.
[60] K. Landsteiner, "On Agglutination of Normal Human Blood," *Transfusion,* https://doi.org/10.1111/j.1537-2995.1961.tb00005.x vol. 1, no. 1, pp. 5-8, 1961/01/02 1961, doi: https://doi.org/10.1111/j.1537-2995.1961.tb00005.x.
[61] D. S. Kim, S. H. Lee, C. H. Ahn, J. Y. Lee, and T. H. Kwon, "Disposable integrated microfluidic biochip for blood typing by plastic microinjection moulding," *Lab on a Chip,* 10.1039/B516495H vol. 6, no. 6, pp. 794-802, 2006, doi: 10.1039/B516495H.
[62] N. M. Oliveira, C. R. Correia, R. L. Reis, and J. F. Mano, "Liquid Marbles for High-Throughput Biological Screening of Anchorage-Dependent Cells," *Advanced Healthcare Materials,* https://doi.org/10.1002/adhm.201400310 vol. 4, no. 2, pp. 264-270, 2015/01/01 2015, doi: https://doi.org/10.1002/adhm.201400310.
[63] C. R. Correia, P. Sher, R. L. Reis, and J. F. Mano, "Liquified chitosan–alginate multilayer capsules incorporating poly(l-lactic acid) microparticles as cell carriers," *Soft Matter,* 10.1039/C2SM26784E vol. 9, no. 7, pp. 2125-2130, 2013, doi: 10.1039/C2SM26784E.
[64] F. A. Almeida *et al.*, "Interfaces in Nano-/Microcrystalline Multigrade CVD Diamond Coatings," *ACS Applied Materials & Interfaces,* vol. 5, no. 22, pp. 11725-11729, 2013/11/27 2013, doi: 10.1021/am403401s.
[65] W. Y. Ho, S. K. Yeap, C. L. Ho, R. A. Rahim, and N. B. Alitheen, "Development of Multicellular Tumor Spheroid (MCTS) Culture from Breast Cancer Cell and a High Throughput Screening Method Using the MTT Assay," *PLOS ONE,* vol. 7, no. 9, p. e44640, 2012, doi: 10.1371/journal.pone.0044640.
[66] M. C. Serrano, S. Nardecchia, M. C. Gutiérrez, M. L. Ferrer, and F. del Monte, "Mammalian cell cryopreservation by using liquid marbles," (in eng), *ACS Appl Mater Interfaces,* vol. 7, no. 6, pp. 3854-60, Feb 18 2015, doi: 10.1021/acsami.5b00072.
[67] A. Lawson, H. Ahmad, and A. Sambanis, "Cytotoxicity effects of cryoprotectants as single-component and cocktail vitrification solutions," (in eng), *Cryobiology,* vol. 62, no. 2, pp. 115-22, Apr 2011, doi: 10.1016/j.cryobiol.2011.01.012.
[68] L. Bahari, A. Bein, V. Yashunsky, and I. Braslavsky, "Directional freezing for the cryopreservation of adherent mammalian cells on a substrate," (in eng), *PLoS One,* vol. 13, no. 2, p. e0192265, 2018, doi: 10.1371/journal.pone.0192265.
[69] N.-K. Nguyen *et al.*, "Liquid Marbles as Miniature Reactors for Chemical and Biological Applications," *Processes*, vol. 8, no. 7, doi: 10.3390/pr8070793.
[70] M. Callies and D. Quéré, "On water repellency," *Soft Matter,* 10.1039/B501657F vol. 1, no. 1, pp. 55-61, 2005, doi: 10.1039/B501657F.
[71] D. Vollath, F. D. Fischer, and D. Holec, "Surface energy of nanoparticles - influence of particle size and structure," (in eng), *Beilstein J Nanotechnol,* vol. 9, pp. 2265-2276, 2018, doi: 10.3762/bjnano.9.211.

[72] P. McEleney, G. M. Walker, I. A. Larmour, and S. E. J. Bell, "Liquid marble formation using hydrophobic powders," *Chemical Engineering Journal,* vol. 147, no. 2, pp. 373-382, 2009/04/15/ 2009, doi: https://doi.org/10.1016/j.cej.2008.11.026.
[73] M. Filella, V. Chanudet, S. Philippo, and F. Quentel, "Particle size and mineralogical composition of inorganic colloids in waters draining the adit of an abandoned mine, Goesdorf, Luxembourg," *Applied Geochemistry,* vol. 24, pp. 52-61, 01/31 2009, doi: 10.1016/j.apgeochem.2008.11.010.
[74] K. Iwuozor, "Properties and Uses of Colloids: A Review," *Colloid and Surface Science,* vol. 4, pp. 24-28, 01/01 2019, doi: 10.11648/j.css.20190402.12.
[75] E. Sowade, T. Blaudeck, and R. R. Baumann, "Inkjet Printing of Colloidal Nanospheres: Engineering the Evaporation-Driven Self-Assembly Process to Form Defined Layer Morphologies," *Nanoscale Research Letters,* vol. 10, no. 1, p. 362, 2015/09/16 2015, doi: 10.1186/s11671-015-1065-2.
[76] B. Fleury, G. Dantelle, S. Darbe, J. Boilot, and T. Gacoin, "Transparent Coatings Made from Spray Deposited Colloidal Suspensions," *Langmuir : the ACS journal of surfaces and colloids,* vol. 28, pp. 7639-45, 04/24 2012, doi: 10.1021/la300872m.
[77] S. J. Hemington-Gorse, "Colloid or crystalloid for resuscitation of major burns," (in eng), *J Wound Care,* vol. 14, no. 6, pp. 256-8, Jun 2005, doi: 10.12968/jowc.2005.14.6.26786.
[78] R. D. Deegan, O. Bakajin, T. F. Dupont, G. Huber, S. R. Nagel, and T. A. Witten, "Capillary flow as the cause of ring stains from dried liquid drops," *Nature,* vol. 389, no. 6653, pp. 827-829, 1997/10/01 1997, doi: 10.1038/39827.
[79] R. Chen, L. Zhang, D. Zang, and W. Shen, "Blood drop patterns: Formation and applications," *Advances in Colloid and Interface Science,* vol. 231, pp. 1-14, 2016/05/01/ 2016, doi: https://doi.org/10.1016/j.cis.2016.01.008.
[80] V. Poulichet, M. Morel, S. Rudiuk, and D. Baigl, "Liquid-liquid coffee-ring effect," *Journal of Colloid and Interface Science,* vol. 573, pp. 370-375, 2020/08/01/ 2020, doi: https://doi.org/10.1016/j.jcis.2020.03.094.
[81] H. Hu and R. G. Larson, "Analysis of the Effects of Marangoni Stresses on the Microflow in an Evaporating Sessile Droplet," *Langmuir,* vol. 21, no. 9, pp. 3972-3980, 2005/04/01 2005, doi: 10.1021/la0475270.
[82] H. Hu and R. G. Larson, "Marangoni Effect Reverses Coffee-Ring Depositions," *The Journal of Physical Chemistry B,* vol. 110, no. 14, pp. 7090-7094, 2006/04/01 2006, doi: 10.1021/jp0609232.
[83] G. Iannacchione and A. Pal, "Bio-colloidal Drying Droplets: Current Trends and Future Perspectives on Image Processing Applications," 08/05 2021, doi: 10.20935/AL2661.
[84] M. Pucetaite, M. Velicka, J. Pilipavicius, A. Beganskiene, J. Ceponkus, and V. Sablinskas, "Uric acid detection by means of SERS spectroscopy on dried Ag colloidal drops," *Journal of Raman Spectroscopy,* https://doi.org/10.1002/jrs.4875 vol. 47, no. 6, pp. 681-686, 2016/06/01 2016, doi: https://doi.org/10.1002/jrs.4875.
[85] H. Li *et al.*, "Preventing the coffee-ring effect and aggregate sedimentation by in situ gelation of monodisperse materials," *Chemical Science,* 10.1039/C8SC03302A vol. 9, no. 39, pp. 7596-7605, 2018, doi: 10.1039/C8SC03302A.
[86] Y. Xie, Y. Liang, D. Chen, X. Wu, L. Dai, and Q. Liu, "Vortical superlattices in a gold nanorods' self-assembled monolayer," *Nanoscale,* 10.1039/C3NR05992H vol. 6, no. 6, pp. 3064-3068, 2014, doi: 10.1039/C3NR05992H.
[87] L.-Q. Lu, Y. Zheng, W.-G. Qu, H.-Q. Yu, and A.-W. Xu, "Hydrophobic Teflon films as concentrators for single-molecule SERS detection," *Journal of Materials Chemistry,* 10.1039/C2JM33955B vol. 22, no. 39, pp. 20986-20990, 2012, doi: 10.1039/C2JM33955B.
[88] T. A. H. Nguyen, M. A. Hampton, and A. V. Nguyen, "Evaporation of Nanoparticle Droplets on Smooth Hydrophobic Surfaces: The Inner Coffee Ring Deposits," *The Journal of Physical Chemistry C,* vol. 117, no. 9, pp. 4707-4716, 2013/03/07 2013, doi: 10.1021/jp3126939.
[89] X. Lin, H. Lee, Y. Hwang, and R. Radermacher, "A review of recent development in variable refrigerant flow systems," *Science and Technology for the Built Environment,* vol. 21, no. 7, pp. 917-933, 2015/10/03 2015, doi: 10.1080/23744731.2015.1071987.
[90] X. Zhang, X. Wu, J. Min, and X. Liu, "Modelling of sessile water droplet shape evolution during freezing with consideration of supercooling effect," *Applied Thermal Engineering,*

vol. 125, pp. 644-651, 2017/10/01/ 2017, doi: https://doi.org/10.1016/j.applthermaleng.2017.07.017.
[91] M. Song, C. Dang, T. Higashi, and E. Hihara, "Review of experimental data associated with the solidification characteristics of water droplets on a cold plate surface at the early frosting stage," *Energy and Buildings,* vol. 223, p. 110103, 2020/09/15/ 2020, doi: https://doi.org/10.1016/j.enbuild.2020.110103.
[92] T. M. Schutzius *et al.*, "Physics of Icing and Rational Design of Surfaces with Extraordinary Icephobicity," *Langmuir,* vol. 31, no. 17, pp. 4807-4821, 2015/05/05 2015, doi: 10.1021/la502586a.
[93] C. Gurganus, A. B. Kostinski, and R. A. Shaw, "High-Speed Imaging of Freezing Drops: Still No Preference for the Contact Line," *The Journal of Physical Chemistry C,* vol. 117, no. 12, pp. 6195-6200, 2013/03/28 2013, doi: 10.1021/jp311832d.
[94] T. Hikima, M. Hanaya, and M. Oguni, "Discovery of a potentially homogeneous-nucleation-based crystallization around the glass transition temperature in salol," *Solid State Communications,* vol. 93, no. 8, pp. 713-717, 1995/02/01/ 1995, doi: https://doi.org/10.1016/0038-1098(94)00754-3.
[95] D. Pan, Q. Wan, and G. Galli, "The refractive index and electronic gap of water and ice increase with increasing pressure," *Nature Communications,* vol. 5, no. 1, p. 3919, 2014/05/27 2014, doi: 10.1038/ncomms4919.
[96] "The behavior of water drops at terminal velocity in air," *Eos, Transactions American Geophysical Union,* https://doi.org/10.1029/TR031i006p00836 vol. 31, no. 6, pp. 836-842, 1950/12/01 1950, doi: https://doi.org/10.1029/TR031i006p00836.
[97] M. Lu, M. Song, X. Pang, C. Dang, and L. Zhang, "Modeling study on sessile water droplet during freezing with the consideration of gravity, supercooling, and volume expansion effects," *International Journal of Multiphase Flow,* vol. 147, p. 103909, 2022/02/01/ 2022, doi: https://doi.org/10.1016/j.ijmultiphaseflow.2021.103909.
[98] Y. Yao, C. Li, Z. Tao, and R. Yang, *Numerical Simulation of Water Droplet Freezing Process on Cold Surface*. 2017, p. V008T10A072.
[99] X. Liu and X. Zhang, *Freezing simulation of static supercooled water droplet on a cold surface*. 2017.
[100] S. Chang, H. Qi, S. Zhou, and Y. Yang, "Experimental study on freezing characteristics of water droplets on cold surfaces," *International Journal of Heat and Mass Transfer,* vol. 194, p. 123108, 2022/09/15/ 2022, doi: https://doi.org/10.1016/j.ijheatmasstransfer.2022.123108.
[101] J. Snoeijer and P. Brunet, "Pointy ice-drops: How water freezes into a singular shape," *American Journal of Physics,* vol. 80, pp. 764-771, 09/01 2012, doi: 10.1119/1.4726201.
[102] J. Wang, Z. Liu, Y. Gou, X. Zhang, and S. Cheng, "Deformation of freezing water droplets on a cold copper surface," *Science in China Series E: Technological Sciences,* vol. 49, no. 5, pp. 590-600, 2006/10/01 2006, doi: 10.1007/s11431-006-2017-y.
[103] M. Nauenberg, "Comment on “Pointy ice-drops: How water freezes into a singular shape” [Am. J. Phys. 80, 764–771 (2012)]," *American Journal of Physics,* vol. 81, no. 2, pp. 150-151, 2013/02/01 2013, doi: 10.1119/1.4765366.
[104] S. Peng, Y. Hu, J. Huang, and M. Song, "Surface free energy analysis for stable supercooling of sodium thiosulfate pentahydrate with microcosmic-visualized methods," *Solar Energy Materials and Solar Cells,* vol. 208, p. 110390, 2020/05/01/ 2020, doi: https://doi.org/10.1016/j.solmat.2019.110390.
[105] Y. Hao, Y. Zhang, and A. Prosperetti, "Mechanics of gas-vapor bubbles," *Physical Review Fluids,* vol. 2, no. 3, p. 034303, 03/23/ 2017, doi: 10.1103/PhysRevFluids.2.034303.
[106] Y. Hao and A. Prosperetti, "The dynamics of vapor bubbles in acoustic pressure fields," *Physics of Fluids,* vol. 11, no. 8, pp. 2008-2019, 1999/08/01 1999, doi: 10.1063/1.870064.
[107] M. E. Zaytsev *et al.*, "Gas–Vapor Interplay in Plasmonic Bubble Shrinkage," *The Journal of Physical Chemistry C,* vol. 124, no. 10, pp. 5861-5869, 2020/03/12 2020, doi: 10.1021/acs.jpcc.9b10675.
[108] N. S. Khabeev, "Diffusion effects in the oscillation of vapor–gas bubbles in a sound field," *International Journal of Heat and Mass Transfer,* vol. 50, no. 17, pp. 3556-3560, 2007/08/01/ 2007, doi: https://doi.org/10.1016/j.ijheatmasstransfer.2006.12.035.

[109] W. Guo, H.-H. Ngo, and J. Li, "A mini-review on membrane fouling," *Bioresource Technology,* vol. 122, pp. 27-34, 2012/10/01/ 2012, doi: https://doi.org/10.1016/j.biortech.2012.04.089.
[110] M. Y. Rezk and N. K. Allam, "Unveiling the Synergistic Effect of ZnO Nanoparticles and Surfactant Colloids for Enhanced Oil Recovery," *Colloid and Interface Science Communications,* vol. 29, pp. 33-39, 2019/03/01/ 2019, doi: https://doi.org/10.1016/j.colcom.2019.01.004.
[111] P. Singha, N.-K. Nguyen, J. Zhang, N.-T. Nguyen, and C. H. Ooi, "Oscillating sessile liquid marble - A tool to assess effective surface tension," *Colloids and Surfaces A: Physicochemical and Engineering Aspects,* vol. 627, p. 127176, 2021/10/20/ 2021, doi: https://doi.org/10.1016/j.colsurfa.2021.127176.
[112] B. T. Lobel *et al.*, "Formation of liquid marbles & aggregates: rolling and electrostatic formation using conductive hexagonal plates," *Materials Advances,* 10.1039/D0MA00670J vol. 1, no. 9, pp. 3302-3313, 2020, doi: 10.1039/D0MA00670J.
[113] N. S. Liao, S. Sidney, K. Deosaransingh, S. K. Van Den Eeden, J. Schwartz, and S. E. Alexeeff, "Particulate Air Pollution and Risk of Cardiovascular Events Among Adults With a History of Stroke or Acute Myocardial Infarction," *Journal of the American Heart Association,* vol. 10, no. 10, p. e019758, 2021/05/18 2021, doi: 10.1161/JAHA.120.019758.
[114] S. Peng, J. Sun, F. Liu, Z. Li, C. Wu, and H. Xiang, "The effect of short-term fine particulate matter exposure on glucose homeostasis: A panel study in healthy adults," *Atmospheric Environment,* vol. 268, p. 118769, 2022/01/01/ 2022, doi: https://doi.org/10.1016/j.atmosenv.2021.118769.
[115] M. Corbishley, *Illustrated Encyclopedia of Ancient Rome*. Getty Publications, 2004.
[116] M. Barati Dalenjan, E. Jamshidi, and H. Ale Ebrahim, "A screw-brush feeding system for uniform fine zinc oxide powder feeding and obtaining a homogeneous gas–particle flow," *Advanced Powder Technology,* vol. 26, no. 1, pp. 303-308, 2015/01/01/ 2015, doi: https://doi.org/10.1016/j.apt.2014.10.010.
[117] H. C. Hamaker, "The London—van der Waals attraction between spherical particles," *Physica,* vol. 4, no. 10, pp. 1058-1072, 1937/10/01/ 1937, doi: https://doi.org/10.1016/S0031-8914(37)80203-7.
[118] V. A. Kirsh, "The Effect of van der Waals' Forces on Aerosol Filtration with Fibrous Filters," *Colloid Journal,* vol. 62, no. 6, pp. 714-720, 2000/11/01 2000, doi: 10.1023/A:1026678725025.
[119] F. L. Leite, C. C. Bueno, A. L. Da Róz, E. C. Ziemath, and O. N. Oliveira, "Theoretical models for surface forces and adhesion and their measurement using atomic force microscopy," (in eng), *Int J Mol Sci,* vol. 13, no. 10, pp. 12773-856, Oct 8 2012, doi: 10.3390/ijms131012773.
[120] B. Rotenberg, A. J. Patel, and D. Chandler, "Molecular explanation for why talc surfaces can be both hydrophilic and hydrophobic," (in eng), *J Am Chem Soc,* vol. 133, no. 50, pp. 20521-7, Dec 21 2011, doi: 10.1021/ja208687a.
[121] F. Taherian, V. Marcon, N. F. A. van der Vegt, and F. Leroy, "What Is the Contact Angle of Water on Graphene?," *Langmuir,* vol. 29, no. 5, pp. 1457-1465, 2013/02/05 2013, doi: 10.1021/la304645w.
[122] T. W. Ng and Y. Panduputra, "Dynamical Force and Imaging Characterization of Superhydrophobic Surfaces," *Langmuir,* vol. 28, no. 1, pp. 453-458, 2012/01/10 2012, doi: 10.1021/la203732g.
[123] M. Katariya and T. Ng, "Drops transformed from a continuous flow on a superhydrophobic incline," *Journal of Physics D: Applied Physics,* vol. 46, p. 345302, 08/06 2013, doi: 10.1088/0022-3727/46/34/345302.
[124] M. Katariya, T. Vuong, and T. W. Ng, "Liquid Body Formation from a Semispherical Superhydrophobic Well on a Small Incline," *Langmuir,* vol. 30, no. 46, pp. 13731-13736, 2014/11/25 2014, doi: 10.1021/la502194d.
[125] S. Fujii, "Liquid Marble as an Amphibious Carrier for the Controlled Delivery and Release of Substances," *Langmuir,* vol. 38, no. 42, pp. 12757-12763, 2022/10/25 2022, doi: 10.1021/acs.langmuir.2c02305.

[126] J. Saczek *et al.*, "Long-Lived Liquid Marbles for Green Applications," *Advanced Functional Materials,* https://doi.org/10.1002/adfm.202011198 vol. 31, no. 35, p. 2011198, 2021/08/01 2021, doi: https://doi.org/10.1002/adfm.202011198.
[127] E. S. Lin, Z. Song, J. W. Ong, H. A. Abid, O. W. Liew, and T. W. Ng, "Liquid marble microbioreactor aeration facilitated by on-demand electrolysis," *Results in Chemistry,* vol. 4, p. 100334, 2022/01/01/ 2022, doi: https://doi.org/10.1016/j.rechem.2022.100334.
[128] A. Tyowua, F. Ahor, S. Yiase, and B. Binks, "Liquid marbles as microreactors for qualitative and quantitative inorganic analyses," *SN Applied Sciences,* vol. 2, 03/01 2020, doi: 10.1007/s42452-020-2174-9.
[129] M.-J. Dalbe, D. Cosic, M. Berhanu, and A. Kudrolli, "Aggregation of frictional particles due to capillary attraction," *Physical Review E,* vol. 83, no. 5, p. 051403, 05/23/ 2011, doi: 10.1103/PhysRevE.83.051403.
[130] X. Ma, N. N. Nguyen, and A. V. Nguyen, "A review on quantifying the influence of lateral capillary interactions on the particle floatability and stability of particle-laden interfaces," *Advances in Colloid and Interface Science,* vol. 307, p. 102731, 2022/09/01/ 2022, doi: https://doi.org/10.1016/j.cis.2022.102731.
[131] A. Gallo, F. Tavares, R. Das, and H. Mishra, "How particle–particle and liquid–particle interactions govern the fate of evaporating liquid marbles," *Soft Matter,* 10.1039/D1SM00750E vol. 17, no. 33, pp. 7628-7644, 2021, doi: 10.1039/D1SM00750E.
[132] S. Whitaker, "Flow in porous media I: A theoretical derivation of Darcy's law," *Transport in Porous Media,* vol. 1, no. 1, pp. 3-25, 1986/03/01 1986, doi: 10.1007/BF01036523.
[133] G. Rehman, I. Bukhari, M. Riaz, N. Rasool, U. Sattar, and H. Manzoor, "Determination of toxic heavy metals in different brands of talcum powder by atomic absorption spectrometry," *International Journal of Applied and Natural Sciences,* vol. 2, pp. 45-52, 01/01 2013.
[134] N. Gupta, H. P. Singh, and R. K. Sharma, "Metal nanoparticles with high catalytic activity in degradation of methyl orange: An electron relay effect," *Journal of Molecular Catalysis A: Chemical,* vol. 335, no. 1, pp. 248-252, 2011/02/01/ 2011, doi: https://doi.org/10.1016/j.molcata.2010.12.001.
[135] J. W. Ong, D. C. K. Chung, E. S. Lin, H. A. Abid, O. W. Liew, and T. W. Ng, "Syringe infusion pump with absolute piston displacement control," *Review of Scientific Instruments,* vol. 90, no. 7, p. 076108, 2019/07/01 2019, doi: 10.1063/1.5099271.
[136] A. Fernández-Pérez and G. Marbán, "Visible Light Spectroscopic Analysis of Methylene Blue in Water; What Comes after Dimer?," *ACS Omega,* vol. 5, no. 46, pp. 29801-29815, 2020/11/24 2020, doi: 10.1021/acsomega.0c03830.
[137] I. C. Nnorom, "Trace metals in cosmetic facial talcum powders marketed in Nigeria," *Toxicological & Environmental Chemistry,* vol. 93, no. 6, pp. 1135-1148, 2011/07/01 2011, doi: 10.1080/02772248.2011.577075.
[138] R. E. Gordon, S. Fitzgerald, and J. Millette, "Asbestos in commercial cosmetic talcum powder as a cause of mesothelioma in women," *International Journal of Occupational and Environmental Health,* vol. 20, no. 4, pp. 318-332, 2014/10/01 2014, doi: 10.1179/2049396714Y.0000000081.
[139] M. D. Doganci, B. U. Sesli, H. Y. Erbil, B. P. Binks, and I. E. Salama, "Liquid marbles stabilized by graphite particles from aqueous surfactant solutions," *Colloids and Surfaces A: Physicochemical and Engineering Aspects,* vol. 384, no. 1, pp. 417-426, 2011/07/05/ 2011, doi: https://doi.org/10.1016/j.colsurfa.2011.04.027.
[140] E. Bormashenko, R. Pogreb, A. Musin, R. Balter, G. Whyman, and D. Aurbach, "Interfacial and conductive properties of liquid marbles coated with carbon black," *Powder Technology,* vol. 203, no. 3, pp. 529-533, 2010/11/25/ 2010, doi: https://doi.org/10.1016/j.powtec.2010.06.019.
[141] V. V. Neklyudov, N. R. Khafizov, I. A. Sedov, and A. M. Dimiev, "New insights into the solubility of graphene oxide in water and alcohols," *Physical Chemistry Chemical Physics,* 10.1039/C7CP02303K vol. 19, no. 26, pp. 17000-17008, 2017, doi: 10.1039/C7CP02303K.
[142] P. Dash, T. Dash, T. K. Rout, A. K. Sahu, S. K. Biswal, and B. K. Mishra, "Preparation of graphene oxide by dry planetary ball milling process from natural graphite," *RSC Advances,* 10.1039/C5RA26491J vol. 6, no. 15, pp. 12657-12668, 2016, doi: 10.1039/C5RA26491J.

[143] L. Zhang, J. Xia, Q. Zhao, L. Liu, and Z. Zhang, "Functional graphene oxide as a nanocarrier for controlled loading and targeted delivery of mixed anticancer drugs," (in eng), *Small,* vol. 6, no. 4, pp. 537-44, Feb 22 2010, doi: 10.1002/smll.200901680.
[144] Z. Xiong *et al.*, "A Dynamic Graphene Oxide Network Enables Spray Printing of Colloidal Gels for High-Performance Micro-Supercapacitors," *Advanced Materials,* https://doi.org/10.1002/adma.201804434 vol. 31, no. 16, p. 1804434, 2019/04/01 2019, doi: https://doi.org/10.1002/adma.201804434.
[145] C. Greening, Z. F. Islam, and S. K. Bay, "Hydrogen is a major lifeline for aerobic bacteria," *Trends in Microbiology,* vol. 30, no. 4, pp. 330-337, 2022/04/01/ 2022, doi: https://doi.org/10.1016/j.tim.2021.08.004.
[146] M. Jafarzadeh and F. Farokhi, "Design and construction of an automatic syringe injection pump," *Pacific Science Review A: Natural Science and Engineering,* vol. 18, no. 2, pp. 132-137, 2016.
[147] S. Oliverio and V. Varlet, "Carbon monoxide analysis method in human blood by Airtight Gas Syringe – Gas Chromatography – Mass Spectrometry (AGS-GC-MS): Relevance for postmortem poisoning diagnosis," *Journal of Chromatography B,* vol. 1090, pp. 81-89, 2018/07/15/ 2018, doi: https://doi.org/10.1016/j.jchromb.2018.05.019.
[148] I. Leifer and D. Tang, "The acoustic signature of marine seep bubbles," *The Journal of the Acoustical Society of America,* vol. 121, no. 1, pp. EL35-EL40, 2007/01/01 2006, doi: 10.1121/1.2401227.
[149] M. Ochoa and B. Ziaie, "A fermentation-powered thermopneumatic pump for biomedical applications," *Lab on a Chip,* 10.1039/C2LC40620A vol. 12, no. 20, pp. 4044-4048, 2012, doi: 10.1039/C2LC40620A.
[150] A. M. Wilson, M. A. Peterlini, and L. Pedreira Mda, "Infusion pumps and red blood cell damage in transfusion therapy: an integrative revision of the academic literature," (in eng por
spa), *Rev Lat Am Enfermagem,* vol. 24, p. e2763, Aug 15 2016, doi: 10.1590/1518-8345.1155.2763.
[151] J. Hughes *et al.*, "Infusion pump-mediated mechanical hemolysis in pediatric patients," *Annals of Clinical & Laboratory Science,* vol. 45, no. 2, pp. 140-147, 2015.
[152] A. N. Rashed, C. Whittlesea, B. Forbes, and S. Tomlin, "The feasibility of using dose-banded syringes to improve the safety and availability of patient-controlled opioid analgesic infusions in children," *European journal of hospital pharmacy,* vol. 21, no. 5, pp. 306-308, 2014.
[153] C. Jeleazcov *et al.*, "Patient-controlled analgesia with target-controlled infusion of hydromorphone in postoperative pain therapy," *Anesthesiology,* vol. 124, no. 1, pp. 56-68, 2016.
[154] B. Jung *et al.*, "Efficacy evaluation of syringe pump developed for continuous drug infusion," *Journal of dental anesthesia and pain medicine,* vol. 16, no. 4, pp. 303-307, 2016.
[155] K. Müller, J. Holzapfel, and L. Brunnberg, "Total intravenous anaesthesia by boluses or by continuous rate infusion of propofol in mute swans (Cygnus olor)," *Veterinary anaesthesia and analgesia,* vol. 38, no. 4, pp. 286-291, 2011.
[156] M. S. Cubberley and W. A. Hess, "An inexpensive programmable dual-syringe pump for the chemistry laboratory," *Journal of Chemical Education,* vol. 94, no. 1, pp. 72-74, 2017.
[157] B. Wijnen, E. J. Hunt, G. C. Anzalone, and J. M. Pearce, "Open-source syringe pump library," *PloS one,* vol. 9, no. 9, p. e107216, 2014.
[158] D. Guelig *et al.*, "Design of a novel, adjustable flow rate, reusable, electricity-free, low-cost syringe infusion pump," *Journal of Medical Devices,* vol. 11, no. 4, 2017.
[159] R. Voelker, "Avoiding Open-Heart Surgery," *JAMA,* vol. 316, no. 13, pp. 1350-1350, 2016.
[160] J. R. Lake, K. C. Heyde, and W. C. Ruder, "Low-cost feedback-controlled syringe pressure pumps for microfluidics applications," *PLoS One,* vol. 12, no. 4, p. e0175089, 2017.
[161] D. H. P. Kang, M. Chen, and O. A. Ogunseitan, "Potential environmental and human health impacts of rechargeable lithium batteries in electronic waste," *Environmental science & technology,* vol. 47, no. 10, pp. 5495-5503, 2013.
[162] J. Zhang, C. Chen, X. Zhang, and S. Liu, "Study on the environmental risk assessment of lead-acid batteries," *Procedia Environmental Sciences,* vol. 31, pp. 873-879, 2016.

[163] Y. Kawabata, "Effect of coefficient of viscosity and ambient temperature on the flow rate of drug solutions in infusion pumps," *Pharmaceutical Development and Technology,* vol. 17, no. 6, pp. 755-762, 2012.
[164] K. Hutchison, "Assessment of gelling in insulin solutions for infusion pumps," *Journal of pharmacy and pharmacology,* vol. 37, no. 8, pp. 528-531, 1985.
[165] A. Furtado, J. Moutinho, S. Moura, F. Oliveira, and E. Filipe, "The role of adequate reference materials in density measurements in hemodialysis," in *Journal of Physics: Conference Series*, 2015, vol. 588, no. 1: IOP Publishing, p. 012051.
[166] K. Takamura, H. Fischer, and N. R. Morrow, "Physical properties of aqueous glycerol solutions," *Journal of Petroleum Science and Engineering,* vol. 98, pp. 50-60, 2012.
[167] J. L. Dashnau, N. V. Nucci, K. A. Sharp, and J. M. Vanderkooi, "Hydrogen bonding and the cryoprotective properties of glycerol/water mixtures," *The Journal of Physical Chemistry B,* vol. 110, no. 27, pp. 13670-13677, 2006.
[168] A. A. A. Zahidi, B. H.-P. Cheong, S. H. Huynh, T. Vuong, O. W. Liew, and T. W. Ng, "Glycerol–water sessile drop elongation on PTFE inclines in relation to biochemical applications," *Colloids and Surfaces A: Physicochemical and Engineering Aspects,* vol. 486, pp. 21-28, 2015.
[169] H. F. Stils Jr, "Adjuvants and antibody production: dispelling the myths associated with Freund's complete and other adjuvants," *ILAR journal,* vol. 46, no. 3, pp. 280-293, 2005.
[170] D. C. K. Chung, M. Katariya, A. A. A. Zahidi, C. Y. Lau, O. W. Liew, and T. W. Ng, "Antibody drop based handling with near-superhydrophobic mesh substrates overcomes condensation sticking," *Materials Science and Engineering: C,* vol. 96, pp. 599-605, 2019.
[171] D. Nychka, G. Gray, P. Haaland, D. Martin, and M. O'connell, "A nonparametric regression approach to syringe grading for quality improvement," *Journal of the American Statistical Association,* vol. 90, no. 432, pp. 1171-1178, 1995.
[172] Y. Priyangani, G. Dharmaratne, and S. Sridharan, "Factors associated and response to needle stick injuries among nursing officers in district general hospitals of Sri Lanka," *Global Journal of Health Science,* vol. 9, no. 8, p. 107, 2017.
[173] A. Winkel, O. Pedersen, E. Ella, A. M. Ismail, and T. D. Colmer, "Gas film retention and underwater photosynthesis during field submergence of four contrasting rice genotypes," *Journal of Experimental Botany,* vol. 65, no. 12, pp. 3225-3233, 2014, doi: 10.1093/jxb/eru166.
[174] T. C. Weber, "Acoustic observations and characterization of oceanic methane gas bubbles rising from the seabed," *The Journal of the Acoustical Society of America,* vol. 140, no. 4, pp. 3077-3077, 2016/10/01 2016, doi: 10.1121/1.4969587.
[175] V. Capozzi, M. Fragasso, R. Romaniello, C. Berbegal, P. Russo, and G. Spano, "Spontaneous Food Fermentations and Potential Risks for Human Health," *Fermentation*, vol. 3, no. 4, doi: 10.3390/fermentation3040049.
[176] F. Liew, M. E. Martin, R. C. Tappel, B. D. Heijstra, C. Mihalcea, and M. Köpke, "Gas fermentation—a flexible platform for commercial scale production of low-carbon-fuels and chemicals from waste and renewable feedstocks," *Frontiers in microbiology,* vol. 7, p. 694, 2016.
[177] K. Liu *et al.*, "Hydrogen production from hydrolysis of Al–Ga–In–SnCl2 composites," *Materials Research Express,* vol. 6, no. 8, p. 085515, 2019/05/17 2019, doi: 10.1088/2053-1591/ab1e5d.
[178] C. Chen *et al.*, "Preparation of Al–Bi–NaCl composites and evaluation of their hydrogen production performance," *Materials Research Express,* vol. 6, no. 4, p. 046532, 2019/01/18 2019, doi: 10.1088/2053-1591/aafc54.
[179] L. C. Emenyeonu, A. E. Croxford, and M. J. Wilkinson, "The potential of aerosol eDNA sampling for the characterisation of commercial seed lots," *PLOS ONE,* vol. 13, no. 8, p. e0201617, 2018, doi: 10.1371/journal.pone.0201617.
[180] J. Priestley, *Experiments and observations on different kinds of air*. J. Johnson, 1776.
[181] F. Thompson and M. Elamari, "An automated gasometer for the teaching laboratory," *Physics Education,* vol. 43, no. 6, p. 588, 2008/11/01 2008, doi: 10.1088/0031-9120/43/6/004.

[182] C. A. Greene and P. S. Wilson, "Laboratory investigation of a passive acoustic method for measurement of underwater gas seep ebullition," *The Journal of the Acoustical Society of America,* vol. 131, no. 1, pp. EL61-EL66, 2012/01/01 2011, doi: 10.1121/1.3670590.
[183] S. H. Huynh, A. A. A. Zahidi, M. Muradoglu, B. H.-P. Cheong, and T. W. Ng, "Plastron-Mediated Growth of Captive Bubbles on Superhydrophobic Surfaces," *Langmuir,* vol. 31, no. 24, pp. 6695-6703, 2015/06/23 2015, doi: 10.1021/acs.langmuir.5b00058.
[184] S. H. Huynh, C. Y. Lau, B. H.-P. Cheong, M. Muradoglu, O. W. Liew, and T. W. Ng, "Controlled transport of captive bubbles on plastrons," *Soft Matter,* 10.1039/C5SM01910A vol. 11, no. 38, pp. 7474-7477, 2015, doi: 10.1039/C5SM01910A.
[185] H. A. Abid, J. W. Ong, E. S. Lin, O. W. Liew, and T. W. Ng, "Volume and rate measurement of slowly generated gas bubbles," *Flow Measurement and Instrumentation,* vol. 72, p. 101694, 2020/04/01/ 2020, doi: https://doi.org/10.1016/j.flowmeasinst.2020.101694.
[186] N. Otsu, "A Threshold Selection Method from Gray-Level Histograms," *IEEE Transactions on Systems, Man, and Cybernetics,* vol. 9, no. 1, pp. 62-66, 1979, doi: 10.1109/TSMC.1979.4310076.
[187] E. S. Gaddis and A. Vogelpohl, "Bubble formation in quiescent liquids under constant flow conditions," *Chemical Engineering Science,* vol. 41, no. 1, pp. 97-105, 1986/01/01/ 1986, doi: https://doi.org/10.1016/0009-2509(86)85202-2.
[188] M. Lichti and H.-J. Bart, "Bubble size distributions with a shadowgraphic optical probe," *Flow Measurement and Instrumentation,* vol. 60, pp. 164-170, 2018/04/01/ 2018, doi: https://doi.org/10.1016/j.flowmeasinst.2018.02.020.
[189] J. Jamaludin, R. A. Rahim, H. A. Rahim, M. H. Fazalul Rahiman, S. Z. Mohd Muji, and J. M. Rohani, "Charge coupled device based on optical tomography system in detecting air bubbles in crystal clear water," *Flow Measurement and Instrumentation,* vol. 50, pp. 13-25, 2016/08/01/ 2016, doi: https://doi.org/10.1016/j.flowmeasinst.2016.06.001.
[190] T. Xue, L. Qu, Z. Cao, and T. Zhang, "Three-dimensional feature parameters measurement of bubbles in gas–liquid two-phase flow based on virtual stereo vision," *Flow Measurement and Instrumentation,* vol. 27, pp. 29-36, 2012/10/01/ 2012, doi: https://doi.org/10.1016/j.flowmeasinst.2012.07.007.
[191] P. Saffman, "On the rise of small air bubbles in water," *Journal of Fluid Mechanics,* vol. 1, no. 3, pp. 249-275, 1956.
[192] H. S. Gan *et al.*, "Augmented reality experimentation on oxygen gas generation from hydrogen peroxide and bleach reaction," *Biochemistry and Molecular Biology Education,* https://doi.org/10.1002/bmb.21117 vol. 46, no. 3, pp. 245-252, 2018/05/01 2018, doi: https://doi.org/10.1002/bmb.21117.
[193] H. A. Abid *et al.*, "Polymerase chain reaction thermal cycling using the programmed tilt displacements of capillary tubes," *Review of Scientific Instruments,* vol. 91, no. 10, p. 104105, 2020/10/01 2020, doi: 10.1063/5.0007879.
[194] E. S. Lin *et al.*, "Liquid marble clearance and restoration via gas bubble insertion and bursting," *Soft Matter,* 10.1039/D0SM02117B vol. 17, no. 9, pp. 2512-2517, 2021, doi: 10.1039/D0SM02117B.
[195] J. Boulton-Stone and J. Blake, "Gas bubbles bursting at a free surface," *Journal of Fluid Mechanics,* vol. 254, pp. 437-466, 1993.
[196] E. Sheppard and N. Tcheurekdjian, "Monolayer Studies IV. Surface Films of Emulsion Latex Particles," *Journal of Colloid and Interface Science - J COLLOID INTERFACE SCI,* vol. 28, pp. 481-486, 11/01 1968, doi: 10.1016/0021-9797(68)90080-5.
[197] A. M. Munshi, V. N. Singh, M. Kumar, and J. P. Singh, "Effect of nanoparticle size on sessile droplet contact angle," *Journal of Applied Physics,* vol. 103, no. 8, p. 084315, 2008/04/15 2008, doi: 10.1063/1.2912464.
[198] C. P. Whitby, X. Bian, and R. Sedev, "Spontaneous liquid marble formation on packed porous beds," *Soft Matter,* 10.1039/C2SM26529J vol. 8, no. 44, pp. 11336-11342, 2012, doi: 10.1039/C2SM26529J.
[199] R. de Levie, "The electrolysis of water," *Journal of Electroanalytical Chemistry,* vol. 476, no. 1, pp. 92-93, 1999/10/21/ 1999, doi: https://doi.org/10.1016/S0022-0728(99)00365-4.
[200] Q. Zhou *et al.*, "Electrode-dependent ammonium oxidation with different low C/N ratios in single-chambered microbial electrolysis cells," *Bioelectrochemistry,* vol. 142, p. 107889, 2021/12/01/ 2021, doi: https://doi.org/10.1016/j.bioelechem.2021.107889.

[201] S. Liang *et al.*, "Improved decolorization of dye wastewater in an electrochemical system powered by microbial fuel cells and intensified by micro-electrolysis," *Bioelectrochemistry,* vol. 124, pp. 112-118, 2018/12/01/ 2018, doi: https://doi.org/10.1016/j.bioelechem.2018.07.008.
[202] T. L. Place, F. E. Domann, and A. J. Case, "Limitations of oxygen delivery to cells in culture: An underappreciated problem in basic and translational research," *Free Radical Biology and Medicine,* vol. 113, pp. 311-322, 2017/12/01/ 2017, doi: https://doi.org/10.1016/j.freeradbiomed.2017.10.003.
[203] C. A. C. Sequeira, D. M. F. Santos, B. Šljukić, and L. Amaral, "Physics of Electrolytic Gas Evolution," *Brazilian Journal of Physics,* vol. 43, no. 3, pp. 199-208, 2013/06/01 2013, doi: 10.1007/s13538-013-0131-4.
[204] J. Miguet, F. Rouyer, and E. Rio, "The Life of a Surface Bubble," *Molecules*, vol. 26, no. 5, doi: 10.3390/molecules26051317.
[205] O. Atasi, D. Legendre, B. Haut, R. Zenit, and B. Scheid, "Lifetime of Surface Bubbles in Surfactant Solutions," *Langmuir,* vol. 36, no. 27, pp. 7749-7764, 2020/07/14 2020, doi: 10.1021/acs.langmuir.9b03597.
[206] P. D. Howell, "The Draining of a two-dimensional bubble," *Journal of Engineering Mathematics,* vol. 35, no. 3, pp. 251-272, 1999/04/01 1999, doi: 10.1023/A:1004399105606.
[207] M. K. Tripathi, K. C. Sahu, and R. Govindarajan, "Dynamics of an initially spherical bubble rising in quiescent liquid," *Nature Communications,* vol. 6, no. 1, p. 6268, 2015/02/17 2015, doi: 10.1038/ncomms7268.
[208] J. Navisa, T. Sravya, M. Swetha, and M. Venkatesan, "Effect of Bubble Size on Aeration Process," *Asian Journal of Scientific Research,* vol. 7, pp. 482-487, 04/01 2014, doi: 10.3923/ajsr.2014.482.487.
[209] R. Wang and X. Li, "On the effective surface tension of powder-derived liquid marbles," *Powder Technology,* vol. 367, pp. 608-615, 2020/05/01/ 2020, doi: https://doi.org/10.1016/j.powtec.2020.04.028.
[210] J. Yang, A. Wang, and Q. Zheng, "Ultra-long lifetime water bubbles stabilized by negative pressure generated between microparticles," *Soft Matter,* 10.1039/C7SM01684K vol. 13, no. 44, pp. 8202-8208, 2017, doi: 10.1039/C7SM01684K.
[211] P. Roy, "Highly efficient vaccines for Bluetongue virus and a related Orbivirus based on reverse genetics," *Current Opinion in Virology,* vol. 44, pp. 35-41, 2020/10/01/ 2020, doi: https://doi.org/10.1016/j.coviro.2020.05.003.
[212] O. Lorain, P. Thiebaud, E. Badorc, and Y. Aurelle, "Potential of freezing in wastewater treatment: soluble pollutant applications," *Water research,* vol. 35, no. 2, pp. 541-547, 2001.
[213] H. Kiani, Z. Zhang, A. Delgado, and D.-W. Sun, "Ultrasound assisted nucleation of some liquid and solid model foods during freezing," *Food Research International,* vol. 44, no. 9, pp. 2915-2921, 2011.
[214] J. W. Ong, T. Minifie, E. S. Lin, H. A. Abid, O. W. Liew, and T. W. Ng, "Cryopreservation without dry ice-induced acidification during sample transport," *Analytical Biochemistry,* vol. 608, p. 113906, 2020/11/01/ 2020, doi: https://doi.org/10.1016/j.ab.2020.113906.
[215] D. C. K. Chung *et al.*, "A superhydrophobic manhole for drops," *Journal of Materials Chemistry A,* vol. 5, no. 3, pp. 914-918, 2017.
[216] J. W. Ong, Z. Song, H. A. Abid, E. S. Lin, O. W. Liew, and T. W. Ng, "Cryoprotectant-free preservation of bacteria using semi-spherical drops," *Cryobiology,* vol. 104, pp. 98-101, 2022/02/01/ 2022, doi: https://doi.org/10.1016/j.cryobiol.2021.11.179.
[217] S. R. Foley *et al.*, "A comprehensive study of ovine haemostasis to assess suitability to model human coagulation," *Thrombosis Research,* vol. 134, no. 2, pp. 468-473, 2014/08/01/ 2014, doi: https://doi.org/10.1016/j.thromres.2014.05.026.
[218] J. W. Ong *et al.*, "Unmanned aerial vehicle transport of frozen blood samples using phase change materials," *Biosystems Engineering,* vol. 221, pp. 30-42, 2022/09/01/ 2022, doi: https://doi.org/10.1016/j.biosystemseng.2022.06.008.
[219] S. R. Narasimharaju *et al.*, "A comprehensive review on laser powder bed fusion of steels: Processing, microstructure, defects and control methods, mechanical properties, current

challenges and future trends," *Journal of Manufacturing Processes,* vol. 75, pp. 375-414, 2022/03/01/ 2022, doi: https://doi.org/10.1016/j.jmapro.2021.12.033.
[220] J. Walker, J. R. Middendorf, C. C. C. Lesko, and J. Gockel, "Multi-material laser powder bed fusion additive manufacturing in 3-dimensions," *Manufacturing Letters,* vol. 31, pp. 74-77, 2022/01/01/ 2022, doi: https://doi.org/10.1016/j.mfglet.2021.07.011.
[221] M. Campagnoli, M. Galati, and A. Saboori, "On the processability of copper components via powder-based additive manufacturing processes: Potentials, challenges and feasible solutions," *Journal of Manufacturing Processes,* vol. 72, pp. 320-337, 12/01 2021, doi: 10.1016/j.jmapro.2021.10.038.
[222] L. Constantin, Z. Wu, N. Li, L. Fan, J.-F. Silvain, and Y. F. Lu, "Laser 3D printing of complex copper structures," *Additive Manufacturing,* vol. 35, p. 101268, 2020/10/01/ 2020, doi: https://doi.org/10.1016/j.addma.2020.101268.
[223] O. R. Enríquez, Á. G. Marín, K. G. Winkels, and J. H. Snoeijer, "Freezing singularities in water drops," *Physics of Fluids,* vol. 24, no. 9, p. 091102, 2012/09/01 2012, doi: 10.1063/1.4747185.
[224] A. Hashmi, A. Strauss, and J. Xu, "Freezing of a Liquid Marble," *Langmuir,* vol. 28, no. 28, pp. 10324-10328, 2012/07/17 2012, doi: 10.1021/la301854f.
[225] D. Zang *et al.*, "Tunable shape transformation of freezing liquid water marbles," *Soft Matter,* 10.1039/C3SM51885J vol. 10, no. 9, pp. 1309-1314, 2014, doi: 10.1039/C3SM51885J.
[226] S. H. Hopper and H. S. Adams, "Copper poisoning from vending machines," (in eng), *Public Health Rep (1896),* vol. 73, no. 10, pp. 910-4, Oct 1958.
[227] A. Semple, W. Parry, and D. Phillips, "Acute copper poisoning. An outbreak traced to contaminated water from a corroded geyser," *Lancet,* pp. 700-701, 1960.
[228] K. R. Sreejith, C. H. Ooi, J. Jin, D. V. Dao, and N.-T. Nguyen, "An automated on-demand liquid marble generator based on electrohydrodynamic pulling," *Review of Scientific Instruments,* vol. 90, no. 5, p. 055102, 2019/05/01 2019, doi: 10.1063/1.5094522.
[229] A. Nikolov and D. Wasan, "Air bubble bursting phenomenon at the air-water interface monitored by the piezoelectric-acoustic method," (in eng), *Adv Colloid Interface Sci,* vol. 272, p. 101998, Oct 2019, doi: 10.1016/j.cis.2019.101998.
[230] O. Couvert, M.-L. Divanac'h, A. Lochardet, D. Thuault, and V. Huchet, "Modelling the effect of oxygen concentration on bacterial growth rates," *Food Microbiology,* vol. 77, pp. 21-25, 2019/02/01/ 2019, doi: https://doi.org/10.1016/j.fm.2018.08.005.
[231] A. Marin, O. Enriquez, P. Brunet, P. Colinet, and J. Snoeijer, "Universality of Tip Singularity Formation in Freezing Water Drops," *Physical review letters,* vol. 113, 04/25 2014, doi: 10.1103/PhysRevLett.113.054301.
[232] A. Schetnikov, V. Matiunin, and V. Chernov, "Conical shape of frozen water droplets," *American Journal of Physics,* vol. 83, no. 1, pp. 36-38, 2015/01/01 2014, doi: 10.1119/1.4897499.
[233] A. Starostin, V. Strelnikov, L. A. Dombrovsky, S. Shoval, and E. Bormashenko, "On the universality of shapes of the freezing water droplets," *Colloid and Interface Science Communications,* vol. 47, p. 100590, 2022/03/01/ 2022, doi: https://doi.org/10.1016/j.colcom.2022.100590.